New Microfabricated Tools for Electrochemical Imaging and Sensing

Todd J. Anderson

A dissertation

submitted in partial fulfillment of the

requirements for the degree of

Doctor of Philosophy

University of Washington

2021

Reading Committee:

Bo Zhang, Chair

Ashleigh Theberge

Bruce Robinson

Program Authorized to Offer Degree:

Chemistry

University of Washington

Abstract

New Microfabricated Tools for Electrochemical Imaging and Sensing

Todd J. Anderson

Chair of the Supervisory Committee:
Professor Bo Zhang
Chemistry

This dissertation covers the development of microfabricated bipolar ultramicroelectrode arrays consisting of many thousands of individually addressable electrodes to enable high resolution electrochemical imaging. Two different devices are presented and discussed prior to characterization in several proof-of-concept experiments, after which one of the array designs is utilized in the creation of a high-throughput electrocatalyst screening platform. Additionally, a micromachining procedure for the fabrication of glass-supported solid-state nanopore substrates is introduced.

Chapter 1 opens with an introduction to various electrochemical imaging techniques and examines bipolar coupling to an optical reporter reaction as a method for simultaneously reading the current through very dense electrode arrays. The advantages of such a scheme are further

explored from the perspective of efficient electrocatalytic screening before the chapter concludes with a discussion of possible solutions to the issues associated with high frequency biomolecule detection via resistive pulse sensing in solid-state nanopores. Chapter 2 then presents a submicron bipolar microelectrode array design which utilizes interfering laser beams to generate the requisite periodic electrode patterns. The shortcomings of this design are addressed in Chapter 3 with the fabrication of an updated device which is used to image several dynamic electrochemical systems via an alternate imaging scheme. This updated device is further utilized in Chapter 4 as a platform for highly parallelized screening of compositionally varied electrocatalyst samples. Chapter 5 then closes this dissertation with the introduction of a novel microfabrication method for freestanding SiN_x membranes on glass chips as a means of eliminating the capacitive noise effects associated with semiconductor/insulator interfaces in high bandwidth solid-state nanopore measurements.

TABLE OF CONTENTS

LIST OF SCHEMES

LIST OF FIGURES

ACKNOWLEDGEMENTS

I would like to begin by thanking my advisor, Dr. Bo Zhang, for the direction he has provided throughout my graduate studies. His mentorship has been critical to my personal and academic growth, and I greatly appreciate the ready availability of his guidance over these past years. I would also like to express my appreciation to my other committee members for their generous support, specifically Dr. Ashleigh Theberge for providing me with invaluable soft lithography resources and advice, Dr. Bruce Robinson for teaching me everything I know about LabVIEW, and Dr. Lih Lin for graciously serving as the graduate school representative for both my general and final exams. Additionally, I must convey my gratitude to Dr. Robert Synovec for providing the opportunity to gain my first research experience as an undergraduate and giving me much-needed feedback during my graduate application process and also to the Chemistry Department and Pacific Northwest National Laboratory for financial assistance in the form of the Lloyd and Florence West Fellowship and the PNNL Fellowship, respectively.

Several members of the Zhang lab have greatly influenced my graduate experience for the better, particularly Peter Defnet with whom I have had the genuine pleasure of collaborating on multiple projects, Dr. Chris Gunderson who took the time to share his nanofabrication knowledge when I first joined the group and helped shape my outlook on graduate life, and Dr. Hongfang Gao who was an endless source of optimism and laughs during the year in which we shared an office. Outside of the program, I want to thank Sung and my other shooting buddies for giving me something fun to look forward to on the weekends. I also need to recognize the impact that Dr. Amrita Basu has had on this phase of my life. We had a lot of fun.

Most importantly, however, I want to express my deepest gratitude to my parents for their unwavering love, continual sacrifice, and endless support that has brought me to where I am today. The pride that the two of you have expressed in me means more to me than anything else.

DEDICATION

To Mom and Dad

You are always the first people I want to tell when things are going well

and the first people I want to talk to when they aren't.

Chapter 1
INTRODUCTION

1.1 Electrochemical Imaging Principles

Electroanalytical measurements are most often carried out by immersion of two or three electrodes in a solution to form an electrochemical cell. The working electrode surface is biased by an external power source with an electrochemical potential relative to the surrounding solution to induce the flow of charge (*i.e.*, electrical current) across the electrode/solution interface via oxidation or reduction of a dissolved redox species. The potential of the working electrode is measured relative to a known redox half reaction occurring at the surface of a reference electrode. A counter electrode may also be utilized for cells involving macroscale working electrodes to provide a path for the majority of the electrical current to pass through the cell without disrupting the stability of the reference electrode by passing current through it. The current response to the applied potential at the working electrode surface can provide rich information about both the chemical properties and concentration of dissolved analytes but is limited to probing the electrode's immediate surroundings. Consequently, measurements must be taken at multiple locations to image the redox activity of spatially heterogeneous electrochemical systems.

Scanning probe techniques provide the most straightforward means of achieving spatial resolved electrochemistry, with scanning electrochemical microscopy (SECM) being the first and most prolific.[1] In this electrochemical imaging method, a miniscule electrode scanned at a constant height over a substrate of interest which has been immersed in an electrolyte solution while the potentials of the electrode and substrate are separately controlled by a bipotentiostat. The resulting current response of the electrode is then correlated with its lateral position above the substrate to

map the latter's redox behavior. Parallel techniques have also employed a variety of other probes to enable electrochemical imaging. In scanning ion conductance microscopy (SICM), a micropipette housing an electrode is scanned across a substrate surface and its z-height controlled to maintain constant ionic current through the pipette orifice, thereby enabling mapping of the substrate topography and conductance.[2] Scanning electrochemical cell microscopy (SECCM) makes similar use of a micropipette filled with electrolyte solution as the probe but is not carried out over an immersed substrate[3]; instead, a droplet of solution at the pipette tip is stepped across the conductive substrate surface to repeatedly form a tiny electrochemical cell in which the portion of the substrate wetted by the solution functions as the working electrode. However, the prohibitively long time required to compile a sufficient number of scans to resolve a region of interest limits the applications of these methods to the study of steady-state systems. Optical detection of redox products provides an alternate scheme which does not suffer from the same temporal limitations[4–6] but is ultimately hindered by the finite number of reactions which generate an optical signal loss of resolution due to free diffusion of the detected species; the use of a pH-dependent fluorescent tracer species to monitor reactions which alter solution pH is similarly constrained.[7–9]

Arrayed measurements provide a more flexible approach to electrochemical imaging in which the current responses of an arrangement of multiple individually addressable electrodes are recorded in tandem.[10–14] This introduction of parallelization enables the study of dynamic systems since each electrode provides a continuous stream of information from a single location, but the fabrication of very large and dense arrays necessary for high resolution imaging is extremely challenging due to the number of leads required to make electrical contact with all of the constituent electrodes. Additionally, the maximum addressable size of such arrays is restricted by

the number of data channels supported by the data acquisition system; consequently, many studies have only been able to make use of smaller subsets of large arrays[10,11] or are limited to sequentially sampling of groups of electrodes.[12–14] An alternative method of monitoring the current response of many electrodes in parallel is therefore of great importance to further expanding the resolution and capacity of electrochemical imaging with electrode arrays.

1.2 Bipolar Electrode Arrays

Bipolar electrodes (BPEs) comprise a unique type of electrochemical system that differs from the conventional setup described in the previous section in that the potential difference between the electrode and solution is determined by the electric field in solution rather than by direct control from an external power source.[15] In an open bipolar system, a floating potential conductor is placed in solution between two driving electrodes which are biased relative to one another, thereby resulting in polarization of the conductor and a difference in potential between any two points on its surface equal to the potential drop of the electric field across this same distance. If such a potential difference exceeds the difference in formal potentials of two redox molecules in solution, the corresponding oxidation and reduction half reactions of these species will occur on opposite ends of the BPE. To maintain a state of electroneutrality, the relative rates of these reactions will be linked to one another such that electrons generated by the oxidation reaction on the anodic pole will flow directly through the electrode to drive the reduction reaction on the cathodic pole. Thus, the current from a redox reaction of interest can be monitored in a completely wireless fashion via coupling to a separate reporter reaction without the necessity for direct electrical contact. The Crooks group has made extensive use of such a scheme in which oxidation and subsequent dissolution of a series of metal bands patterned on the surface of an open BPE serves as a visual indicator of the rate of a coupled reduction reaction.[16–19] However, due to the parallel ionic current

pathway which exists in an open bipolar system, relatively large electrodes are necessary to yield a sufficient potential difference between their poles to achieve reaction coupling without the application of extremely high voltages. This requirement greatly limits the maximum achievable density of open BPE arrays.

Closed bipolar systems operate on a similar principle to their open bipolar counterparts, but the aforementioned parallel ionic current pathway is not present.[20,21] Instead, a driving potential is applied across a floating potential conductor embedded in an insulating substrate and exposed at either end to two segregated solutions. Because there is no path for current to travel through the system except through the BPE, the majority of the voltage drop between the driving electrodes is observed at the BPE/solution interface rather than occurring linearly along the electrode's length, thereby rendering the size of the electrode irrelevant when determining the potential difference between its two ends. Consequently, closed BPEs are well-suited to the creation of dense arrays of micro- and nanoscale electrodes which are necessary for high resolution electrochemical imaging.

1.3 Optical Imaging via Bipolar Coupling

Fluorescence-enabled electrochemical microscopy (FEEM) is an electrochemical imaging technique introduced by our group in 2013 which utilizes arrays of closed BPEs to couple a redox reaction of interest to a fluorogenic reporter reaction.[22] This reporter reaction has typically been the reduction of resazurin to fluorescent resorufin, although the oxidation of dihydroresorufin to resorufin has also been used to monitor reduction processes.[23] In both of these detection methods, each analyte molecule which is oxidized or reduced on the detecting pole of a BPE results in the production of a stoichiometric number of fluorogenic species on the reporting pole which each emit a continual stream of photons in response to incident excitation light. As a result of this

amplification effect, the current through each electrode is proportional to the derivative of the fluorescence intensity so long as the limiting reaction occurs on the detecting side of the array.

FEEM has already been utilized in conjunction with BPE arrays fabricated from bundles of carbon fibers insulated in epoxy to resolve a number of dynamic electrochemical phenomena including heterogeneity of electrocatalytic activity,[22] the convective flow of a redox molecule solution from a micropipette,[22] and the diffusion layers about an ultramicroelectrode (UME).[24] However, the spatial resolution achieved with these arrays was negatively impacted by the poor uniformity and crosstalk due to aggregation of the constituent carbon fibers. To address these shortcomings, the construction of microfabricated arrays with geometrically arranged microscale electrodes was explored. The development and characterization of two different massive closed bipolar UME array platforms utilizing micromachining methods is discussed in Chapters 2 and 3.

Although the generation of a fluorescent moiety provides an effective means of monitoring electrochemical processes with an optical signal via bipolar coupling, free diffusion of reporter molecules away from their electrodes of origin results in a loss of spatial resolution and accumulation of fluorescent background (which is discussed in greater detail in Chapter 2). Electrochemiluminescence (ECL), which has already been extensively utilized in biosensing applications,[25] has therefore been investigated as an alternative reporter reaction for optical imaging with BPE arrays to maximize the spatial resolution of this scheme. In the anodic ECL mechanism which was selected, simultaneous oxidation of $Ru(bpy)_3^{2+}$ and a 2-(dibutylamino)ethanol (DBAE) coreactant at the electrode surface is followed by deprotonation of the resulting DBAE radical cation to form a strongly reducing radical species which interacts with the oxidized Ru complex to yield an electronically excited $Ru(bpy)_3^{2+*}$ which then relaxes to the ground state via emission of a photon. Because this light results from the rapid interaction of

multiple reaction intermediates produced at the electrode surface rather than subsequent excitation of an untethered fluorophore, this optical signal is confined to the electrode surface and is free of any luminescent background. Additionally, the consistent ratio between the number of electrons generated via initial oxidation of the ECL precursors and the number of emitted photons results in a directly proportional relationship between the current through the electrode and the optical signal emanating from its surface. Indeed, ECL systems have already been utilized in conjunction with both open[26] and closed bipolar electrode arrays[27–30] as reporter reactions, but the applications of these devices have been limited to either sensing or very low resolution imaging (~0.5 mm). Electrochemical imaging utilizing an ECL reporter reaction with massive bipolar UME arrays is therefore discussed in Chapter 3 and carried out in several proof-of-concept experiments.

1.4 High-Throughput Electrocatalytic Screening

Heterogeneous electrocatalysts are electrode materials which lower the energy barrier for a reaction of interest by altering the interaction of the reactant species with the electrode surface; this lower energy barrier is usually manifested as a reduction in the magnitude of the potential which must be applied to the electrode to drive the reaction. The development of new electrocatalysts is of particular importance to the generation of hydrogen via electrochemical water splitting (the hydrogen evolution reaction, HER) for clean energy applications.[31,32] High-throughput screening of electrocatalyst candidates is typically carried out via a combinatorial approach[33–35] in which large libraries of compositionally varied samples are synthesized and subsequently screened for catalytic activity toward a specific reaction by measuring the current onset potential or current density at a specific applied voltage. Since the efficiency of a particular method is governed by both the library synthesis time and the parallelization of the scanning

method, new techniques for streamlining both of these steps are of interest in informing the discovery and optimization of new electrocatalysts.

The most commonly used library synthesis method is distribution aliquots of conductive inks loaded with known electrocatalyst compositions[36,37] or solutions containing known concentrations of multiple metal salts which are subsequently reduced to yield alloys.[38–40] However, these techniques are fairly time consuming due to their sequential nature. The generation of continuous gradients in electrocatalyst composition via physical vapor deposition (PVD)[41–45] provides a more attractive method for the rapid generation of a large electrocatalyst libraries in a single experiment, but the required instrumentation is prohibitively expensive. All of the electrochemical imaging techniques outlined in Section 1.1 have been adapted into high-throughput electrocatalyst screening platforms (*i.e.*, scanning probe techniques,[46] optical detection of redox products,[38,42,47–50] individually addressable electrode arrays[36,37,43,47,51–54]) but nevertheless suffer from the same issues regarding data collection time, poor resolution/crosstalk, and a limited number of data channels, respectively. Screening of electrocatalyst samples deposited on both open[17–19,44,55] and closed[56,57] bipolar electrode arrays has been successfully carried out, but none of these studies have made use of arrays comprised of more than a handful of electrodes and only two have utilized an optical reporter reaction. A high-throughput electrocatalyst screening platform utilizing an ECL-based readout of the HER activity of electrocatalyst candidates deposited on massive bipolar UME arrays via a novel gradient electrodeposition method is therefore described in Chapter 4.

1.5 Glass Solid-State Nanopore Substrates

Because of the electrical circuit which connects the electrodes of an electrochemical cell, each electron which is removed when a dissolved species is oxidized on the anode is replaced by a

corresponding reduction half reaction occurring at the cathode. This movement of electrons from the anode to the cathode results in a charge imbalance about the two electrodes and the formation of an electric field which induces the movement of dissolved ions (*i.e.*, ionic current) to equilibrate the charge distribution in solution. If the solutions about the anode and cathode are separated by an impermeable membrane which may be traversed through a single nanopore, this constriction will function as a resistor to ionic current and thereby impede the flow of electrical current through the entire electrochemical cell. The ionic current through the pore may therefore be detected by simply monitoring the current through the rest of the system.

Should a particle in solution enter the pore due to Brownian motion, pressure, or electric field effects such as electroosmosis or electrophoresis, the flow of ions will be disrupted and a transient decrease in electrical current will be observed with a magnitude dependent on the size of the particle relative to the pore. If the dimensions of the pore are known, this characteristic resistive pulse can be used to detect and size the obstructing particle in a scheme referred to as a Coulter counter[58] as well as determine other properties such as particle concentration, zeta potential, and electrophoretic mobility.[59] Our group has also demonstrated that the extremely high electric field which is concentrated at the pore orifice (on the order of 10^5 V/m, depending on the pore geometry[60]) can further enable open bipolar coupling of redox reactions on translocating metal nanoparticles.[61]

One of the most notable applications of the Coulter counter principle is the sequencing of single-stranded deoxyribonucleic acid (DNA) via the characteristic resistive pulses exhibited by the individual nucleotide bases during translocation.[62] These measurements have most often been carried out using biological nanopores comprised of transport proteins embedded in lipid bilayers, but the use of solid-state nanopores provides an interesting alternative due to the elevated signals

elevated signal levels exhibited by these devices relative to their biological counterparts (over one order of magnitude increase[63]). Solid-state nanopores for DNA sequencing are typically fabricated by drilling a pore several nanometers in diameter through a thin insulating membrane (*e.g.*, Si_3N_4 or SiO_2) supported on a microfabricated chip. Because the free-running translocation of DNA typically occurs at a rate of ~20 megabases per second,[63] current measurements must be carried using bandwidths of ~20 MHz which precludes the use of traditional Si substrates as membrane supports since the capacitance associated with semiconductor/insulator interfaces during high bandwidth measurements results in unacceptably high dielectric noise levels.[64,65] Several studies have reported freestanding membranes suspended on amorphous glass or glass-on-Si substrates, but most use the membrane as a stop layer for dissolution of the underlying material[66–69] which could result in undesired pitting or thinning of the membrane material; others describe manual transfer of the individual membranes to the supporting chips,[65,70–73] thereby impeding mass production of the devices. Chapter 5 closes this dissertation by describing a novel wafer-scale microfabrication process for glass-supported free-standing SiN_x membranes fabricated via direct deposition over apertures in the supporting chips using plasma-enhanced chemical vapor deposition (PECVD) without any intervening transfer or wet etching steps.

1.6 REFERENCES

(1) Polcari, D.; Dauphin-Ducharme, P.; Mauzeroll, J. Scanning Electrochemical Microscopy: A Comprehensive Review of Experimental Parameters from 1989 to 2015. *Chem. Rev.* **2016**, *116*, 13234–13278.

(2) Zhu, C.; Huang, K.; Siepser, N. P.; Baker, L. A. Scanning Ion Conductance Microscopy. *Chem. Rev.* **2020**, acs.chemrev.0c00962.

(3) Bentley, C. L.; Kang, M.; Unwin, P. R. Scanning Electrochemical Cell Microscopy: New Perspectives on Electrode Processes in Action. *Curr. Opin. Electrochem.* **2017**, *6*, 23–30.

(4) Sambur, J. B.; Chen, T.-Y.; Choudhary, E.; Chen, G.; Nissen, E. J.; Thomas, E. M.; Zou, N.; Chen, P. Sub-Particle Reaction and Photocurrent Mapping to Optimize Catalyst-Modified Photoanodes. *Nature* **2016**, *530*, 77–80.

(5) Sambur, J. B.; Chen, P. Distinguishing Direct and Indirect Photoelectrocatalytic Oxidation Mechanisms Using Quantitative Single-Molecule Reaction Imaging and Photocurrent Measurements. *J. Phys. Chem. C* **2016**, *120*, 20668–20676.

(6) Chen, Y.; Zhao, D.; Fu, J.; Gou, X.; Jiang, D.; Dong, H.; Zhu, J.-J. *In Situ* Imaging Facet-Induced Spatial Heterogeneity of Electrocatalytic Reaction Activity at the Subparticle Level via Electrochemiluminescence Microscopy. *Anal. Chem.* **2019**, acs.analchem.9b01044.

(7) Yang, M.; Batchelor-McAuley, C.; Kätelhön, E.; Compton, R. G. Reaction Layer Imaging Using Fluorescence Electrochemical Microscopy. *Anal. Chem.* **2017**, *89*, 6870–6877.

(8) Pruchyathamkorn, J.; Yang, M.; Amin, H. M. A.; Batchelor-McAuley, C.; Compton, R. G. Imaging Electrode Heterogeneity Using Chemically Confined Fluorescence Electrochemical Microscopy. *J. Phys. Chem. Lett.* **2017**, *8*, 6124–6127.

(9) Fuladpanjeh-Hojaghan, B.; Elsutohy, M. M.; Kabanov, V.; Heyne, B.; Trifkovic, M.; Roberts, E. P. L. In-Operando Mapping of PH Distribution in Electrochemical Processes. *Angew. Chem.* **2019**, *131*, 16971–16975.

(10) Wydallis, J. B.; Feeny, R. M.; Wilson, W.; Kern, T.; Chen, T.; Tobet, S.; Reynolds, M. M.; Henry, C. S. Spatiotemporal Norepinephrine Mapping Using a High-Density CMOS Microelectrode Array. *Lab. Chip* **2015**, *15*, 4075–4082.

(11) Dragas, J.; Viswam, V.; Shadmani, A.; Chen, Y.; Bounik, R.; Stettler, A.; Radivojevic, M.; Geissler, S.; Obien, M. E. J.; Müller, J.; Hierlemann, A. In Vitro Multi-Functional Microelectrode Array Featuring 59 760 Electrodes, 2048 Electrophysiology Channels, Stimulation, Impedance Measurement, and Neurotransmitter Detection Channels. *IEEE J. Solid-State Circuits* **2017**, *52*, 1576–1590.

(12) Tedjo, W.; Nejad, J. E.; Feeny, R.; Yang, L.; Henry, C. S.; Tobet, S.; Chen, T. Electrochemical Biosensor System Using a CMOS Microelectrode Array Provides High Spatially and Temporally Resolved Images. *Biosens. Bioelectron.* **2018**, *114*, 78–88.

(13) Viswam, V.; Bounik, R.; Shadmani, A.; Dragas, J.; Urwyler, C.; Boos, J. A.; Obien, M. E. J.; Muller, J.; Chen, Y.; Hierlemann, A. Impedance Spectroscopy and Electrophysiological Imaging of Cells With a High-Density CMOS Microelectrode Array System. *IEEE Trans. Biomed. Circuits Syst.* **2018**, *12*, 1356–1368.

(14) Tedjo, W.; Chen, T. An Integrated Biosensor System With a High-Density Microelectrode Array for Real-Time Electrochemical Imaging. *IEEE Trans. Biomed. Circuits Syst.* **2020**, *14*, 20–35.

(15) Mavré, F.; Anand, R. K.; Laws, D. R.; Chow, K.-F.; Chang, B.-Y.; Crooks, J. A.; Crooks, R. M. Bipolar Electrodes: A Useful Tool for Concentration, Separation, and Detection of Analytes in Microelectrochemical Systems. *Anal. Chem.* **2010**, *82*, 8766–8774.

(16) Chow, K.-F.; Chang, B.-Y.; Zaccheo, B. A.; Mavré, F.; Crooks, R. M. A Sensing Platform Based on Electrodissolution of a Ag Bipolar Electrode. *J. Am. Chem. Soc.* **2010**, *132*, 9228–9229.

(17) Fosdick, S. E.; Crooks, R. M. Bipolar Electrodes for Rapid Screening of Electrocatalysts. *J. Am. Chem. Soc.* **2012**, *134*, 863–866.

(18) Fosdick, S. E.; Berglund, S. P.; Mullins, C. B.; Crooks, R. M. Parallel Screening of Electrocatalyst Candidates Using Bipolar Electrochemistry. *Anal. Chem.* **2013**, *85*, 2493–2499.

(19) Fosdick, S. E.; Berglund, S. P.; Mullins, C. B.; Crooks, R. M. Evaluating Electrocatalysts for the Hydrogen Evolution Reaction Using Bipolar Electrode Arrays: Bi- and Trimetallic Combinations of Co, Fe, Ni, Mo, and W. *ACS Catal.* **2014**, *4*, 1332–1339.

(20) Guerrette, J. P.; Oja, S. M.; Zhang, B. Coupled Electrochemical Reactions at Bipolar Microelectrodes and Nanoelectrodes. *Anal. Chem.* **2012**, *84*, 1609–1616.

(21) Cox, J. T.; Guerrette, J. P.; Zhang, B. Steady-State Voltammetry of a Microelectrode in a Closed Bipolar Cell. *Anal. Chem.* **2012**, *84*, 8797–8804.

(22) Guerrette, J. P.; Percival, S. J.; Zhang, B. Fluorescence Coupling for Direct Imaging of Electrocatalytic Heterogeneity. *J. Am. Chem. Soc.* **2013**, *135*, 855–861.

(23) Oja, S. M.; Guerrette, J. P.; David, M. R.; Zhang, B. Fluorescence-Enabled Electrochemical Microscopy with Dihydroresorufin as a Fluorogenic Indicator. *Anal. Chem.* **2014**, *86*, 6040–6048.

(24) Oja, S. M.; Zhang, B. Imaging Transient Formation of Diffusion Layers with Fluorescence-Enabled Electrochemical Microscopy. *Anal. Chem.* **2014**, *86*, 12299–12307.

(25) Qi, H.; Zhang, C. Electrogenerated Chemiluminescence Biosensing. *Anal. Chem.* **2020**, *92*, 524–534.

(26) Chow, K.-F.; Mavré, F.; Crooks, J. A.; Chang, B.-Y.; Crooks, R. M. A Large-Scale, Wireless Electrochemical Bipolar Electrode Microarray. *J. Am. Chem. Soc.* **2009**, *131*, 8364–8365.

(27) Wu, M.-S.; Liu, Z.; Shi, H.-W.; Chen, H.-Y.; Xu, J.-J. Visual Electrochemiluminescence Detection of Cancer Biomarkers on a Closed Bipolar Electrode Array Chip. *Anal. Chem.* **2015**, *87*, 530–537.

(28) Zhai, Q.; Zhang, X.; Han, Y.; Zhai, J.; Li, J.; Wang, E. A Nanoscale Multichannel Closed Bipolar Electrode Array for Electrochemiluminescence Sensing Platform. *Anal. Chem.* **2016**, *88*, 945–951.

(29) Iwama, T.; Inoue, K. Y.; Abe, H.; Matsue, T. Chemical Imaging Using a Closed Bipolar Electrode Array. *Chem. Lett.* **2018**, *47*, 843–845.

(30) Ino, K.; Yaegaki, R.; Hiramoto, K.; Nashimoto, Y.; Shiku, H. Closed Bipolar Electrode Array for On-Chip Analysis of Cellular Respiration by Cell Aggregates. *ACS Sens.* **2020**, *5*, 740–745.

(31) Safizadeh, F.; Ghali, E.; Houlachi, G. Electrocatalysis Developments for Hydrogen Evolution Reaction in Alkaline Solutions – A Review. *Int. J. Hydrog. Energy* **2015**, *40*, 256–274.

(32) Yang, W.; Chen, S. Recent Progress in Electrode Fabrication for Electrocatalytic Hydrogen Evolution Reaction: A Mini Review. *Chem. Eng. J.* **2020**, *393*, 124726.

(33) Smotkin, E. S.; Díaz-Morales, R. R. New Electrocatalysts by Combinatorial Methods. *Annu. Rev. Mater. Res.* **2003**, *33*, 557–579.

(34) Jeon, M. K.; Lee, C. H.; Park, G. I.; Kang, K. H. Combinatorial Search for Oxygen Reduction Reaction Electrocatalysts: A Review. *J. Power Sources* **2012**, *216*, 400–408.

(35) Antolini, E. Evaluation of the Optimum Composition of Low-Temperature Fuel Cell Electrocatalysts for Methanol Oxidation by Combinatorial Screening. *ACS Comb. Sci.* **2017**, *19*, 47–54.

(36) Guerin, S.; Hayden, B. E.; Lee, C. E.; Mormiche, C.; Owen, J. R.; Russell, A. E.; Theobald, B.; Thompsett, D. Combinatorial Electrochemical Screening of Fuel Cell Electrocatalysts. *J. Comb. Chem.* **2004**, *6*, 149–158.

(37) Smotkin, E. S.; Jiang, J.; Nayar, A.; Liu, R. High-Throughput Screening of Fuel Cell Electrocatalysts. *Appl. Surf. Sci.* **2006**, *252*, 2573–2579.

(38) Reddington, E. Combinatorial Electrochemistry: A Highly Parallel, Optical Screening Method for Discovery of Better Electrocatalysts. *Science* **1998**, *280*, 1735–1737.

(39) Jayaraman, S.; Hillier, A. C. Screening the Reactivity of $Pt_x Ru_y$ and $Pt_x Ru_y Mo_z$ Catalysts toward the Hydrogen Oxidation Reaction with the Scanning Electrochemical Microscope. *J. Phys. Chem. B* **2003**, *107*, 5221–5230.

(40) Fernández, J. L.; White, J. M.; Sun, Y.; Tang, W.; Henkelman, G.; Bard, A. J. Characterization and Theory of Electrocatalysts Based on Scanning Electrochemical Microscopy Screening Methods. *Langmuir* **2006**, *22*, 10426–10431.

(41) Guerin, S.; Hayden, B. E. Physical Vapor Deposition Method for the High-Throughput Synthesis of Solid-State Material Libraries. *J. Comb. Chem.* **2006**, *8*, 66–73.

(42) Prochaska, M.; Jin, J.; Rochefort, D.; Zhuang, L.; DiSalvo, F. J.; Abruña, H. D.; van Dover, R. B. High Throughput Screening of Electrocatalysts for Fuel Cell Applications. *Rev. Sci. Instrum.* **2006**, *77*, 054104.

(43) Guerin, S.; Hayden, B. E.; Lee, C. E.; Mormiche, C.; Russell, A. E. High-Throughput Synthesis and Screening of Ternary Metal Alloys for Electrocatalysis. *J. Phys. Chem. B* **2006**, *110*, 14355–14362.

(44) Latyshev, V.; Vorobiov, S.; Shylenko, O.; Komanicky, V. Screening of Electrocatalysts for Hydrogen Evolution Reaction Using Bipolar Electrodes Fabricated by Composition Gradient Magnetron Sputtering. *J. Electroanal. Chem.* **2019**, *854*, 113562.

(45) Yang, Y.; Chen, G.; Zeng, R.; Villarino, A. M.; DiSalvo, F. J.; van Dover, R. B.; Abruña, H. D. Combinatorial Studies of Palladium-Based Oxygen Reduction Electrocatalysts for Alkaline Fuel Cells. *J. Am. Chem. Soc.* **2020**, *142*, 3980–3988.

(46) Liang, Y.; Pfisterer, J. H. K.; McLaughlin, D.; Csoklich, C.; Seidl, L.; Bandarenka, A. S.; Schneider, O. Electrochemical Scanning Probe Microscopies in Electrocatalysis. *Small Methods* **2019**, *3*, 1800387.

(47) Sullivan, M. G.; Utomo, H.; Fagan, P. J.; Ward, M. D. Automated Electrochemical Analysis with Combinatorial Electrode Arrays. *Anal. Chem.* **1999**, *71*, 4369–4375.

(48) Xiang, C.; Suram, S. K.; Haber, J. A.; Guevarra, D. W.; Soedarmadji, E.; Jin, J.; Gregoire, J. M. High-Throughput Bubble Screening Method for Combinatorial Discovery of Electrocatalysts for Water Splitting. *ACS Comb. Sci.* **2014**, *16*, 47–52.

(49) Brace, K. M.; Hayden, B. E.; Russell, A. E.; Owen, J. R. A Parallel Optical Screen for the Rapid Combinatorial Electrochromic Analysis of Electrochemical Materials. *Adv. Mater.* **2006**, *18*, 3253–3257.

(50) Jaramillo, T. F.; Ivanovskaya, A.; McFarland, E. W. High-Throughput Screening System for Catalytic Hydrogen-Producing Materials. *J. Comb. Chem.* **2002**, *4*, 17–22.

(51) Spong, A. D.; Vitins, G.; Guerin, S.; Hayden, B. E.; Russell, A. E.; Owen, J. R. Combinatorial Arrays and Parallel Screening for Positive Electrode Discovery. *J. Power Sources* **2003**, *119–121*, 778–783.

(52) Strasser, P.; Fan, Q.; Devenney, M.; Weinberg, W. H.; Liu, P.; Nørskov, J. K. High Throughput Experimental and Theoretical Predictive Screening of Materials − A Comparative Study of Search Strategies for New Fuel Cell Anode Catalysts. *J. Phys. Chem. B* **2003**, *107*, 11013–11021.

(53) Dang, T.; Ramsaran, R.; Roy, S.; Froehlich, J.; Wang, J.; Kubiak, C. P. Design of a High Throughput 25-Well Parallel Electrolyzer for the Accelerated Discovery of CO2 Reduction Catalysts via a Combinatorial Approach. *Electroanalysis* **2011**, *23*, 2335–2342.

(54) Zhang, Y.; McGinn, P. J. Combinatorial Screening for Methanol Oxidation Catalysts in Alloys of Pt, Cr, Co and V. *J. Power Sources* **2012**, *206*, 29–36.

(55) Termebaf, H.; Shayan, M.; Kiani, A. Two-Step Bipolar Electrochemistry: Generation of Composition Gradient and Visual Screening of Electrocatalytic Activity. *Langmuir* **2015**, *31*, 13238–13246.

(56) Lin, X.; Zheng, L.; Gao, G.; Chi, Y.; Chen, G. Electrochemiluminescence Imaging-Based High-Throughput Screening Platform for Electrocatalysts Used in Fuel Cells. *Anal. Chem.* **2012**, *84*, 7700–7707.

(57) Zhang, J.-D.; Hao, N.; Lu, L.; Yun, S.; Zhu, X.-F.; Hong, K.; Feng, L.-D. High-Efficient Preparation and Screening of Electrocatalysts Using a Closed Bipolar Electrode Array System. *J. Electroanal. Chem.* **2019**, *832*, 1–6.

(58) Coulter, W. H. Means for Counting Particles Suspended in a Fluid. US2656508A, October 20, 1953.

(59) Luo, L.; German, S. R.; Lan, W.-J.; Holden, D. A.; Mega, T. L.; White, H. S. Resistive-Pulse Analysis of Nanoparticles. *Annu. Rev. Anal. Chem.* **2014**, *7*, 513–535.

(60) Lan, W.-J.; Holden, D. A.; Zhang, B.; White, H. S. Nanoparticle Transport in Conical-Shaped Nanopores. *Anal. Chem.* **2011**, *83*, 3840–3847.

(61) Han, C.; Hao, R.; Fan, Y.; Edwards, M. A.; Gao, H.; Zhang, B. Observing Transient Bipolar Electrochemical Coupling on Single Nanoparticles Translocating through a Nanopore. *Langmuir* **2019**, *35*, 7180–7190.

(62) Haque, F.; Li, J.; Wu, H.-C.; Liang, X.-J.; Guo, P. Solid-State and Biological Nanopore for Real-Time Sensing of Single Chemical and Sequencing of DNA. *Nano Today* **2013**, *8*, 56–74.

(63) Balan, A.; Machielse, B.; Niedzwiecki, D.; Lin, J.; Ong, P.; Engelke, R.; Shepard, K. L.; Drndić, M. Improving Signal-to-Noise Performance for DNA Translocation in Solid-State Nanopores at MHz Bandwidths. *Nano Lett.* **2014**, *14*, 7215–7220.

(64) Uram, J. D.; Ke, K.; Mayer, M. Noise and Bandwidth of Current Recordings from Submicrometer Pores and Nanopores. *ACS Nano* **2008**, *2*, 857–872.

(65) Pitchford, W. H.; Kim, H.-J.; Ivanov, A. P.; Kim, H.-M.; Yu, J.-S.; Leatherbarrow, R. J.; Albrecht, T.; Kim, K.-B.; Edel, J. B. Synchronized Optical and Electronic Detection of Biomolecules Using a Low Noise Nanopore Platform. *ACS Nano* **2015**, *9*, 1740–1748.

(66) Yanagi, I.; Akahori, R.; Hatano, T.; Takeda, K. Fabricating Nanopores with Diameters of Sub-1 Nm to 3 Nm Using Multilevel Pulse-Voltage Injection. *Sci. Rep.* **2015**, *4*, 5000.

(67) Balan, A.; Chien, C.-C.; Engelke, R.; Drndić, M. Suspended Solid-State Membranes on Glass Chips with Sub 1-PF Capacitance for Biomolecule Sensing Applications. *Sci. Rep.* **2016**, *5*, 17775.

(68) de Vreede, L. J.; Ying, C.; Houghtaling, J.; Figueiredo Da Silva, J.; Hall, A. R.; Lovera, A.; Mayer, M. Wafer-Scale Fabrication of Fused Silica Chips for Low-Noise Recording of Resistive Pulses through Nanopores. *Nanotechnology* **2019**, *30*, 265301.

(69) Xia, P.; Zuo, J.; Paudel, P.; Choi, S.; Chen, X.; Rahman Laskar, M. A.; Bai, J.; Song, W.; Im, J.; Wang, C. Sapphire-Supported Nanopores for Low-Noise DNA Sensing. *Biosens. Bioelectron.* **2021**, *174*, 112829.

(70) Merchant, C. A.; Healy, K.; Wanunu, M.; Ray, V.; Peterman, N.; Bartel, J.; Fischbein, M. D.; Venta, K.; Luo, Z.; Johnson, A. T. C.; Drndić, M. DNA Translocation through Graphene Nanopores. *Nano Lett.* **2010**, *10*, 2915–2921.

(71) Schneider, G. F.; Kowalczyk, S. W.; Calado, V. E.; Pandraud, G.; Zandbergen, H. W.; Vandersypen, L. M. K.; Dekker, C. DNA Translocation through Graphene Nanopores. *Nano Lett.* **2010**, *10*, 3163–3167.

(72) Lee, M.-H.; Kumar, A.; Park, K.-B.; Cho, S.-Y.; Kim, H.-M.; Lim, M.-C.; Kim, Y.-R.; Kim, K.-B. A Low-Noise Solid-State Nanopore Platform Based on a Highly Insulating Substrate. *Sci. Rep.* **2015**, *4*, 7448.

(73) Zhang, X.; van Deursen, P. M. G.; Fu, W.; Schneider, G. F. Facile and Ultraclean Graphene-on-Glass Nanopores by Controlled Electrochemical Etching. *ACS Sens.* **2020**, *5*, 2317–2325.

Chapter 2

SUBMICRON BIPOLAR ELECTRODE ARRAYS VIA LASER INTERFERENCE LITHOGRAPHY

2.1 INTRODUCTION

Electroanalytical methods in which the current response of an electrode held under a potential bias is used to monitor the local environment about the electrode are an excellent tool for the study of dynamic redox systems. Indeed, methods such as chronoamperometry have been widely utilized to investigate transient electrochemical phenomena ranging from discrete neurotransmitter exocytosis events[1,2] to single nanoparticle collisions on the surface of an ultramicroelectrode (UME).[3–5] However, while the temporal resolution of such techniques is able to reach submillisecond levels,[6,7] no spatial information about the system of interest is gained without taking measurements at multiple locations. Scanning probe methods such as scanning electrochemical microscopy (SECM),[8] scanning ion conductance microscopy (SICM),[9] and scanning electrochemical cell microscopy (SECCM)[10] have been proposed to address this shortcoming, but all suffer from loss of temporal resolution due to the requisite scanning time. Individually addressable electrode arrays in which each element acts as a separate data channel provide an excellent alternative for imaging the electrochemical activity of spatially and temporally heterogenous redox systems,[11–15] but size of the data generated in such a scheme necessitates compromises between the imaging area, spatial resolution, and bandwidth. Fabrication of large and dense arrays is also very challenging due to the large number of leads which is required to make electrical contact with all of the constituent electrodes. An alternative strategy for monitoring the electrical current through the individual electrodes of an array in parallel is therefore of great utility in achieving high spatial and temporal imaging resolution.

Fluorescence-enabled electrochemical microscopy (FEEM) is an electrochemical imaging technique previously introduced by our group to address this parallelization issue by enabling optical reading of the current through dense electrode arrays.[16] In this method, an electric field is applied across a floating-potential conductor connecting two segregated solutions to couple a redox reaction of interest to a complementary fluorogenic indicator reaction (initially resazurin reduction fluorescent resorufin to monitor oxidation reactions, but eventually extended to dihydroresorufin oxidation for reduction reactions[17]). Electrons passing through such a closed bipolar electrode (BPE) thereby yield an optical signal which enables virtually any electrochemical process to be monitored via a fluorescent signal. The sensitivity of this scheme is also greater than would otherwise be achievable through the collection of electric current alone due to signal amplification from the continual stream of photons that is generated for each electron (see **Scheme 2.1**). Electrochemical imaging may be carried out using this technique if a large number of bipolar electrodes are arranged in parallel to form an array. Indeed, arrays of thousands of ~6 μm diameter carbon fibers (CFs) insulated with epoxy have already been used by our group to image electrochemical processes including the relative electrocatalytic activity of Pt deposited on the surface of a CF array[16] and the diffusion profile about a 10 μm diameter CF electrode.[18] However, due to uneven electrochemical response and poor uniformity arising from aggregation and crosstalk between the constituent fibers, ordered arrays of miniscule electrodes are desirable to expand the range of research targets which may be investigated using FEEM.

To this end, laser interference lithography (LIL) has been employed to produce high-resolution arrays comprised of thousands of electrodes. This maskless photolithographic technique has been widely utilized since its introduction in 1978[19] for the production of large-scale patterns of repeating nanoscale structures,[20] with a number of applications appearing in the field of

plasmonics.[21–23] LIL is carried out by mounting a substrate coated in a thin photoresist film to a stage on which a mirror has been affixed perpendicular to the sample. An expanding laser beam is then directed toward the stage so that light is reflected by the mirror to the substrate at the same angle as the directly incident light (**Scheme 2.2a**, the "Lloyd's mirror" configuration). Interference between intersecting wavefronts from both beams results in the formation of a pattern of regularly spaced bright and dark fringes, the period of which is given by **Equation 2.1** below,

$$\Lambda = \frac{\lambda}{2 \sin \theta} \qquad (2.1)$$

where λ is the wavelength of the laser and θ is the angle of incidence of the laser on the mirror. If the resist surface is subjected to two separate exposures oriented 90° to one another, grid patterns exhibiting size and spacing on the same order as the laser wavelength may be generated for use as electrode array templates (see **Scheme 2.2b**). Indeed, LIL has been applied to the fabrication of large metal nanoelectrode and nanostructure arrays,[24–27] but none of these arrays are comprised of individually addressable electrodes. Standard micromachining processes have therefore been utilized in conjunction with LIL patterning to produce arrays of thousands of individually addressable submicron BPEs.

2.2 Experimental Section

2.2.1 *Chip Fabrication*

A (100) Si wafer (Rogue Valley Microdevices) coated in 1 μm low-pressure chemical vapor deposited (LPCVD) SiN_x was first RCA cleaned by immersion for 10 min in a 1:1:5 (NH_4OH:H_2O_2:H_2O) solution @ 75°C followed by 10 minutes in a 1:1:6 (HCl:H_2O_2:H_2O) solution @ 75°C. This wafer was then treated in a hexamethyldisilazane (HMDS) oven to promote resist adhesion and then spin coated with AZ 5214E (Microchemicals) @ 4000 rpm and patterned via

photolithography using a custom mask (Photosciences). The exposed nitride was dry etched with a Vision RIE parallel-plate reactive ion etcher using a recipe of 10 sccm CHF_3 and 40 sccm CF_4 @ 40 mtorr and 225 W, after which the wafer was anisotropically etched in a 30% KOH solution to yield 50x 1 cm × 1 cm chips with a 50 μm × 50 μm SiN_x window exposed in the center of each. A 200 nm Al film was then deposited on the chips to completely coat the underside of the windows using a custom built thermal evaporator.

2.2.2 *BPE Array Fabrication*

After an initial RCA clean step, 35 nm of Cr was thermally evaporated directly onto the SiN_x surface of the windowed chips, after which the chips were dehydrated on a hot plate for 20 minutes @ 200°C before being spin-coated twice with a 1:4 (HMDS:PGMEA) solution @ 4000 rpm, once with 1:1 (AZ 1505:PGMEA) (Microchemicals) @ 4000 rpm, and then soft-baked for 1 min to evaporate excess solvent. The coated chips were then mounted perpendicular to a UV-reflective mirror (Thorlabs) and exposed twice with a 90° rotation of the chip carried out between exposures using an IK3201R-F 325 nm HeCd laser (KIMMON KOHA) mounted 122 in. from the sample stage. Exposures were carried out with the mirror oriented 11.4° to the incident laser beam. A spatial filter with a 13x objective and a 10 μm pinhole (Newport) mounted 59 in. from the laser was used to clean and expand the beam. Exposure time was controlled using a Model T132 shutter driver/timer (Vincent Assoc.) mounted between the spatial filter and the sample stage. The energy dose delivered to the sample surface was calculated to be 10.0 mJ/cm^2 using a PM100D power meter (Thorlabs). Subsequent to exposure, the chips were developed by immersion in AZ 300 MIF (Microchemicals) for 1 min, followed by two rinses in DI water for 1 min each. The patterned surfaces were descummed via 27.5 sccm O_2 plasma @ 40 mtorr and 60 W to generate arrays of holes using a Solarus Advanced Plasma Clean System (Gatan), after which the base Cr film on

each chip was etched by covering the surface with Cr 1020 chromium etchant (Transene) for 20 sec followed by two DI water rinses for 1 min each. The photoresist was then removed by immersion in acetone for 5 min followed by 20 min of O_2 plasma cleaning (same parameters as listed above). The patterned Cr layers were then used to etch the underlying SiN_x windows in the Si chips with the same RIE instrument and nitride etch recipe which has been previously described. Layers of Au (50 nm) and Ti (650 nm) were then deposited onto the chips to fill the holes using an SEC-600 e-beam evaporator (CHA Industries), after which the overlying metal films were lifted off by immersion in Cr 1020 etchant for ~24 hrs. As a final step, the Al backing on each window was removed by applying a 73% : 3.1% : 3.3% : 20.6% (H_3PO_4:HNO_3:CH_3COOH:H_2O) solution to the backside of the chips for 10 min.

2.2.3 *Cyclic Voltammetry and Fluorescence Coupling*

Potential was driven across the arrays using an EG&G Princeton Applied Research Model 175 universal programmer with two Ag/AgCl electrodes. Wires were freshly chlorided prior to each experiment using a 1:1 solution of 70% HNO_3 and 3 M KCl. The fluorescence coupling experiment was recorded using an Andor Luca S 658M EMCCD cooled to -20 ^oC with 30 ms exposure, 0.6 µs vertical pixel shift speed, and 13.5 MHz readout rate. Videos contained 1000 frames with a maximum resolution of 658×496 pixels which was cropped to the array surface. An Olympus IX70 inverted microscope with a 1000x objective was used to image the array. All videos were analyzed using ImageJ.

Arrays were prepared for use by epoxying the base of a 1 mL plastic pipettor tip cut to ~1 cm in length to the face of each device to contain the solution on the detecting side of the array; the opposite side was immersed in a drop of reporter solution placed on a glass microscope slide. Cyclic voltammetry was carried out using the previously mentioned setup to apply a driving

voltage of -0.2 to 0.6 V vs. Ag/AgCl at 100 mV/s to couple 1 mM ferrocenemethanol 100 mM KCl to 1 mM $K_3[Fe(CN)_6]$ 100 mM KCl across the array. Fluorescence coupling was carried out using a driving voltage sweep of 0 to -1 V vs. Ag/AgCl at 100 mV/s to couple the 1 mM $K_3[Fe(CN)_6]$ 100 mM KCl above the array to 50 µM dihydroresorufin 0.5 M NaOH below the array.

2.2.4 *Characterization*

All etching processes were monitored and characterized with a Bruker Dimension Icon atomic force microscope (AFM) using the contact-mode ScanAsyst function. Sample characterization was also carried out on a XL 830 Dual-Beam Scanning Electron Microscope (FEI). Film thicknesses were measured using a Dektak profilometer (Bruker).

2.3 Results and Discussion

2.3.1 *Array Fabrication*

SiN_x window chips which have been widely used as nanopore substrates[28–33] and transmission electron microscopy (TEM) sample supports[34–37] were selected as the BPE array substrates due to the low stress of low-pressure chemical vapor deposited (LPCVD) SiN_x which enables the creation of freestanding membranes of nanoscale thickness[38]; this minimal substrate thickness is necessary for the creation of arrays of submicron BPEs due to the challenges associated with depositing metal into very high aspect ratio pores to form the constituent electrodes. Fabrication of these chips was carried out by first patterning a series of 792 µm squares surround by dicing borders through the surface coating of a (100) Si wafer with 1 µm LPCVD SiN_x film on each side using photolithography and reactive ion etching (RIE), after which the wafer was immersed in hot KOH solution. Because KOH preferentially etches the (100) crystal face of Si ~400 times faster than the

(111) crystal face (oriented 54.74° from one another), pyramidal holes were etched through the chips to form 50 μm × 50 μm windows beneath the SiN_x on the opposite side, thereby yielding a series of freestanding membranes; KOH etching of the dicing borders also released the individual chips from the wafer.

To facilitate fabrication of BPE arrays in the suspended SiN_x membranes (see **Scheme 2.3**), a layer of Cr was evaporated over the upper flat surface of each chip and a layer of Al over the opposite KOH etched side, after which the chip was spin coated with photoresist and exposed twice via LIL with a 90° rotation carried out between the exposures. The resulting arrayed hole pattern was transferred into the Cr film by wet etching to form a hard mask for RIE of the underlying window to the Al on the opposite side. **Figure 2.1a** shows an example of the RIE results with a cross-section of an etched pore shown in **Figure 2.1b**. Note the verticality of the sidewalls which is characteristic of the anisotropic dry etching. Au (50 nm) and Ti (650 nm) were then evaporated over the surface and into the etched holes where the Al backing enabled accumulation of the deposited metal and prevented it from passing straight through the etched membrane. Ti was used instead of Au alone to enhance adhesion to the surrounding SiN_x and to reduce the cost of such a thick metal film; Au was used for the anodic poles of the electrodes to eliminate the possibility of Ti oxidation on this surface. Note that it was necessary to carry out the Ti evaporation at a relatively slow rate (0.7 Å/s) to minimize gradual constriction of the pores during deposition (**Figure A1**) which resulted in a conical electrode geometry (**Figure A2**). The fabrication process was finished by removing the Al backing and lifting off the Au/Ti layer on the upper chip surface via dissolution of the underlying Cr. The resulting arrays consist of ~3900 BPEs (500 nm diameter, 800 nm period) arranged in a rectangular lattice configuration. Scanning electron microscopy (SEM) imaging of the array surface revealed well-ordered arrays of distinct BPEs and with no

residual metal bridging between any of the electrodes on the upper insulator surface after lift off (**see Figures 2.2a,b**). The absence of any apparent missing electrodes indicates that good adhesion was achieved between the deposited metal and the SiN_x sidewalls. **Figures 2.2c** shows a completed device with the LIL-patterned region in the center exhibiting the observed iridescence. Note that while this portion of the surface is ~25 mm^2 in area, the actual electroactive surface of the bipolar array (shown in **Figure 2.2d**) is limited by the mechanical stability of the freestanding membrane and comprises only ~0.01% of the patterned region.

2.3.2 *Cyclic Voltammetry and Fluorescence Coupling*

Initial electrochemical characterization of these BPE arrays was carried out via cyclic voltammetry (CV) to couple ferrocenemethanol oxidation to $Fe(CN)_6^{3-}$ reduction. While the CV shown in **Figure A3** demonstrates the onset of coupling at ~0.3 V and reasonable stability over the course of multiple scans, the slant of the preceding baseline indicates leakage of ionic current through the array, likely through a small crack in the insulator or a hole created by a missing electrode. To further test the utility of these BPE arrays as platforms for FEEM imaging, correlated fluorescence cyclic voltammetry (F-CV) was carried out by coupling dihydroresorufin oxidation in basic glucose solution to $Fe(CN)_6^{3-}$ reduction using one of these devices (see **Figure 2.3a**). In this fluorescent reporting scheme, the precursor is oxidized on the reporting poles of the array electrodes to form fluorescent resorufin (λ_{max} = 585 nm) before being quickly reduced back to dihydroresorufin by glucose to prevent the accumulation of fluorescent background.[17] The fluorescence response to the applied potential was monitored on the reporting side of the array using an inverted microscope and was observed to modulate in close correlation with the applied triangular voltage waveform (see **Figure 2.3b**). Note that the consistent discrepancy observed between the potential and intensity minima is likely due to the applied voltage being scanned below

the driving potential necessary for coupling of the two half reactions; after the scan is reversed, the optical signal continues to decrease as the reporter species is reduced by glucose until the coupling potential is reached and the intensity begins to rise.

Although these initial observations appear somewhat promising, examination of frames from the F-CV video reveals that the fluorescent signal is distributed evenly across the entire surface of the array rather than being confined to the individual electrodes (**Figures 2.3c-e**), an effect which is likely due to free diffusion of the resorufin molecules after generation. If the mass transport of this species is approximated as two-dimensional diffusion at the array surface, the mean displacement of a reporter molecule from its point of origin in a given time *t* is given by **Equation 2.2**,

$$x = 2\sqrt{Dt} \qquad (\mathbf{2.2})$$

where *D* is the diffusion coefficient of the molecule. Given the diffusion coefficient of 4.8×10^{-6} cm^2/s for resorufin[39] and a camera exposure time of 30 ms which was utilized for fluorescence imaging, the mean displacement of a resorufin molecule at the array surface during the collection of a single video frame is ~7.6 μm. This means that each reporter molecule was able to diffuse up to 9.5 times the period of the array while its optical signal was being detected, thereby lowering the effective imaging resolution of the entire system by a factor of ~19. Fluorescence-coupling therefore seems to be poorly suited as a means of reading the current through BPE arrays of submicron resolution.

Several strategies to limit diffusion of the reporter species and enable imaging at the maximum resolution of the array are currently being investigated. The most direct solution to this issue is immobilization of the fluorescent reporter molecules in some sort of polymer matrix spread on the surface of the array so as to preconcentrate the fluorogenic precursor on the array surface

and localize any optical signal to its electrode of origin. Such a scheme could create other problems, however, since depletion of the confined fluorophore precursor would result in a permanent decrease in local concentration of this species at the array surface which could in turn limit the current generated by the coupled reaction of interest. Increasing the viscosity of the reporter solution to slow diffusion of the reporter molecules presents similar complications since mass transport of the precursor species to the array surface would also be impeded which would also limit the current through the array. The use of an electrochemiluminescence (ECL) reporter reaction for macroscale closed bipolar systems has also been reported in the literature[40–42] and provides a promising alternative to fluorescence for high resolution imaging since light is not generated via continual excitation of an untethered fluorophore but rather by the immediate relaxation of an excited species generated at the electrode surface which also results in zero background accumulation. Such an imaging scheme is discussed in greater detail in Chapter 3.

2.4 CONCLUSIONS

In this unpublished work, LIL was used in conjunction with standard micromachining processes to fabricate SiN_x-insulated closed bipolar electrode arrays consisting of thousands of individually addressable submicron metal electrodes for use in FEEM imaging. These arrays were successfully used to detect the reduction of $Fe(CN)_6^{3-}$ via coupling to fluorogenic dihydroresorufin oxidation. However, the resulting optical signal was not localized to the individual electrodes due to free diffusion of the reporter molecules, thereby greatly lowering the effective imaging resolution which could be achieved with these devices. The use of an ECL reporter reaction to address this shortcoming is explored in the following chapter. A flexible polymer array substrate is also introduced to overcome the size limitations and fragility of the SiN_x membranes used in these devices.

2.5 REFERENCES

(1) Liu, X.; Tong, Y.; Fang, P.-P. Recent Development in Amperometric Measurements of Vesicular Exocytosis. *TrAC Trends Anal. Chem.* **2019**, *113*, 13–24.

(2) Guille-Collignon, M.; Lemaître, F. Recent Developments Concerning the Investigation of Exocytosis with Amperometry. *Curr. Opin. Electrochem.* **2021**, *29*, 100751.

(3) Peng, Y.-Y.; Qian, R.-C.; Hafez, M. E.; Long, Y.-T. Stochastic Collision Nanoelectrochemistry: A Review of Recent Developments. *ChemElectroChem* **2017**, *4*, 977–985.

(4) Xu, W.; Zou, G.; Hou, H.; Ji, X. Single Particle Electrochemistry of Collision. *Small* **2019**, *15*, 1804908.

(5) Defnet, P. A.; Anderson, T. J.; Zhang, B. Stochastic Collision Electrochemistry of Single Silver Nanoparticles. *Curr. Opin. Electrochem.* **2020**, *22*, 129–135.

(6) Zhang, B.; Heien, M. L. A. V.; Santillo, M. F.; Mellander, L.; Ewing, A. G. Temporal Resolution in Electrochemical Imaging on Single PC12 Cells Using Amperometry and Voltammetry at Microelectrode Arrays. *Anal. Chem.* **2011**, *83*, 571–577.

(7) Defnet, P. A.; Han, C.; Zhang, B. Temporally-Resolved Ultrafast Hydrogen Adsorption and Evolution on Single Platinum Nanoparticles. *Anal. Chem.* **2019**, *91*, 4023–4030.

(8) Polcari, D.; Dauphin-Ducharme, P.; Mauzeroll, J. Scanning Electrochemical Microscopy: A Comprehensive Review of Experimental Parameters from 1989 to 2015. *Chem. Rev.* **2016**, *116*, 13234–13278.

(9) Zhu, C.; Huang, K.; Siepser, N. P.; Baker, L. A. Scanning Ion Conductance Microscopy. *Chem. Rev.* **2020**, acs.chemrev.0c00962.

(10) Bentley, C. L.; Kang, M.; Unwin, P. R. Scanning Electrochemical Cell Microscopy: New Perspectives on Electrode Processes in Action. *Curr. Opin. Electrochem.* **2017**, *6*, 23–30.

(11) Wydallis, J. B.; Feeny, R. M.; Wilson, W.; Kern, T.; Chen, T.; Tobet, S.; Reynolds, M. M.; Henry, C. S. Spatiotemporal Norepinephrine Mapping Using a High-Density CMOS Microelectrode Array. *Lab. Chip* **2015**, *15*, 4075–4082.

(12) Dragas, J.; Viswam, V.; Shadmani, A.; Chen, Y.; Bounik, R.; Stettler, A.; Radivojevic, M.; Geissler, S.; Obien, M. E. J.; Müller, J.; Hierlemann, A. In Vitro Multi-Functional Microelectrode Array Featuring 59 760 Electrodes, 2048 Electrophysiology Channels, Stimulation, Impedance Measurement, and Neurotransmitter Detection Channels. *IEEE J. Solid-State Circuits* **2017**, *52*, 1576–1590.

(13) Tedjo, W.; Nejad, J. E.; Feeny, R.; Yang, L.; Henry, C. S.; Tobet, S.; Chen, T. Electrochemical Biosensor System Using a CMOS Microelectrode Array Provides High Spatially and Temporally Resolved Images. *Biosens. Bioelectron.* **2018**, *114*, 78–88.

(14) Viswam, V.; Bounik, R.; Shadmani, A.; Dragas, J.; Urwyler, C.; Boos, J. A.; Obien, M. E. J.; Muller, J.; Chen, Y.; Hierlemann, A. Impedance Spectroscopy and Electrophysiological Imaging of Cells With a High-Density CMOS Microelectrode Array System. *IEEE Trans. Biomed. Circuits Syst.* **2018**, *12*, 1356–1368.

(15) Tedjo, W.; Chen, T. An Integrated Biosensor System With a High-Density Microelectrode Array for Real-Time Electrochemical Imaging. *IEEE Trans. Biomed. Circuits Syst.* **2020**, *14*, 20–35.

(16) Guerrette, J. P.; Percival, S. J.; Zhang, B. Fluorescence Coupling for Direct Imaging of Electrocatalytic Heterogeneity. *J. Am. Chem. Soc.* **2013**, *135*, 855–861.

(17) Oja, S. M.; Guerrette, J. P.; David, M. R.; Zhang, B. Fluorescence-Enabled Electrochemical Microscopy with Dihydroresorufin as a Fluorogenic Indicator. *Anal. Chem.* **2014**, *86*, 6040–6048.

(18) Oja, S. M.; Zhang, B. Imaging Transient Formation of Diffusion Layers with Fluorescence-Enabled Electrochemical Microscopy. *Anal. Chem.* **2014**, *86*, 12299–12307.

(19) Ng, W. W.; Hong, C.-S.; Yariv, A. Holographic Interference Lithography for Integrated Optics. *IEEE Trans. Electron Devices* **1978**, *25*, 1193–1200.

(20) Lu, C.; Lipson, R. H. Interference Lithography: A Powerful Tool for Fabricating Periodic Structures: Interference Lithography. *Laser Photonics Rev.* **2010**, *4*, 568–580.

(21) Gisbert Quilis, N.; Lequeux, M.; Venugopalan, P.; Khan, I.; Knoll, W.; Boujday, S.; Lamy de la Chapelle, M.; Dostalek, J. Tunable Laser Interference Lithography Preparation of Plasmonic Nanoparticle Arrays Tailored for SERS. *Nanoscale* **2018**, *10*, 10268–10276.

(22) Quilis, N. G.; Hageneder, S.; Fossati, S.; Auer, S. K.; Venugopalan, P.; Bozdogan, A.; Petri, C.; Moreno-Cencerrado, A.; Toca-Herrera, J. L.; Jonas, U.; Dostalek, J. UV-Laser Interference Lithography for Local Functionalization of Plasmonic Nanostructures with Responsive Hydrogel. *J. Phys. Chem. C* **2020**, *124*, 3297–3305.

(23) Oh, Y.; Lim, J. W.; Kim, J. G.; Wang, H.; Kang, B.-H.; Park, Y. W.; Kim, H.; Jang, Y. J.; Kim, J.; Kim, D. H.; Ju, B.-K. Plasmonic Periodic Nanodot Arrays *via* Laser Interference Lithography for Organic Photovoltaic Cells with >10% Efficiency. *ACS Nano* **2016**, *10*, 10143–10151.

(24) Du, K.; Wathuthanthri, I.; Mao, W.; Xu, W.; Choi, C.-H. Large-Area Pattern Transfer of Metallic Nanostructures on Glass Substrates via Interference Lithography. *Nanotechnology* **2011**, *22*, 285306.

(25) Kim, T.-H.; Yea, C.-H.; Chueng, S.-T. D.; Yin, P. T.-T.; Conley, B.; Dardir, K.; Pak, Y.; Jung, G. Y.; Choi, J.-W.; Lee, K.-B. Large-Scale Nanoelectrode Arrays to Monitor the Dopaminergic Differentiation of Human Neural Stem Cells. *Adv. Mater.* **2015**, *27*, 6356–6362.

(26) Lee, J.-H.; Choi, H. K.; Yang, L.; Chueng, S.-T. D.; Choi, J.-W.; Lee, K.-B. Nondestructive Real-Time Monitoring of Enhanced Stem Cell Differentiation Using a Graphene-Au Hybrid Nanoelectrode Array. *Adv. Mater.* **2018**, *30*, 1802762.

(27) Kim, D.-S.; Kang, E.-S.; Baek, S.; Choo, S.-S.; Chung, Y.-H.; Lee, D.; Min, J.; Kim, T.-H. Electrochemical Detection of Dopamine Using Periodic Cylindrical Gold Nanoelectrode Arrays. *Sci. Rep.* **2018**, *8*, 14049.

(28) Tabard-Cossa, V.; Trivedi, D.; Wiggin, M.; Jetha, N. N.; Marziali, A. Noise Analysis and Reduction in Solid-State Nanopores. *Nanotechnology* **2007**, *18*, 305505.

(29) Dimitrov, V.; Mirsaidov, U.; Wang, D.; Sorsch, T.; Mansfield, W.; Miner, J.; Klemens, F.; Cirelli, R.; Yemenicioglu, S.; Timp, G. Nanopores in Solid-State Membranes Engineered for Single Molecule Detection. *Nanotechnology* **2010**, *21*, 065502.

(30) Rosenstein, J. K.; Wanunu, M.; Merchant, C. A.; Drndic, M.; Shepard, K. L. Integrated Nanopore Sensing Platform with Sub-Microsecond Temporal Resolution. *Nat. Methods* **2012**, *9*, 487–492.

(31) Balan, A.; Machielse, B.; Niedzwiecki, D.; Lin, J.; Ong, P.; Engelke, R.; Shepard, K. L.; Drndić, M. Improving Signal-to-Noise Performance for DNA Translocation in Solid-State Nanopores at MHz Bandwidths. *Nano Lett.* **2014**, *14*, 7215–7220.

(32) Shekar, S.; Niedzwiecki, D. J.; Chien, C.-C.; Ong, P.; Fleischer, D. A.; Lin, J.; Rosenstein, J. K.; Drndić, M.; Shepard, K. L. Measurement of DNA Translocation Dynamics in a Solid-State Nanopore at 100 Ns Temporal Resolution. *Nano Lett.* **2016**, *16*, 4483–4489.

(33) Chou, Y.-C.; Masih Das, P.; Monos, D. S.; Drndić, M. Lifetime and Stability of Silicon Nitride Nanopores and Nanopore Arrays for Ionic Measurements. *ACS Nano* **2020**, *14*, 6715–6728.

(34) Morkved, T. L.; Lopes, W. A.; Hahm, J.; Sibener, S. J.; Jaeger, H. M. Silicon Nitride Membrane Substrates for the Investigation of Local Structure in Polymer Thin Films. *Polymer* **1998**, *39*, 3871–3875.

(35) Grant, A. W.; Hu, Q.-H.; Kasemo, B. Transmission Electron Microscopy Windows for Nanofabricated Structures. *Nanotechnology* **2004**, *15*, 1175–1181.

(36) Zwickl, B. M.; Shanks, W. E.; Jayich, A. M.; Yang, C.; Bleszynski Jayich, A. C.; Thompson, J. D.; Harris, J. G. E. High Quality Mechanical and Optical Properties of Commercial Silicon Nitride Membranes. *Appl. Phys. Lett.* **2008**, *92*, 103125.

(37) Ring, E. A.; Peckys, D. B.; Dukes, M. J.; Baudoin, J. P.; Jonge, N. D. Silicon Nitride Windows for Electron Microscopy of Whole Cells. *J. Microsc.* **2011**, *243*, 273–283.

(38) Toivola, Y.; Thurn, J.; Cook, R. F.; Cibuzar, G.; Roberts, K. Influence of Deposition Conditions on Mechanical Properties of Low-Pressure Chemical Vapor Deposited Low-Stress Silicon Nitride Films. *J. Appl. Phys.* **2003**, *94*, 6915–6922.

(39) Schilling, E. A.; Kamholz, A. E.; Yager, P. Cell Lysis and Protein Extraction in a Microfluidic Device with Detection by a Fluorogenic Enzyme Assay. *Anal. Chem.* **2002**, *74*, 1798–1804.

(40) Lin, X.; Zheng, L.; Gao, G.; Chi, Y.; Chen, G. Electrochemiluminescence Imaging-Based High-Throughput Screening Platform for Electrocatalysts Used in Fuel Cells. *Anal. Chem.* **2012**, *84*, 7700–7707.

(41) Wu, M.-S.; Liu, Z.; Shi, H.-W.; Chen, H.-Y.; Xu, J.-J. Visual Electrochemiluminescence Detection of Cancer Biomarkers on a Closed Bipolar Electrode Array Chip. *Anal. Chem.* **2015**, *87*, 530–537.

(42) Zhai, Q.; Zhang, X.; Han, Y.; Zhai, J.; Li, J.; Wang, E. A Nanoscale Multichannel Closed Bipolar Electrode Array for Electrochemiluminescence Sensing Platform. *Anal. Chem.* **2016**, *88*, 945–951.

2.6 SCHEMES AND FIGURES

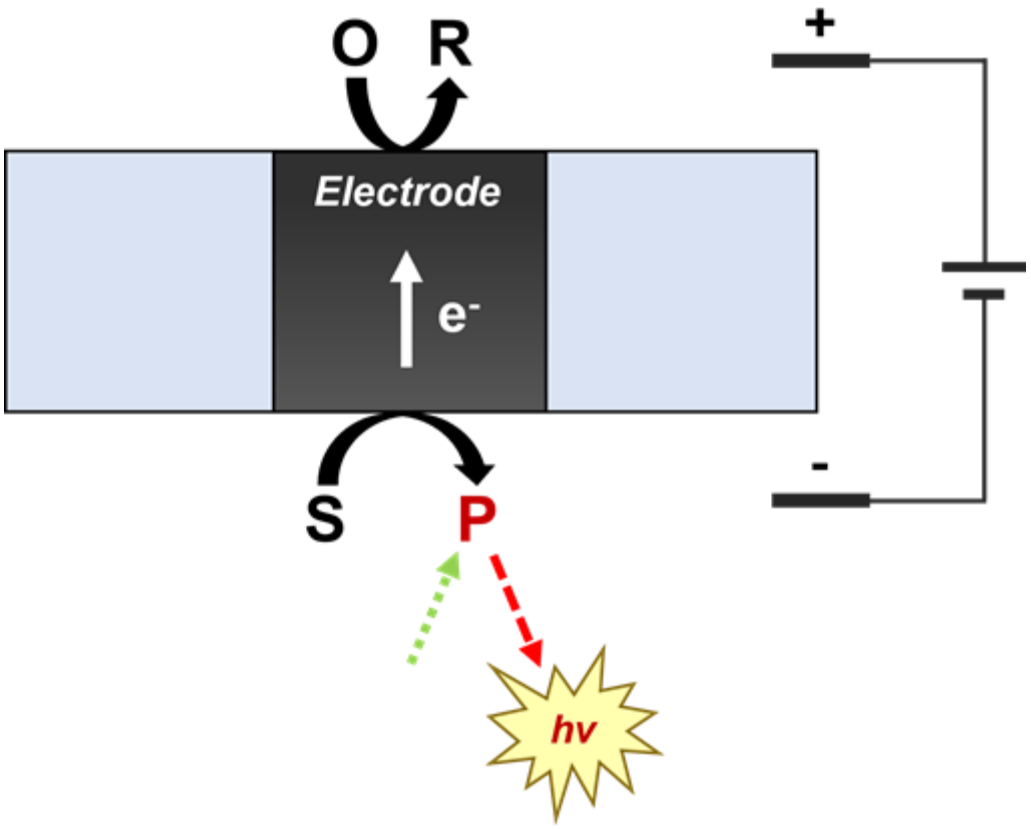

Scheme 2.1. Diagram of FEEM bipolar coupling scheme in which a reduction reaction (O to R) is coupled to a fluorogenic oxidation reaction (S to P).

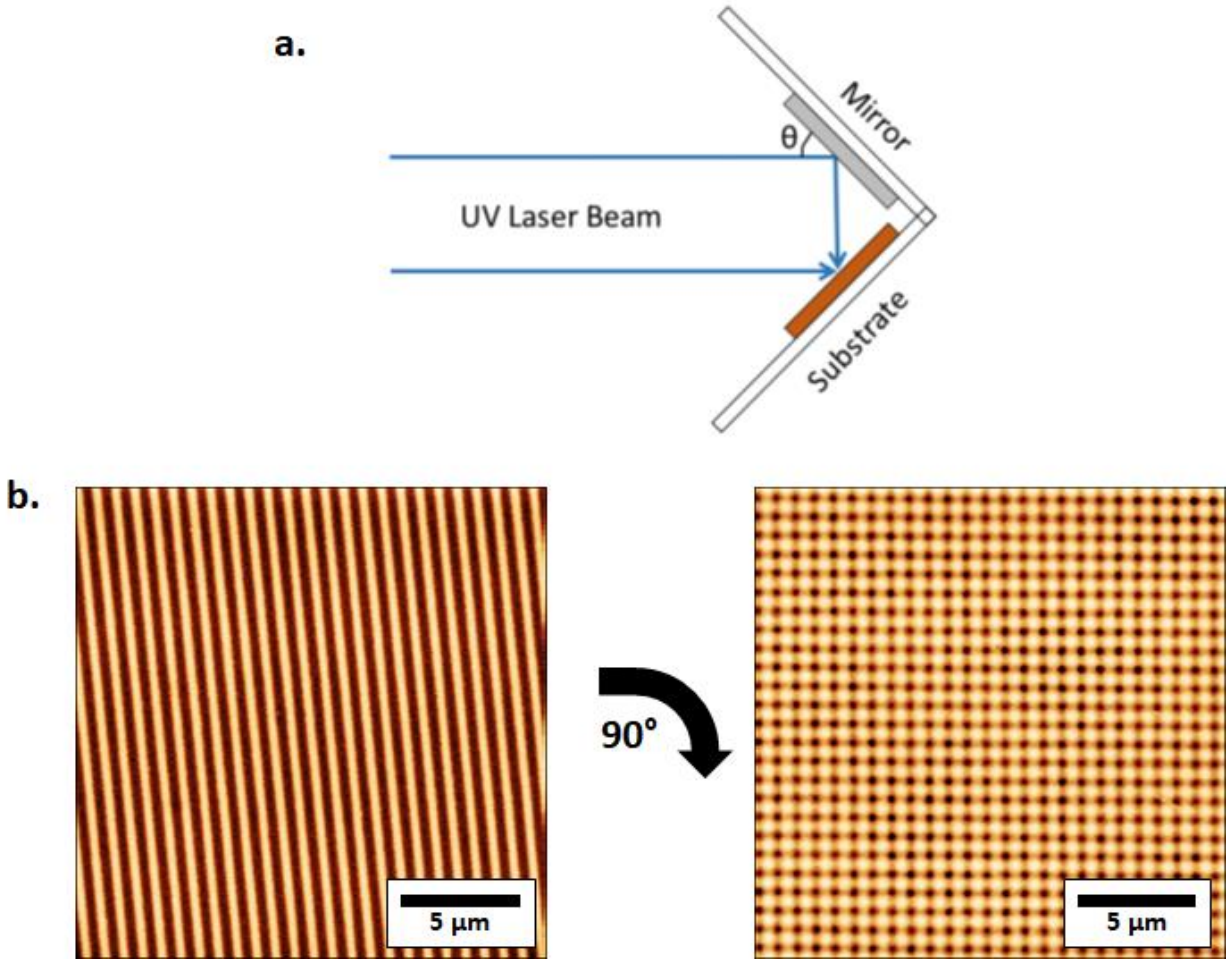

Scheme 2.2. (a) Diagram of Lloyd's mirror LIL setup. (b) Representative AFM images of photoresist patterns after the first (left) and second (right) LIL exposures carried out at a 90° angle to one another.

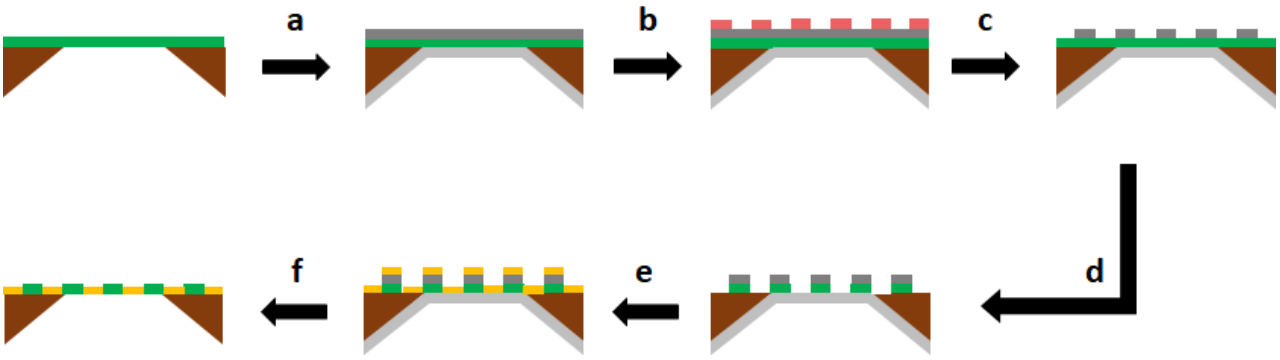

Scheme 2.3. Flowchart of array fabrication scheme. Cr is first evaporated over the top of a SiN_x window chip and Al over the bottom (a), after which the Cr surface is patterned with photoresist via LIL (b) and wet etched (c) to yield a Cr hard mask. This mask is used to plasma etch an array of pores into the underlying SiN_x (d). Au/Ti is evaporated over the surface to fill the pores (e) and then lifted off from the upper surface by dissolution of the underlying Cr to yield a BPE array (f). The lower Al film is also removed during the final step.

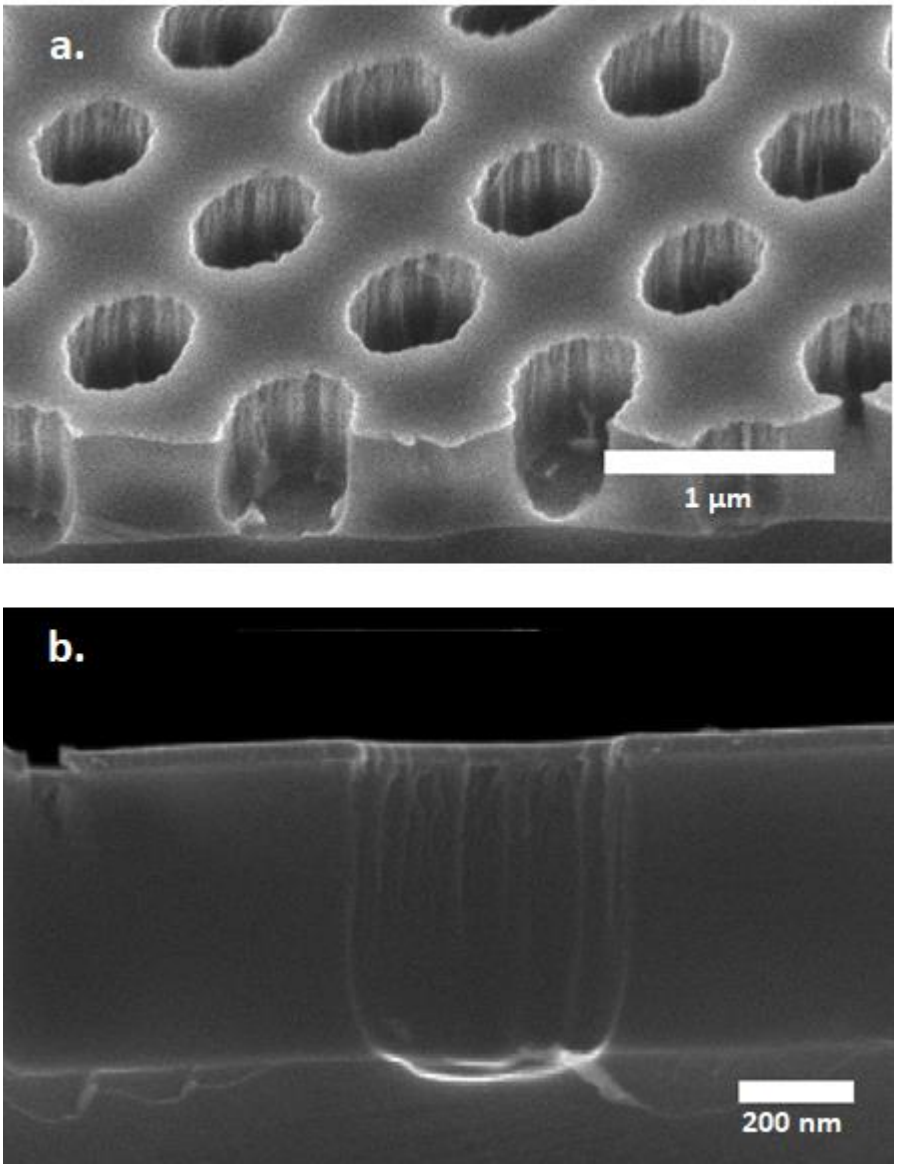

Figure 2.1. (a) SEM micrograph of RIE results for a 1 µm thick SiN_x film imaged from at 45° angle to the surface (chip was cleaved prior to imaging). (b) Cross-sectional SEM micrograph of a pore from the etch shown in (a). Note that both images are taken of the Si-supported portion of the SiN_x film since the freestanding portion did not remain intact after cleaving.

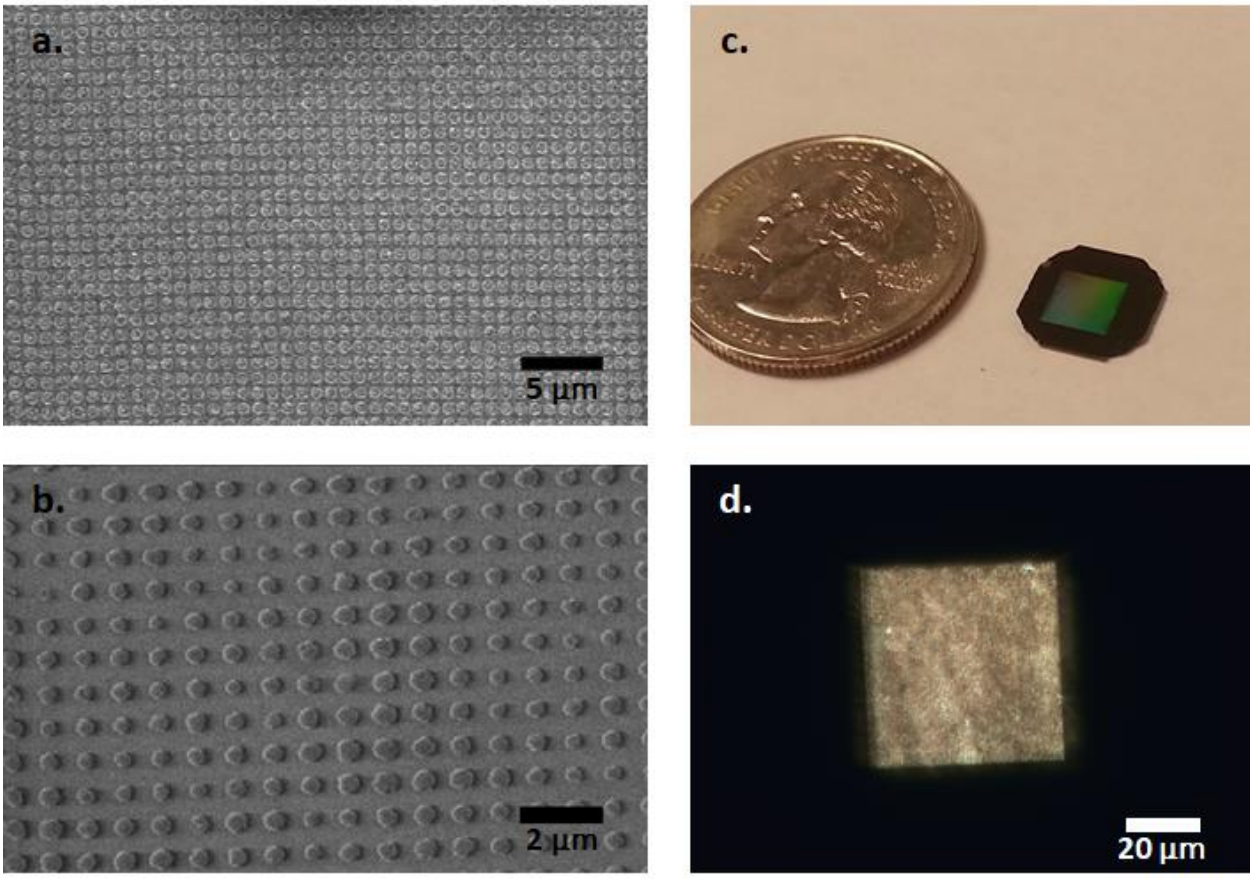

Figure 2.2. SEM micrographs of the (a) top and (b) bottom surfaces of a completed BPE array. (c) SEM micrograph of a completed BPE array chip with a quarter for scale. (d) Transmission microscope image of the electroactive portion of the array surface.

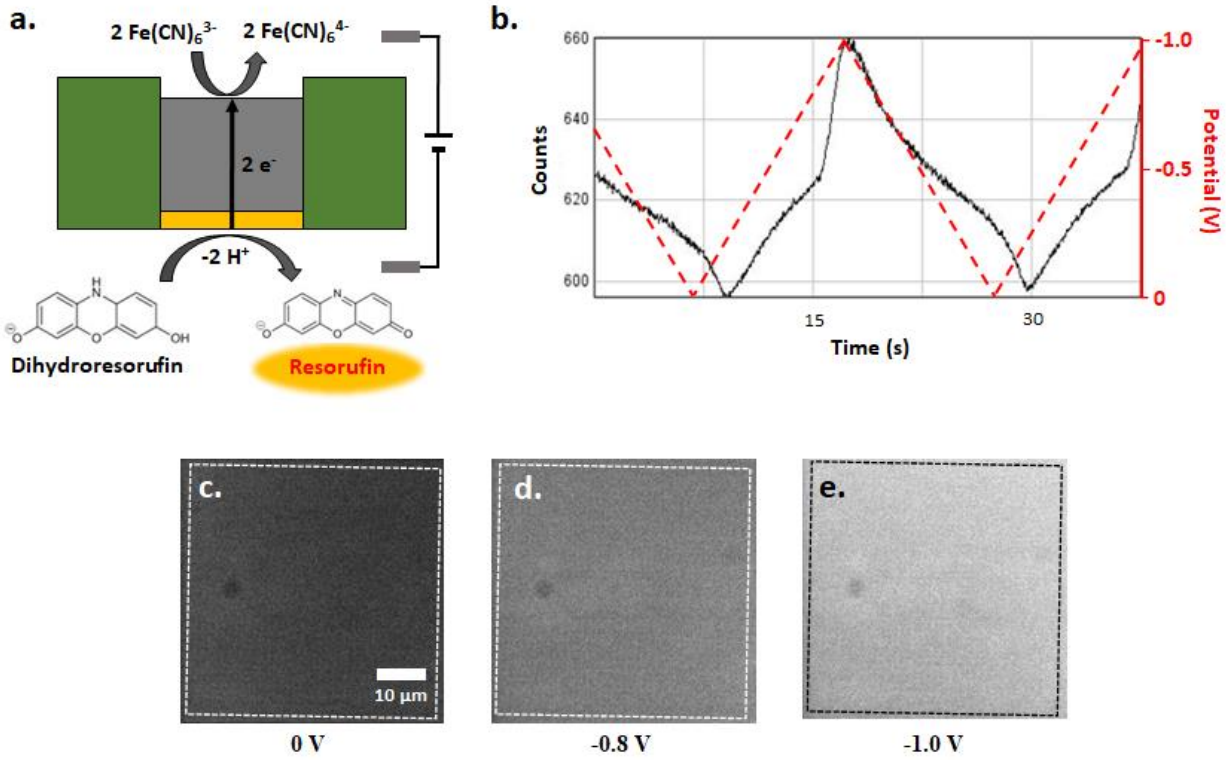

Figure 2.3. (a) Diagram of FEEM imaging in which $Fe(CN)_6^{3-}$ reduction is coupled to fluorogenic dihydroresorufin oxidation. (b) Fluorescence intensity trace for array surface overlaid with the applied driving potential waveform. (c) Representative fluorescence images of the array surface monitored in panel (b) corresponding to various driving potentials. The dotted line in each image denotes the outline of the array surface.

Chapter 3

ELECTROCHEMILUMINESCENCE (ECL)-BASED ELECTROCHEMICAL IMAGING USING A MASSIVE ARRAY OF BIPOLAR ULTRAMICROELECTRODES

3.1 INTRODUCTION

Electroanalytical methods for imaging redox molecules with high spatial and temporal resolution have sparked significant interest in fields ranging from bioanalysis[1,2] to electrocatalysis.[3-5] In general, these techniques may be classified into two broad groups: scanning probe methods and dual optical-electrochemical imaging. Notable techniques in the former category include scanning electrochemical microscopy (SECM),[6] scanning electrochemical cell microscopy (SECCM),[7] and scanning ion conductance microscopy (SICM).[8] Each of these methods is performed by rapidly scanning a miniscule probe such as an ultramicroelectrode (UME) or quartz nanopipette over a surface of interest while collecting the tip current to map the electrochemical activity and topography of the substrate. While they all can achieve nanoscale spatial resolution,[9] the time required to raster the probe across the sample surface limits their utility in highly dynamic electrochemical systems. In contrast, dual optical-electrochemical methods provide a means of monitoring spatially segregated redox processes at an enhanced temporal resolution. They may also enable the detection of single molecules due to the high sensitivity of optical-based detection.[10,11]

Electrochemiluminescence (ECL)[12] and fluorogenic reactions[13,14] have been employed as probes for direct mapping of electrocatalytic activity; luminol-based ECL systems are also commonly used in hydrogen peroxide sensors.[15,16] However, the processes which may be studied by such direct imaging methods are limited to a few reactions which produce a luminescent

product. Changes in the fluorescence of pH-sensitive reporter species have also been utilized to image reactions which alter solution pH,[17-19] but the range of applications for this approach is similarly constrained. The Chen group recently used a fluorogenic reporter reaction to monitor a non-fluorogenic reaction via a competition mechanism.[20] Despite its elegance, this approach may be confined to the study of inner sphere redox species since it relies upon competition between two parallel adsorption processes.

The use of an array of bipolar electrodes (BPEs) to couple an analyte reaction to a complementary reporter reaction provides a more flexible imaging approach. In an open BPE scheme, a driving voltage is used to induce a potential gradient along the surface of a floating electrode. Once the potential difference exceeds the difference in formal potential of two redox species in the same solution, two half reactions will be coupled to one another on the BPE. If one of these generates an optical signal, such as ECL or fluorescence, one can use the optical response to monitor the reaction on the opposite pole.[21-25] However, due to the competing ionic current pathway in an open BPE system, large electrodes or high driving potentials are often needed to achieve the desired coupling.

Closed BPEs provide an interesting alternative since the parallel ionic current pathway is not present.[26,27] The majority of the applied potential drops across the closed BPE itself, thereby eliminating the need for large electrodes and high driving voltages. An array of closed BPEs can then be used as an electrochemical imaging platform to monitor dynamic changes in redox concentrations. Indeed, our group has previously introduced the fluorescence-enabled electrochemical microscopy (FEEM) in which a fluorogenic reaction was used to image redox processes on an array of carbon fibers.[28-30] While the carbon fibers arrays are easy to prepare, they exhibited poor uniformity and crosstalk due to aggregation of the constituent fibers.[28] The

fluorescent reporting species was also prone to fast diffusion, thereby further inhibiting the spatial resolution.

Here we present the use of a very large array of microfabricated closed BPEs for imaging highly dynamic redox processes. This flexible BPE array is 1×1 cm^2 in size and is comprised of 146,522 8μm-diameter carbon UMEs arranged in an ordered hexagonal lattice pattern with a 28 μm electrode spacing. Our BPE array can be prepared with conventional microfabrication tools and has an electrode count over twice that of any individually addressable electrode array reported in the literature.[31-35] Using ECL as the reporter process (see **Scheme 3.1**), the electrochemical signal can be optically recorded from all of the electrodes with a temporal resolution better than 30 ms. The use of ECL also improves the spatial resolution compared to a fluorescence-based scheme due to the absence of unhindered diffusion of the reporter species. To our knowledge, this is the first instance of ECL-based electrochemical imaging on very large, uniform BPE arrays; other array-based studies have reported a similar detection strategy, but either do not focus on spatially resolving the source of the ECL signal[36-39] or are limited to a spatial resolution of ~0.5 mm.[40]

3.2 Experimental Section

3.2.1 *Array Fabrication*

A Si wafer (Silicon Valley Microelectronics) was cleaned by O_2 plasma (Glow Research) for 5 min (175 W, 1 torr) and spin-coated with SU-8 2050 (MicroChem) photoresist (PR) to yield a 40 μm thick film. The PR film was baked at 65 °C for 3 min and 95 °C for 6 min followed by selective exposure on a mask aligner (ABM-USA). The exposed wafer was then subjected to stress reduction (1 min at 65 °C) and post-exposure baking (6 min at 95 °C). The PR film was then

developed in SU-8 developer (MicroChem) for 5 min and rinsed with developer, isopropanol, and DI water before being spun dry.

The SU-8-patterned wafer was diced into ~2×2 cm^2 chips and hard baked in a tube furnace (Thermo Scientific) for 40 min at 300 °C under N_2 flow, after which the temperature was increased to 900 °C for 1 h. The furnace was left closed until it had returned to room temperature. Following pyrolysis, 20 µm of Parylene C was deposited over the patterned chips with a Labcoter 2 system (Specialty Coating Systems) at 175 °C and 690 °C for the vaporizer and pyrolysis furnaces, respectively, and a chamber pressure of 35 mtorr. The Parylene C films were annealed for 2 h at 400 °C under N_2. A PlasmaLab 100 ICP etcher (Oxford Instruments) was used to expose the pyrolyzed carbon structures through the overlying Parylene. The processed Parylene films were released from Si by overnight immersion in 1 M KOH at 100 °C.

3.2.2 *Array Preparation for Imaging*

A plastic well was epoxied to the array surface for containment of the top analyte solution. The well was prepared by cutting a 15 mm section from the wide end of a 1 mL pipette tip and attaching it to the array. The ECL solution below the array was contained on the microscope stage using a home-built device fabricated from three 1.0 mm thick glass slides (VWR). One slide was used as the base and two were positioned laterally about 1 cm apart, creating a 1 mm deep channel for ECL solution containment. Epoxy was used to prevent solution leakage.

3.2.3 *Bipolar Imaging*

Potential was driven across the array using a 3-electrode CV-27 potentiostat (BAS) with three Ag/AgCl electrodes. Two electrodes were placed in the bottom ECL solution, and one was placed in the top solution. Wires were freshly chlorided prior to each experiment using a 1:1 solution of

70% HNO_3 and 3 M KCl. The ECL-CV and redox puffing experiments were recorded on an Andor iXon 897E EMCCD camera cooled to -80 ^oC with 30 ms exposure, 300 EM Gain, 5.1x pre-amplifier gain, 0.3 µs vertical pixel shift speed, and 10 MHz readout rate. Videos contained 1500 frames with 512×512 pixels. An Olympus IX70 microscope equipped with a 4x (0.1 NA Olympus Plan N) objective was used to image the array. Each pixel measured 3.92 µm, yielding a 4.0×10^6 μm^2 field of view and allowing 6005 full electrodes in each frame.

The generator-collector and depletion zone imaging experiments were recorded using an Andor Luca S 658M EMCCD cooled to -20 ^oC with 30 ms exposure; 0.6 µs vertical pixel shift speed, and 13.5 MHz readout rate. Videos contained 1500 frames with 658×496 pixels. The same IX70 microscope and 4x objective were used. Each pixel measured 1.03 µm, yielding a 3.5×10^5 μm^2 field of view and allowing 507 full electrodes to be viewed in each frame. All videos were analyzed using ImageJ.

An optically-correlated bipolar CV was driven between 100 mM $Fe(CN)_6^{3-}$ 100 mM KCl solution on top of the array, and 25 mM $Ru(bpy)_3^{2+}$ 20 mM DBAE 100 mM phosphate buffer (PB) pH 7.4 below the array. Potential was scanned from 0 to +2.8 V to 0 V vs. Ag/AgCl at 200 mV/s using a CV-27 potentiostat. The current-potential (*i*-*V*) trace was recorded using a Labview 2013 program, while the ECL intensity-potential (I_{ECL}-*V*) trace was simultaneously monitored using conditions described above.

In the generator-collector experiment, a 12.7 µm diameter Au UME was positioned using a Sutter MP-225 micromanipulator in 50 mM $Fe(CN)_6^{4-}$ 1 M KCl solution ~100 µm above the array surface. A 0.8 V potential was applied on the Au UME vs. Ag/AgCl to generate $Fe(CN)_6^{3-}$ at the electrode surface. The $Fe(CN)_6^{3-}$ then diffused to the array surface, which was biased at +2.0 V, and underwent electrochemical reduction by coupling to anodic ECL across each closed-bipolar

electrode. The solution used in the ECL experiment was 5 mM $Ru(bpy)_3^{2+}$ 20 mM DBAE 100 mM PB pH 7.4.

To image the depletion zone, a similar procedure was followed as for the above generator-collector experiment. Important differences include the use of a 50 µm Au UME as the generator electrode and maintaining a stationary electrode position throughout the experiment. The Au electrodes for both experiments were fabricated by sealing a piece of Au wire in a glass capillary.[41] Electrodes were characterized using cyclic voltammetry in 1 mM FcMeOH 100 mM KCl solution.

For the redox concentration mapping experiment, a pulled glass micropipette[42] with a 10 µm orifice was immersed in 100 mM KCl solution and was used to inject 100 mM $Fe(CN)_6^{3-}$ 100 mM KCl solution orthogonally onto the array surface. An Eppendorf Femtojet was used to apply constant injection pressures for a controlled period ranging from 1 to 10 s with pressures ranging from 0.5 to 2 PSI. The micropipette was placed ~100 µm above the array surface and remained at a constant distance for the duration of the experiment. Following each stimulation, $Fe(CN)_6^{3-}$ was reduced across the array surface, which was coupled to an anodic ECL process to generate an optical output. A 2.8 V potential was applied across the array to drive the bipolar reaction. The solution used in the ECL experiment consisted of 25 mM $Ru(bpy)_3^{2+}$ 20 mM DBAE 100 mM PB at pH 7.4.

3.3 Results and Discussion

3.3.1 *Fabrication of Bipolar UME Arrays*

A bottom-up process was developed to fabricate the BPE arrays. As summarized in **Scheme 3.2**, our method involves making a large, uniform array of carbon UMEs on a Si substrate, insulating it in a thin Parylene film, and exfoliating the array from the substrate. Several key factors need to be considered. First, since the array resolution is limited by the electrode size and spacing, closely

spaced UMEs are desirable to attain maximum density. The insulating film must also be robust and continuous to prevent passage of ionic current. Lastly, the device must be as thin as possible to minimize electrical discontinuities which could arise from high aspect ratio electrode geometries.

We adapted a procedure from Wang, *et al.*[43] to generate large arrays of carbon micropillars. A high-temperature pyrolysis process turns an array of SU-8 micropillars into an array of conductive carbon posts. Note from **Figures 3.1a** and **3.1b**, however, that the height and diameter of each micropillar is reduced by a factor of two during pyrolysis. This volume loss plays a role in determining the final device thickness and must be considered by selecting a SU-8 thickness twice that of the desired micropillar height.

The carbon array was insulated by Parylene C, a flexible coating widely used in the electronics industry[44-46] due to its excellent electrical properties and chemical resistance. A continuous film may be formed about the carbon micropillars once sufficient growth has occurred on their sidewalls (**Figure 3.1c**). With this in mind, the SU-8 precursor structures were hexagonally arranged to minimize both the edge-to-edge electrode spacing and, by extension, the thickness of Parylene C required to form a continuous film. The use of a hexagonal lattice arrangement also resulted in a 15% increase in electrode density compared to a square lattice.

We used thermal annealing to prevent stress fractures in the free-standing membranes after exfoliation. This annealing process increases the tensile strength and elongation-at-break of the Parylene film. Melting and reflowing of the Parylene also renders the substance amorphous and serves to seal any unfilled voids which would result in the passage of ionic current through the insulating layer during device operation. We used O_2 plasma etching to expose the upper carbon surfaces (**Figure 3.1d**). A hot KOH solution was used to dissolve the Si and free the devices. No

degradation or etching of the Parylene or electrodes was observed. Note the uniformity of the electrodes and absence of defects shown in **Figures 3.1e** and **3.1f**. A finished device is pictured in **Figure 3.1g**.

3.3.2 *Electrochemical Imaging*

Electrochemical imaging experiments were performed to characterize the array's response dynamics, as well as to explore a previously unreported imaging application. Four unique experiments are described along with their independent analyses. We quantify the homogeneity of the ECL response across each array electrode, provide proof for the absence of cross talk, demonstrate the capacity to image variable redox concentrations, and explore the generation of depletion zones in confined spaces using a generator-collector apparatus. Overall, we aim to highlight the excellent performance and broad applicability of our newly fabricated closed-bipolar array for electrochemical imaging.

We first investigated the homogeneity of the ECL intensity (I_{ECL}) on the array by performing a correlated ECL-cyclic voltammogram (ECL-CV). Here, bulk 100 mM $Fe(CN)_6^{3-}$ is placed on top of the array and coupled to anodic ECL solution below the array by reversibly scanning the potential from 0 to 2.8 V, as shown in **Figure 3.2a**. Both electrochemical (i-V) and optical (I_{ECL}-V) voltammograms were plotted in **Figure 3.2b**. The two signals match well in their overall shape, where both onset potentials begin at ~1.1 V and approach a maximum value at ~2.1 V. Interestingly, the I_{ECL} begins to decrease despite increasing potential at 2.3 V, possibly due to interference from other redox reactions such as water oxidation.

The optical response of a ~300-electrode subset of the array during the potential scan is displayed in **Figure 3.2c** to show single electrode responses. We observe that the I_{ECL} at each electrode is indeed uniform relative to its adjacent electrodes. We aimed to further quantify this

homogeneity by plotting each individual electrode's I_{ECL} response at correlated potentials, as shown in **Figure B1a**. The plotted results demonstrate that the ECL intensity changes uniformly with scanned potential across the array subset. In **Figure B1b** we expand the analysis of individual electrode I_{ECL}-values across all 6000 non-edge electrodes within the recorded field of view. Much variability is observed between the I_{ECL} for electrodes within this large region as evidenced by the wide distribution at each potential. However, examination of a single frame during the scan in **Figure B1d** allows us to conclude that the variation is present only in the upper left and lower left corners of the array, likely due to those regions extending slightly below the focal plane of the microscope objective. Since the 300-electrode subset is entirely within the same focal plane, it will be treated as the metric for comparison. We therefore conclude that the I_{ECL} response is indeed identical across equivalent electrodes.

We next aimed to determine if crosstalk (electron transfer between neighboring electrodes) was occurring since it has been reported for previous closed-bipolar array fabrication schemes.[28] Elimination of crosstalk is important to ensure single-electrode spatial resolution. We investigated this behavior by using a generator-collector setup as shown in **Figure 3.3a**, similar to the setup used in our previous work.[30] Here, a 12.7 µm Au UME was positioned ~100 µm above the array surface in a 50 mM $Fe(CN)_6^{4-}$ solution. A +0.8 V potential was applied to the Au UME, producing $Fe(CN)_6^{3-}$ which diffused toward the array. The diffusion layer was optically detected across the biased (+2V) bipolar array by coupling to anodic ECL.

Upon activation of the generator electrode, a 3-electrode cluster in the array was immediately illuminated by ECL. The generator electrode was then moved laterally across the array with a micro-positioner and the corresponding array illumination precisely followed its movement with no perceptible lag. **Figure 3.3b** displays four illuminated positions of the

electrode. This result suggests that the relatively constant size of the diffusion layer was uniformly detected. If crosstalk were present, we would expect to observe overlap of the signal from neighboring electrodes. While it is possible for toppling of the electrodes to occur prior to Parylene deposition, these occurrences are easily observable and may be screened out during the fabrication process. Nonetheless, we verified that the arrays were absent from crosstalk by scanning the generator electrode across thousands of other array electrodes in subsequent experiments.

We next aimed to explore our capacity to map variable redox concentrations across a wide area. Here, we positioned a micropipette filled with 100 mM $Fe(CN)_6^{3-}$ 100 µm away from the array, as shown in **Figure 3.4a**. A pressure-injection module was used to dispense the $Fe(CN)_6^{3-}$ at pressures between 0.5 and 2 PSI and durations from 1 to 10 s. Reduction of $Fe(CN)_6^{3-}$ was coupled to anodic ECL across the bipolar array electrodes which were driven by a +2.8 V bias voltage.

In **Figure 3.4b** we show an example $Fe(CN)_6^{3-}$ injection time lapse using 2 PSI for 5 s. Variations in ECL intensity and illuminated regions are observed depending on the time point during the injection. The illumination zone begins as a ~150 µm diameter cluster at 0.09 s and grows in area until the pressure is turned off at 5 s, resulting in a zone diameter of ~1 mm. After the pressure is turned off, the intensity gradually fades due to decreased $Fe(CN)_6^{3-}$ convection paired with dilution by the bulk KCl solution. Under constant potential, the I_{ECL} fluctuations must be due to local changes in $Fe(CN)_6^{3-}$ concentration. In **Figure 3.4b** we observe higher $Fe(CN)_6^{3-}$ concentrations near the center of the plume during the injection period which implies a faster convective flow velocity. This is in good agreement with simulations of convective flow profiles from a micropipette by Unwin and co-workers.[47-49]

Figure 3.4c compares the maximum intensities from 12 puffing experiments using the annotated injection pressure and duration conditions. We observe that a high pressure and short duration (2 PSI, 0.5 sec) more effectively delivers $Fe(CN)_6^{3-}$ to the array compared to a low pressure over a long duration (0.5 PSI, 10 sec). This effect can be attributed to increased convective mass transfer at higher pressures, thereby displacing more KCl solution from the array surface.[49] Overall, these results demonstrate that we can map changing redox concentrations during dynamic time-resolved redox processes.

We lastly examined the time-resolved formation of a redox depletion zone from a generator-collector setup in a confined space. The experiment used a setup similar to the one shown in **Figure 3.3**. A major difference was the use of a larger 50 µm Au UME with a 2 mm glass sheath held at a fixed position ~100 µm above the array. An oxidizing potential of +0.8 V was applied to the Au UME to generate $Fe(CN)_6^{3-}$ via $Fe(CN)_6^{4-}$ oxidation which then diffused to the array surface. The diffusion layer was optically probed on the bipolar array by coupling $Fe(CN)_6^{3-}$ reduction to the anodic ECL.

Interestingly, we observed a starkly different behavior than in **Figure 3.3**. A larger illumination zone was immediately detected which was indicative of the larger diffusion layer about the 50 µm Au UME. This illuminated area grew to ~400 µm over the first 2 s, with greater ECL intensity being observed near the center than at the edges. However, beginning at 3 s, the center of the illumination began to steadily decrease in intensity until a dark depletion zone was formed directly beneath the Au UME position. Over time, both the illumination and depletion regions pushed further outward away from the original Au UME location.

We believe the formation of the depletion zone is due to a multi-step interaction between the mass transfer at the Au UME and array electrodes, as illustrated in **Figure 3.5a**. An initial

oxidation of 50 mM $Fe(CN)_6^{4-}$ near the Au UME generates $Fe(CN)_6^{3-}$ which diffuses radially outward. Hindered diffusion due to confinement in the ~100 μm micro-gap steadily decreases the available $Fe(CN)_6^{4-}$ at the UME surface. While $Fe(CN)_6^{4-}$ may continue to diffuse to the UME from the sides, the center region directly beneath the UME can no longer receive $Fe(CN)_6^{4-}$. Therefore, less and less $Fe(CN)_6^{3-}$ could be generated from this region leading to the formation of the observed depletion zone, which is shown in panels 2-6 in **Figure 3.5b**.

In **Figure 3.5c** we support this mechanism by creating a heatmap that illustrates how the ECL intensity of the selected area changes over the recording duration. Importantly, the heatmap indicates that both the diffusion layer and depletion zones grow radially outward at the same rate as evidenced by the steady thickness of the I_{ECL} ring. This observation suggests that both regions are controlled by the same diffusion-limited mass transfer process and are likely emanating from the same UME point source. Consequently, we expect the size of the depletion zone to be directly influenced by the diameter of the generating UME. Overall, these results demonstrate the excellent electrochemical imaging capacity of our bipolar array for dynamic time-resolved processes.

3.4 CONCLUSIONS

In summary, we have successfully fabricated uniform, massive arrays of carbon bipolar UMEs using a reproducible microfabrication procedure. This process uses carbon pyrolysis and Parylene deposition to yield an ultrathin freestanding Parylene film containing >140,000 highly uniform bipolar carbon UMEs. These arrays have been used to study several dynamic processes, including tracing the motion of an Au UME, imaging the pressure-driven flow of redox species from a micropipette, and characterizing the generation, diffusion, and depletion of $Fe(CN)_6^{3-}$ on an Au UME. The spatial resolution was found to be limited by the size of the bipolar UMEs and their spacing, which can be further improved by reducing the electrode dimensions and the

interelectrode spacing. The temporal resolution, on the other hand, is limited only by the data transfer rate of the camera. Our results have further confirmed that microfabricated UME arrays are uniquely suited to imaging fast and dynamic redox processes. Further work focusing on the development of this bipolar imaging system to create a massively parallelized screening platform for high-throughput screening of metal electrocatalysts is discussed in the following chapter.

Note: This chapter is adapted with permission from Anderson, T. J.; Defnet, P. A.; Zhang, B. "Electrochemiluminescence (ECL)-Based Electrochemical Imaging Using a Massive Array of Bipolar Ultramicroelectrodes." Anal. Chem. **2020**, *92*, 6748–6755.

3.5 REFERENCES

(1) Lin, T.-E.; Rapino, S.; Girault, H. H.; Lesch, A. Electrochemical Imaging of Cells and Tissues. *Chem. Sci.* **2018**, *9*, 4546–4554.

(2) Conzuelo, F.; Schulte, A.; Schuhmann, W. Biological Imaging with Scanning Electrochemical Microscopy. *Proc. R. Soc. A* **2018**, *474*, 20180409.

(3) Takahashi, Y.; Kobayashi, Y.; Wang, Z.; Ito, Y.; Ota, M.; Ida, H.; Kumatani, A.; Miyazawa, K.; Fujita, T.; Shiku, H.; Korchev, Y. E.; Miyata, Y.; Fukuma, T.; Chen, M.; Matsue, T. High-Resolution Electrochemical Mapping of the Hydrogen Evolution Reaction on Transition-Metal Dichalcogenide Nanosheets. *Angew. Chem. Int. Ed.* **2020,** *59*, 3601–3608.

(4) Zhu, M.-J.; Pan, J.-B.; Wu, Z.-Q.; Gao, X.-Y.; Zhao, W.; Xia, X.-H.; Xu, J.-J.; Chen, H.-Y. Electrogenerated Chemiluminescence Imaging of Electrocatalysis at a Single Au-Pt Janus Nanoparticle. *Angew. Chem. Int. Ed.* **2018**, *57*, 4010–4014.

(5) Zou, N.; Chen, G.; Mao, X.; Shen, H.; Choudhary, E.; Zhou, X.; Chen, P. Imaging Catalytic Hotspots on Single Plasmonic Nanostructures via Correlated Super-Resolution and Electron Microscopy. *ACS Nano* **2018**, *12*, 5570–5579.

(6) Amemiya, S.; Bard, A. J.; Fan, F.-R. F.; Mirkin, M. V.; Unwin, P. R. Scanning Electrochemical Microscopy. *Ann. Rev. Anal. Chem.* **2008**, *1*, 95–131.

(7) Ebejer, N.; Schnippering, M.; Colburn, A. W.; Edwards, M. A.; Unwin, P. R. Localized High Resolution Electrochemistry and Multifunctional Imaging: Scanning Electrochemical Cell Microscopy. *Anal. Chem.* **2010**, *82*, 9141–9145.

(8) Chen, C.-C.; Zhou, Y.; Baker, L. A. Scanning Ion Conductance Microscopy. *Ann. Rev. Anal. Chem.* **2012**, *5*, 207–228.

(9) Takahashi, Y.; Kumatani, A.; Shiku, H.; Matsue, T. Scanning Probe Microscopy for Nanoscale Electrochemical Imaging. *Anal. Chem.* **2017**, *89*, 342–357.

(10) Hao, R.; Peng, Z.; Zhang, B. Single-Molecule Fluorescence Microscopy for Probing the Electrochemical Interface. *ACS Omega* **2020**, *5*, 89–97.

(11) Fan, Y.; Anderson, T. J.; Zhang, B. Single-Molecule Electrochemistry: From Redox Cycling to Single Redox Events. *Curr. Opin. in Electrochem.* **2018**, *7*, 81–86.

(12) Chen, Y.; Zhao, D.; Fu, J.; Gou, X.; Jiang, D.; Dong, H.; Zhu, J.-J. In Situ Imaging Facet-Induced Spatial Heterogeneity of Electrocatalytic Reaction Activity at the Subparticle Level via Electrochemiluminescence Microscopy. *Anal. Chem.* **2019**, *91*, 6829-6835.

(13) Sambur, J. B.; Chen, T.-Y.; Choudhary, E.; Chen, G.; Nissen, E. J.; Thomas, E. M.; Zou, N.; Chen, P. Sub-Particle Reaction and Photocurrent Mapping to Optimize Catalyst-Modified Photoanodes. *Nature* **2016**, *530*, 77–80.

(14) Sambur, J. B.; Chen, P. Distinguishing direct and indirect photoelectrocatalytic oxidation mechanisms using quantitative single-molecule reaction imaging and photocurrent measurements. *J. Phys. Chem. C* **2016**, *120*, 20668–20676.

(15) Zhang, J.; Zhou, J.; Tian, C.; Yang, S.; Jiang, D.; Zhang, X.-X.; Chen, H.-Y. Localized Electrochemiluminescence from Nanoneedle Electrodes for Very-High-Density Electrochemical Sensing. *Anal. Chem.* **2017**, *89*, 11399–11404.

(16) Cui, C.; Jin, R.; Jiang, D.; Zhang, J.; Zhu, J.-J. Electrogenerated Chemiluminescence in Submicrometer Wells for Very High-Density Biosensing. *Anal. Chem.* **2020**, *92*, 578–582.

(17) Yang, M.; Batchelor-McAuley, C.; Kätelhön, E.; Compton, R. G. Reaction Layer Imaging Using Fluorescence Electrochemical Microscopy. *Anal. Chem.* **2017**, *89*, 6870–6877.

(18) Pruchyathamkorn, J.; Yang, M.; Amin, H. M. A.; Batchelor-McAuley, C.; Compton, R. G. Imaging Electrode Heterogeneity Using Chemically Confined Fluorescence Electrochemical Microscopy. *J. Phys. Chem. Lett.* **2017**, *8*, 6124–6127.

(19) Fuladpanjeh-Hojaghan, B.; Elsutohy, M. M.; Kabanov, V.; Heyne, B.; Trifkovic, M.; Roberts, E. P. L. In-Operando Mapping of pH Distribution in Electrochemical Processes. *Angew. Chem.* **2019**, *131*, 16971–16975.

(20) Mao, X.; Liu, C.; Hesari, M.; Zou, N.; Chen, P. Super-Resolution Imaging of Non-Fluorescent Reactions via Competition. *Nat. Chem.* **2019**, *11*, 687–694.

(21) Arora, A.; Eijkel, J. C. T.; Morf, W. E.; Manz, A. A Wireless Electrochemiluminescence Detector Applied to Direct and Indirect Detection for Electrophoresis on a Microfabricated Glass Device. *Anal. Chem.* **2001**, *73*, 3282–3288.

(22) Zhan, W.; Alvarez, J.; Crooks, R. M. Electrochemical Sensing in Microfluidic Systems Using Electrogenerated Chemiluminescence as a Photonic Reporter of Redox Reactions. *J. Am. Chem. Soc.* **2002**, *124*, 13265–13270.

(23) Mavré, F.; Chow, K.-F.; Sheridan, E.; Chang, B.-Y.; Crooks, J. A.; Crooks, R. M. A Theoretical and Experimental Framework for Understanding Electrogenerated Chemiluminescence (ECL) Emission at Bipolar Electrodes. *Anal. Chem.* **2009**, *81*, 6218–6225.

(24) Chow, K.-F.; Mavré, F.; Crooks, R. M. Wireless Electrochemical DNA Microarray Sensor. *J. Am. Chem. Soc.* **2008**, *130*, 7544–7545.

(25) Chow, K.-F.; Mavré, F.; Crooks, J. A.; Chang, B.-Y.; Crooks, R. M. A Large-Scale, Wireless Electrochemical Bipolar Electrode Microarray. *J. Am. Chem. Soc.* **2009**, *131*, 8364–8365.

(26) Cox, J. T.; Guerrette, J. P.; Zhang, B. Steady-State Voltammetry of a Microelectrode in a Closed Bipolar Cell. *Anal. Chem.* **2012**, *84*, 8797-8804.

(27) Guerrette, J. P.; Oja, S. M.; Zhang, B. Coupled Electrochemical Reactions at Bipolar Microelectrodes and Nanoelectrodes. *Anal. Chem.* **2012**, *84*, 1609-1616.

(28) Guerrette, J. P.; Percival, S. J.; Zhang, B. Fluorescence Coupling for Direct Imaging of Electrocatalytic Heterogeneity. *J. Am. Chem. Soc.* **2013**, *135*, 855–861.

(29) Oja, S. M.; Guerrette, J. P.; David, M. R.; Zhang, B. Fluorescence-Enabled Electrochemical Microscopy with Dihydroresorufin as a Fluorogenic Indicator. *Anal. Chem.* **2014**, *86*, 6040–6048.

(30) Oja, S. M.; Zhang, B. Imaging Transient Formation of Diffusion Layers with Fluorescence-Enabled Electrochemical Microscopy. *Anal. Chem.* **2014**, *86*, 12299–12307.

(31) Wydallis, J. B.; Feeny, R. M.; Wilson, W.; Kern, T.; Chen, T.; Tobet, S.; Reynolds, M. M.; Henry, C. S. Spatiotemporal Norepinephrine Mapping Using a High-Density CMOS Microelectrode Array. *Lab Chip* **2015**, *15*, 4075–4082.

(32) Dragas, J.; Viswam, V.; Shadmani, A.; Chen, Y.; Bounik, R.; Stettler, A.; Radivojevic, M.; Geissler, S.; Obien, M. E. J.; Muller, J.; Hierlemann, A. *In Vitro* Multi-Functional Microelectrode Array Featuring 59 760 Electrodes, 2048 Electrophysiology Channels, Stimulation, Impedance Measurement, and Neurotransmitter Detection Channels. *IEEE J. Solid-State Circuits* **2017**, *52*, 1576–1590.

(33) Tedjo, W.; Nejad, J. E.; Feeny, R.; Yang, L.; Henry, C. S.; Tobet, S.; Chen, T. Electrochemical Biosensor System Using a CMOS Microelectrode Array Provides High Spatially and Temporally Resolved Images. *Biosens. and Bioelect.* **2018**, *114*, 78–88.

(34) Viswam, V.; Bounik, R.; Shadmani, A.; Dragas, J.; Urwyler, C.; Boos, J. A.; Obien, M. E. J.; Muller, J.; Chen, Y.; Hierlemann, A. Impedance Spectroscopy and Electrophysiological Imaging of Cells with a High-Density CMOS Microelectrode Array System. *IEEE Trans. Biomed. Circuits Syst.* **2018**, *12*, 1356–1368.

(35) Tedjo, W.; Chen, T. An Integrated Biosensor System with a High-Density Microelectrode Array for Real-Time Electrochemical Imaging. *IEEE Trans. Biomed. Circuits Syst.* **2019**, 1–1.

(36) Lin, X.; Zheng, L.; Gao, G.; Chi, Y.; Chen, G. Electrochemiluminescence Imaging-Based High-Throughput Screening Platform for Electrocatalysts Used in Fuel Cells. *Anal. Chem.* **2012**, *84*, 7700–7707.

(37) Wu, M.-S.; Liu, Z.; Shi, H.-W.; Chen, H.-Y.; Xu, J.-J. Visual Electrochemiluminescence Detection of Cancer Biomarkers on a Closed Bipolar Electrode Array Chip. *Anal. Chem.* **2015**, *87*, 530–537.

(38) Zhai, Q.; Zhang, X.; Han, Y.; Zhai, J.; Li, J.; Wang, E. A Nanoscale Multichannel Closed Bipolar Electrode Array for Electrochemiluminescence Sensing Platform. *Anal. Chem.* **2016**, *88*, 945–951.

(39) Ino, K.; Yaegaki, R.; Hiramoto, K.; Nashimoto, Y.; Shiku, H. Closed Bipolar Electrode Array for On-Chip Analysis of Cellular Respiration by Cell Aggregates. *ACS Sens.* **2020**, 5, 740-745.

(40) Iwama, T.; Inoue, K. Y.; Abe, H.; Matsue, T. Chemical Imaging Using a Closed Bipolar Electrode Array. *Chem. Lett.* **2018**, *47*, 843–845.

(41) Defnet, P. A.; Zhang, B. Detection of Transient Nanoparticle Collision Events Using Electrochemiluminescence on a Closed Bipolar Microelectrode. *ChemElectroChem* **2020**, *7*, 252–259.

(42) Defnet, P. A.; Han, C.; Zhang, B. Temporally-Resolved Ultrafast Hydrogen Adsorption and Evolution on Single Platinum Nanoparticles. *Anal. Chem.* **2019**, *91*, 4023–4030.

(43) Wang, C.; Jia, G.; Taherabadi, L. H.; Madou, M. J. A Novel Method for the Fabrication of High-Aspect Ratio C-MEMS Structures. *J. Microelectromech. Sys.* **2005**, *14*, 348–358.

(44) Li, W.; Rodger, D. C.; Meng, E.; Weiland, J. D.; Humayun, M. S.; Tai, Y.-C. Wafer-Level Parylene Packaging with Integrated RF Electronics for Wireless Retinal Prostheses. *J. Microelectromech. Sys.* **2010**, *19*, 735–742.

(45) Jung, Y. H.; Qiu, Y.; Lee, S.; Shih, T.-Y.; Xu, Y.; Xu, R.; Lee, J.; Schendel, A. A.; Lin, W.; Williams, J. C.; Behdad, N.; Ma, Z. A Compact Parylene-Coated WLAN Flexible Antenna for Implantable Electronics. *IEEE Antennas and Wireless Prop. Lett.* **2016**, *15*, 1382–1385.

(46) Trantidou, T.; Tariq, M.; Terracciano, C.; Toumazou, C.; Prodromakis, T. The Effects of Annealing on Mechanical, Chemical, and Physical Properties and Structural Stability of Parylene C. *Sensors* **2014**, *14*, 11629–11639.

(47) Macpherson, J. V; Simjee, N.; Unwin, P. R. Hydrodynamic Ultramicroelectrodes: Kinetic and Analytical Applications. *Electrochim. Acta* **2001**, *47*, 29–45.

(48) Bitziou, E.; Rudd, N. C.; Edwards, M. A.; Unwin, P. R. Visualization and Modeling of the Hydrodynamics of an Impinging Microjet. *Anal. Chem.* **2006**, *78*, 1435–1443.

(49) Macpherson, J. V; Beeston, M. A.; Unwin, P. R. Imaging Local Mass-Transfer Rates within an Impinging Jet and Studies of Fast Heterogeneous Electron-Transfer Kinetics Using the Microjet Electrode. *J. Chem. Soc. Faraday Trans.* **1995**, *91*, 899–904.

3.6 SCHEMES AND FIGURES

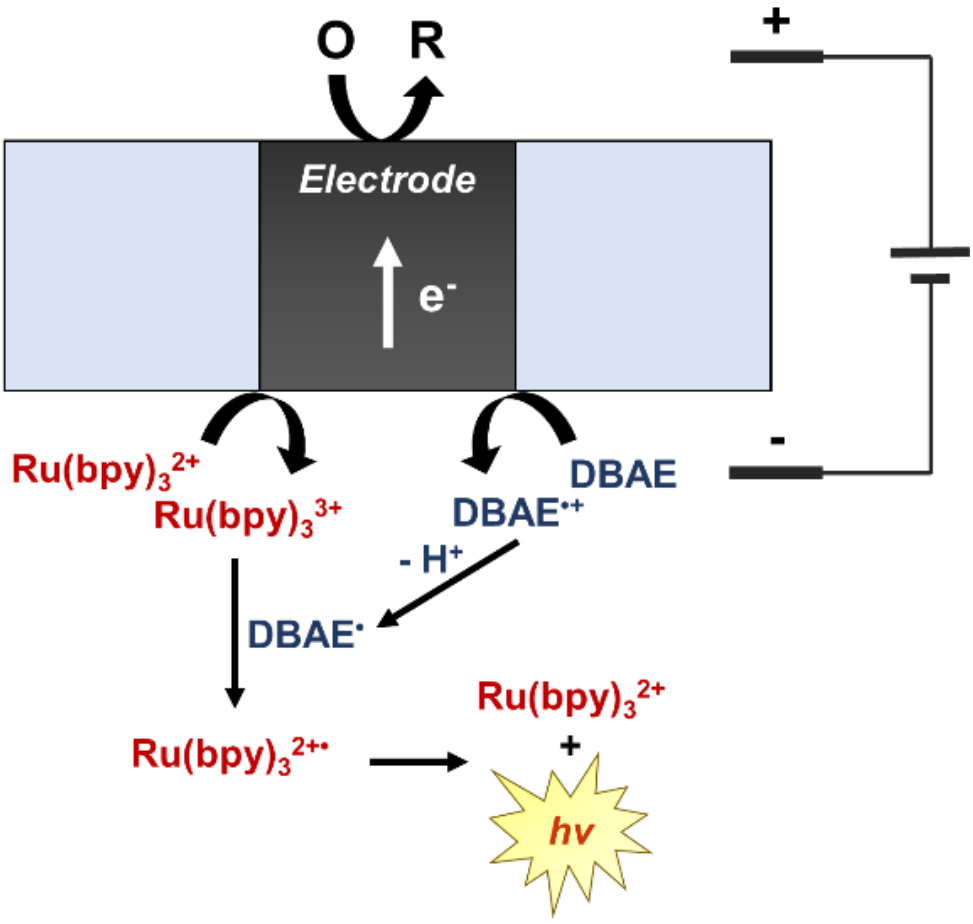

Scheme 3.1. Diagram of a reduction reaction coupled to a $Ru(bpy)_3^{2+}$-based ECL system with a 2-(dibutyl)aminoethanol (DBAE) co-reactant across a closed bipolar electrode.

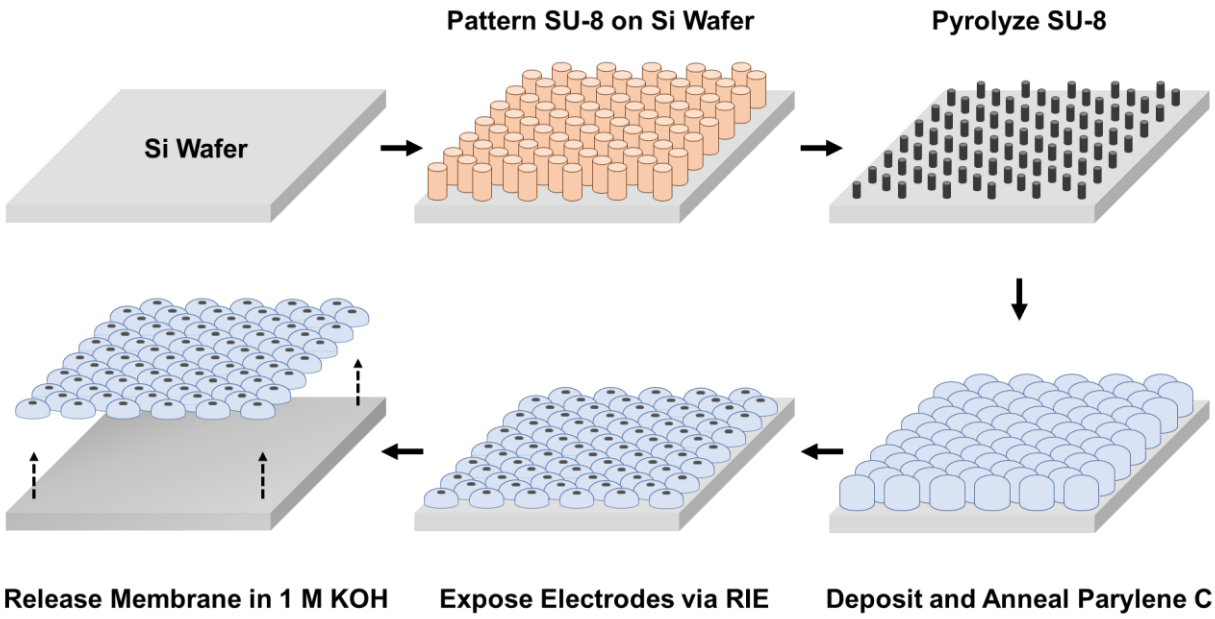

Scheme 3.2. Flowchart illustrating each step of the bipolar UME array fabrication process.

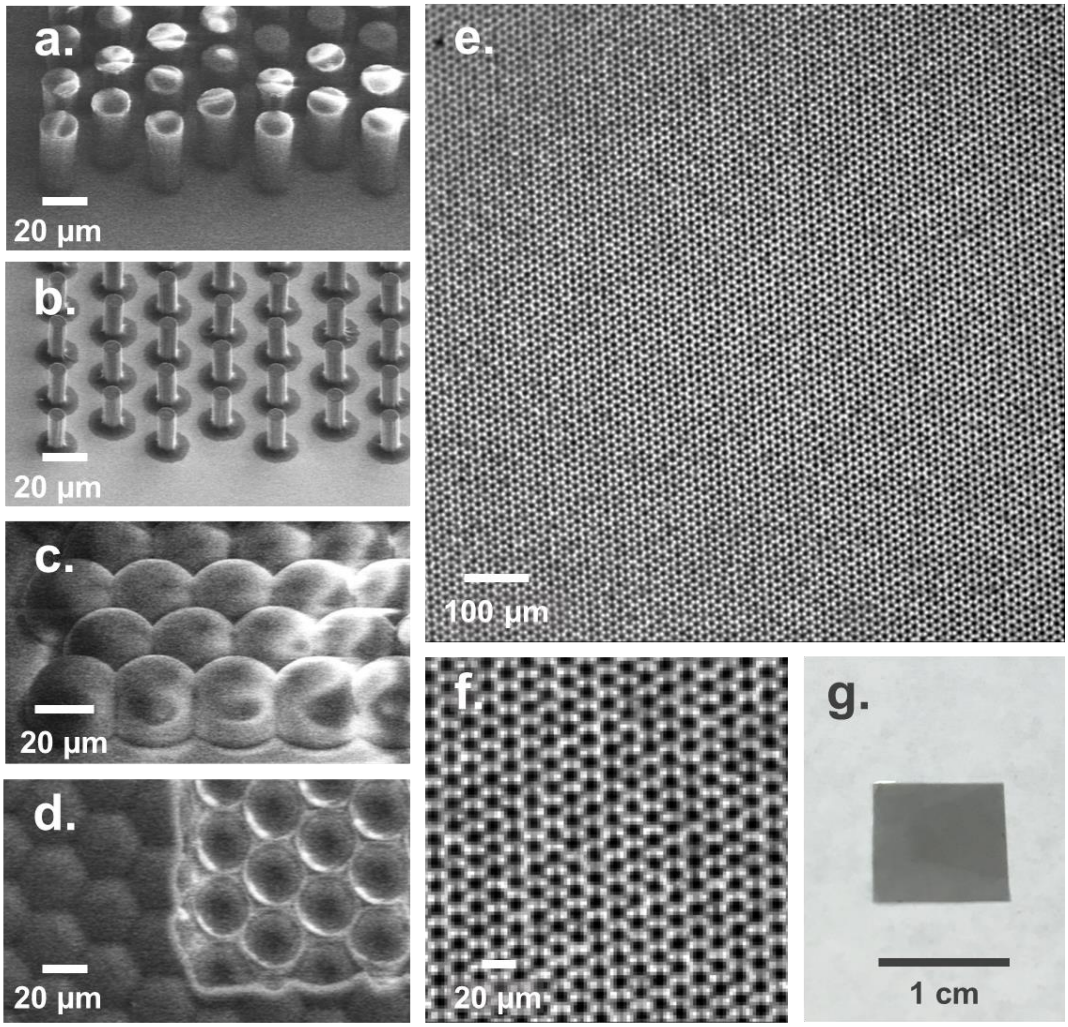

Figure 3.1. (a) SEM images of SU-8 micropillars (18 µm diameter, 40 µm height) on Si, (b) pyrolytic carbon micropillars (8 µm diameter, 18 µm height), (c) carbon micropillars coated in a 20 µm Parylene C film, (d) a portion of the pyrolytic carbon micropillars exposed. (e) Brightfield optical micrograph of the reporting surface of the array. (f) Close-up view of the array surface. (g) Photograph of a freestanding bipolar UME array.

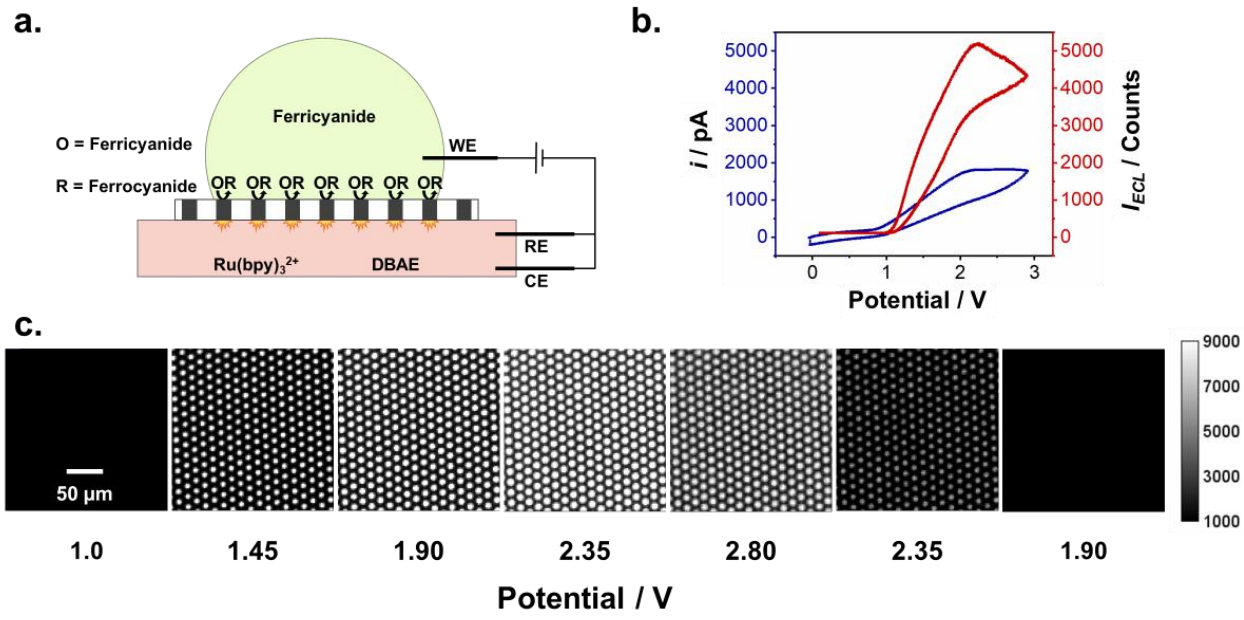

Figure 3.2. (a) Schematic of an ECL-CV coupling 100 mM $Fe(CN)_6^{3-}$ to anodic ECL across the bipolar array. Potential was swept from 0 to 2.8 to 0 V at 200 mV/s. (b) Correlation of the electrochemical (*i*-*V*) and optical (I_{ECL}-V) signals. The *i*-*V* signal is representative of the whole array, while the optical signal was averaged across a ~300 electrode subset, including the inactive substrate between electrodes. (c) ECL response from a ~300 electrode subset demonstrating the homogeneity of the I_{ECL} at each electrode for the described potentials.

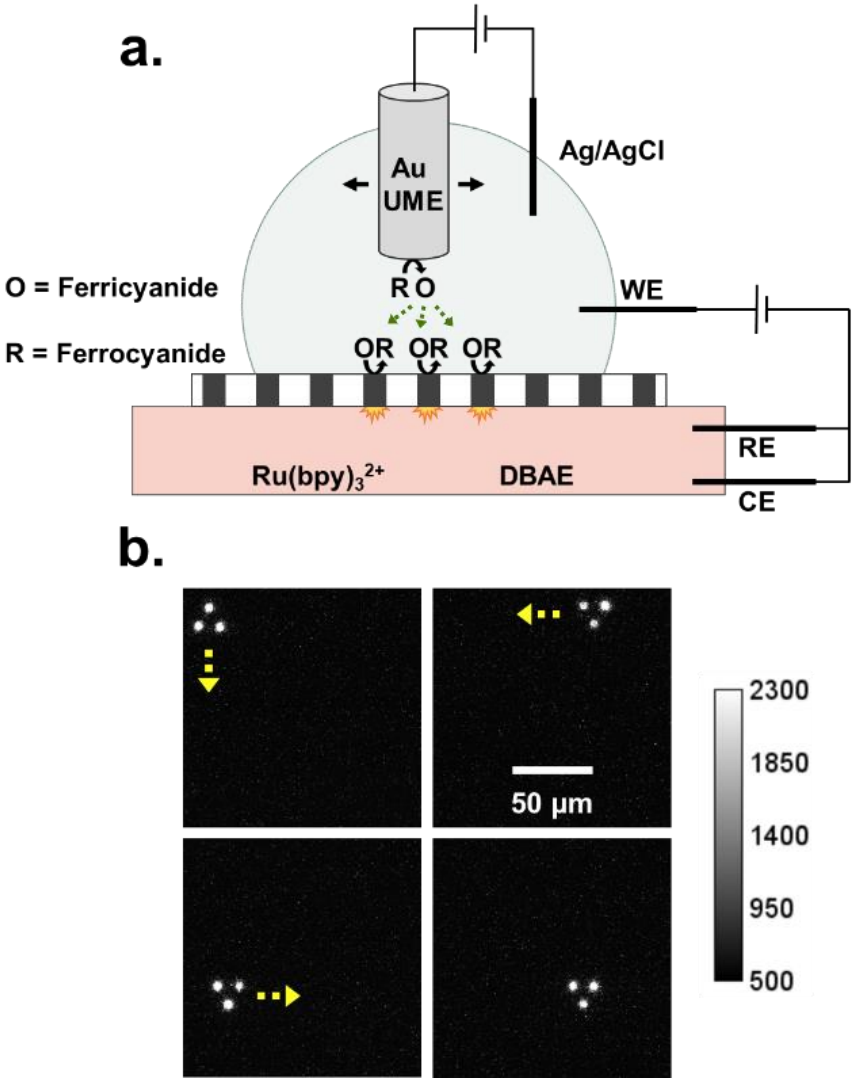

Figure 3.3. (a) Schematic showing the anodic ECL detection of a diffusion layer on an UME. $Fe(CN)_6^{4-}$ is oxidized on a 12.7 µm Au UME at +0.8 V to produce $Fe(CN)_6^{3-}$. The incident $Fe(CN)_6^{3-}$ on the array is detected by ECL at +2.0 V bias voltage. As the UME is moved laterally across the array, the detected diffusion layer precisely follows the UME movement. (b) Optical frames displaying the UME's diffusion layer movement.

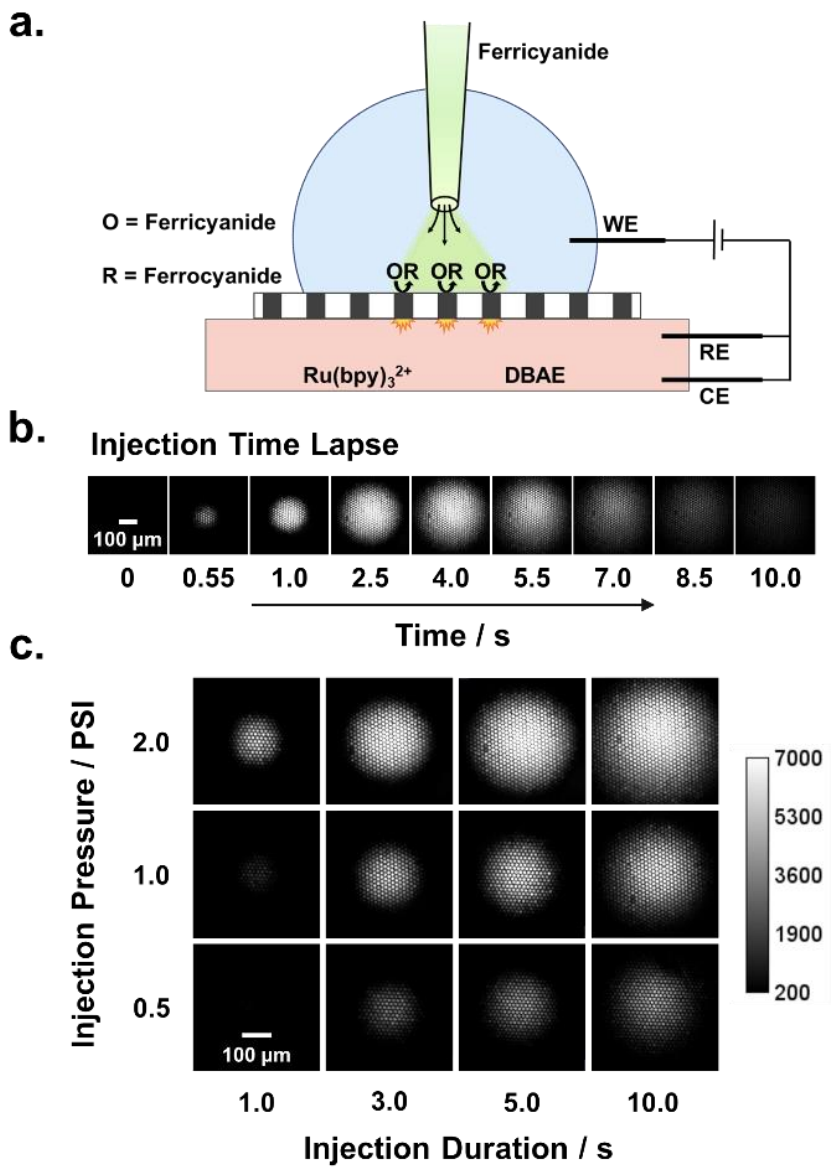

Figure 3.4. (a) Schematic displaying the injection of $Fe(CN)_6^{3-}$ from a micropipette onto the array. $Fe(CN)_6^{3-}$ was detected by coupling to anodic ECL across the biased bipolar array (+2.0 V). (b) Time-lapse images of a single injection using 2 PSI for 5 s. The variable ECL intensities are due to the detected heterogeneity in $Fe(CN)_6^{3-}$ concentration. (c) Maximum intensity frames collected during 12 independent injection experiments using the described injection pressure and duration conditions. The calibration bar to the right of (c) describes the ECL intensity for (b) and (c).

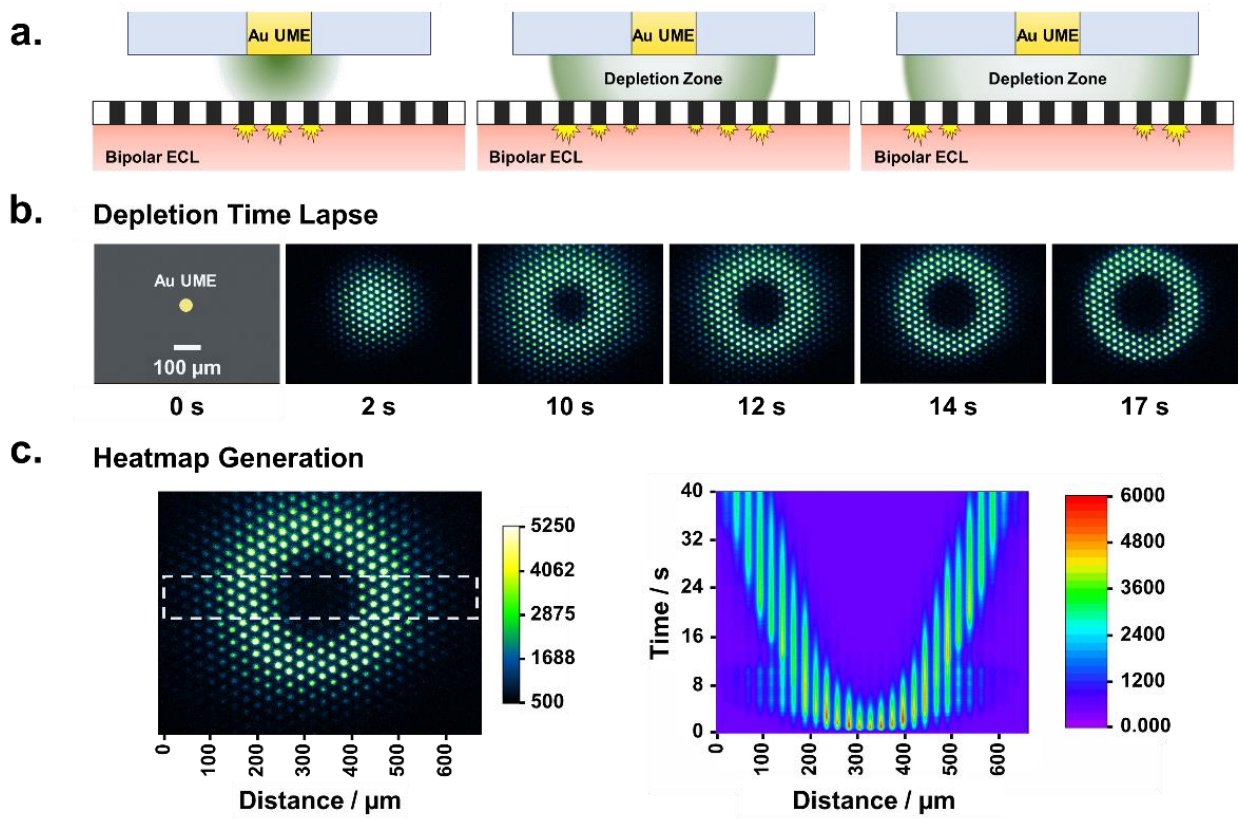

Figure 3.5. (a) Schematic showing the formation of a depletion zone in a generator-collector setup. $Fe(CN)_6^{4-}$ is oxidized on a 50 µm Au UME generating $Fe(CN)_6^{3-}$. The incident $Fe(CN)_6^{3-}$ on the biased array (+2.0 V) is visually detected by anodic ECL. A dark redox depletion zone is formed due to the consumption of $Fe(CN)_6^{4-}$ in the ~100 µm micro-gap between the UME and array. (b) Progression of the ECL response during the depletion time lapse. (c) Heatmap generated using the section of the array enclosed in the dotted white box on the left. The result on the right shows the average intensity at each distance within the selected region for the duration of the video. The calibration bars on the left and right of the heatmap are both in units of I_{ECL}.

Chapter 4

HIGH-THROUGHPUT ELECTROCATALYST SCREENING ON A MASSIVE ARRAY OF CLOSED BIPOLAR MICROELECTRODES

4.1 INTRODUCTION

Given the large number of properties which influence electrocatalytic performance (*e.g.*, particle morphology,[1] surface ligands,[2] alloy composition,[3] atomic ordering,[4] etc.), high-throughput screening methods are critical to inform the discovery and optimization of new electrocatalysts. Such screening is typically carried out via a combinatorial approach in which compositionally stepped or gradient samples are synthesized and subsequently screened to ascertain the effects of selected physical properties on the catalytic activity toward a reaction of interest.[5–7] Because the efficiency of such a scheme is partially governed by the sample creation time, this step has been targeted for improvement in various studies. Distribution of catalyst-bearing conductive inks in an arrayed pattern to enable screening of various composites is perhaps the simplest sample preparation method[8,9]; mixtures of metal salt solutions may also be dispensed in a similar manner followed by chemical or electrochemical treatment to form catalytic alloy spots of the desired metals.[10–12] However, while both of these techniques have been automated using inkjet prinking,[13] a piezodispensing apparatus,[14] or a scanning flow cell,[15] the sequential nature of such an approach greatly increases the time required for the creation of large sample libraries. Several forms of physical vapor deposition (PVD) have been employed to generate well-controlled gradients of electrocatalytic metals via co-deposition from multiple sources.[16–20] This approach is particularly attractive due to the extremely large number of alloy compositions which may be created in a single deposition, but the expense of the requisite instrumentation and metal sources renders it cost-prohibitive for many applications. Exploitation of the potential gradient along an open bipolar

electrode to manipulate the electrodeposition rates of multiple metals has also been proposed,[21] although the combinations of metals and achievable gradients are somewhat constrained by difference in redox potentials of the deposited species.

Several strategies have also been employed to maximize the throughput of electrocatalyst activity detection. Scanning techniques in which an ultramicroelectrode (UME),[11,12,14,17,22–26] reference/counter electrode couple,[27,28] optical fiber, flow cell,[29,30] or laser[31] is rastered across a catalytic surface while the current response is recorded have been extensively utilized to map the catalytic activity of compositionally varied samples, but the experiment time is typically quite long due to the use of a single probe. Individually addressable electrode arrays offer an improvement in screening parallelization,[8,9,13,18,32–35] but are limited in size due to the number of data channels which must be simultaneously monitored; additionally, fabrication of such devices is extremely challenging due to the large number of connecting leads. Optical imaging of reaction products originating from an electrocatalyst array via a pH-dependent fluorescent reporter,[10,17,32] photochromic film,[36,37] or gas bubble detection[38] provides a more rapid, albeit indirect, approach to monitoring catalytic activity, but free diffusion of the detected species limits the capacity of these techniques to screen compositional gradients.

Open bipolar electrodes (BPEs) address the majority of these shortcomings by allowing a reaction of interest to be coupled to a complementary reporter reaction via the application of an external polarizing potential, thereby providing a direct measure of catalytic activity without necessitating that electrical contact be maintained with the electrode.[19,21,39–41] When coupled with a luminescent reporter reaction such as electrochemiluminescence (ECL), this scheme yields an optical signal which is directly proportional to the catalytic current and easily scalable for many BPEs arranged in parallel.[42–44] Unfortunately, the presence of a competing ionic current pathway

in open bipolar systems necessitates the use of relatively large electrodes to yield a sufficient potential difference across the electrode surface to induce coupling,[45] thereby limiting the maximum array density and number of catalyst compositions which may be simultaneously screened. Closed BPE arrays do not possess such a parallel ionic current pathway due to segregation of the detecting and reporting solutions on opposite sides of the array, meaning that the majority of the applied potential drop occurs at the electrode solution/interface[46,47] and electrode size does not affect functionality. However, despite the absence of any constraints to array size and resolution, all of the electrocatalytic screening studies utilizing closed BPE arrays which have been carried out at the time of this writing are limited to small arrays comprised of only a handful of electrodes.[48,49]

We therefore present a highly parallelized electrocatalyst screening platform based on ECL imaging with massive microfabricated closed bipolar UME arrays which we have reported in a previous publication.[50] By imaging a subset consisting of only 4% of the surface area of one of these arrays, we are able to map the onset potentials of electrocatalytic materials deposited on over 6000 separate electrodes; this degree of screening parallelization is over an order of magnitude greater than the largest array-based electrocatalyst screening study reported in the literature.[18] Additionally, we introduce a facile method for selective electrodeposition of catalytic metals on the array surface by establishing direct electrical contact with all of the electrodes in the array using a Hg drop biased at a reducing potential. This electrodeposition scheme is much more straightforward than existing techniques for modifying BPE arrays via electrodeposition which rely on coupling metal salt reduction to a mediating oxidation reaction[49,51] and can be further extended to enable screening of a gradient in the deposited metal composition by delivering metal salt solution to the array surface via a micropipette. Lastly, we present an alternate fabrication

scheme for our closed bipolar UME arrays which incorporates an Au coating of the constituent electrodes. These Au-modified arrays are used in conjunction with the aforementioned gradient electrodeposition technique to demonstrate the utility of this platform by investigating the heterogeneity in activity of a compositionally varied metal/metal hydroxide HER electrocatalyst.

4.2 Experimental Section

4.2.1 *Array Fabrication*

Bipolar carbon UME arrays were fabricated and prepared for imaging using the same procedure described in our previous publication.[50] Au-modified arrays were fabricated using a similar procedure. However, a 200 nm Au film was first deposited onto the array surface using a sputter coater (Evatec) prior to insulation with Parylene C. Additionally, annealing was carried out after exposure of the electrodes via dry etching to prevent premature delamination of the arrays from the Si substrates.

4.2.2 *Array Modification via Electrodeposition*

Potential was controlled for all electrodeposition processes using an EG&G Princeton Applied Research Model 273A Potentiostat/Galvanostat. The Hg drop was contained on a modified microscope slide using an o-ring which was held in place with epoxy. Electrical contact was made with the Hg drop using two bundles of carbon fibers positioned on each side of the o-ring. A commercial reference electrode (BASi) and a Pt foil counter electrode were used to form an electrochemical cell over the surface of the array. Au electrodeposition was performed with 50 mM $AuCl_3$ solution at 1.5 mA for 2 min using an array half-covered with polydimethylsiloxane (PDMS). Metal salt solutions for gradient electrodeposition were delivered from a z-height of 100 µm above the array surface using a 5 µm diameter pulled quartz micropipette in conjunction with

an Eppendorf Femtojet at a pressure of 0.22 PSI for 100 s. An Olympus CK40 inverted microscope and electronic micromanipulator (Sutter) were used to position the pipette prior to injection. All gradient electrodepositions were carried out in a 100 mM KCl supporting electrolyte solution. Pt deposition was performed by injection of 50 mM $PtCl_4$ solution at -0.1 V vs. Ag/AgCl; $Ni(OH)_2$ deposition was performed by injection of 1 M $NiCl_2$ 100 mM NaCl pH 3.6 solution at -1 V vs. Ag/AgCl followed by cycling from 0.1 to 0.5 V vs. Ag/AgCl at 5 mV/s in 100 mM KOH for 25 cycles.

4.2.3 *Imaging of Electrocatalytic Activity*

Potential was driven across the array using an EG&G Princeton Applied Research Model 175 universal programmer linked to a 3-electrode CV-27 potentiostat (BAS) with 3 Ag/AgCl electrodes. Reference and counter electrodes were placed in the bottom ECL solution and the working electrode was placed in the top solution. Wires were freshly chlorided prior to each experiment using a 1:1 solution of 70% HNO_3 and 3 M KCl. All imaging experiments were recorded on an Andor iXon 897E EMCCD camera cooled to -80 ^oC with 30 ms exposure, 300 EM Gain, 5.1x pre-amplifier gain, 0.3 µs vertical pixel shift speed, and 10 MHz readout rate. Videos contained 1500 frames with 512×512 pixels. An Olympus IX70 microscope equipped with a 4x (0.1 NA Olympus Plan N) objective was used to image the array. Each pixel measured 3.92 µm, yielding a 4.0×10^6 μm^2 field of view and allowing ~6000 full electrodes in each frame. The ECL solution below the array was contained on the microscope stage using a home-built device fabricated from three 1.0 mm thick glass slides (VWR). One slide was used as the base and two were positioned laterally about 1 cm apart, creating a 1 mm deep channel for ECL solution containment. Epoxy was used to prevent solution leakage.

ECL voltammograms of the HER in acid were collected using a driving voltage sweep of 0 to 3 V vs. Ag/AgCl at 200 mV/s to couple the HER in 100 mM $HClO_4$ 100 mM NaCl above the array to anodic ECL in 25 mM $Ru(bpy)_3^{2+}$ 20 mM DBAE 100 mM phosphate buffer (PB) pH 7.4 below the array; alkaline HER ECL voltammograms were collected using a driving voltage sweep of 0 to 4 V vs. Ag/AgCl at 200 mV/s to couple HER in 100 mM KOH to the same anodic ECL solution. The camera and potentiostat were simultaneously triggered using a custom LabVIEW 2013 program and ECL intensity-potential (I_{ECL}-V) videos were collected using the conditions described above.

4.2.4 *Analysis of ECL Video Data*

ImageJ was used to designate each electrode as a separate region of interest (ROI) in the collected videos and extract the ECL intensity traces for all electrodes. These traces were then analyzed using a custom Python script which determined the frame number at which the ECL intensity first exceeded 180 counts and converted this value to an applied potential using the voltage scan rate. These potentials were then assigned color values and mapped to their corresponding ROIs to yield false color plots of the coupling onset potentials of the electrodes.

4.2.5 *$Ni(OH)_2$ Modification of Au UME*

The Au electrode was fabricated by sealing a piece of Au wire in a glass capillary[52] prior to characterization using cyclic voltammetry in 1 mM FcMeOH 100 mM KCl solution. Variable $Ni(OH)_2$ coverage was achieved by immersing the electrode in the aforementioned $NiCl_2$ solution for intervals ranging from 10 s to 5 min. Alkaline HER activity was evaluated by monitoring the current response of the UME in 100 mM KOH using a potential sweep of 0 to -2 V vs. Ag/AgCl

at 200 mV/s. The electrode was polished after the collection of each voltammogram to regenerate the Au surface.

4.3 Results and Discussion

4.3.1 *Modification of Bipolar UME Arrays via Electrodeposition*

To facilitate electrodeposition of a catalytic metal on the detecting side of a carbon bipolar UME array, a Hg drop was used to make electrical contact with the reporting poles of all electrodes in the array which allowed the same potential to be simultaneously applied across the array's entire electroactive surface and eliminated the need for bipolar coupling of the metal salt reduction to a separate oxidation mediator reaction. This approach also offers the benefit of enabling selective modification of subsets of the array by blocking off portions of the lower surface with thin sheets of polydimethylsiloxane (PDMS) before bringing it in contact with the Hg, thereby preventing electrodeposition from occurring in these regions. To carry out an electrodeposition, the well on the detecting side of array was first filled with a metal salt solution, after which the opposite side was brought into contact with the Hg drop. An Ag/AgCl reference electrode and Pt foil counter electrode were then immersed in the solution to form an electrochemical cell in which the array served as the working electrode (see **Figure 4.1a**).

Figure 4.1b shows an example of an array which was modified with Au in this manner across half of the surface via galvanostatic electrodeposition from a 50 mM solution of $AuCl_3$. The uniformity of the Au distribution indicates both that electrical contact was made with all of the electrodes and that a consistent potential was applied across the surface. The Au overgrowth observed in **Figure 4.1b** at the border between the modified and unmodified portions of the array may be attributed to the higher Au ion concentration which existed along this boundary due to depletion of metal ions above the half of the array which experienced a potential bias. Note that

the residue observed on the representative bare carbon electrode shown in **Figure 4.1c** may be attributed to salt deposits left behind after drying the array.

4.3.2 *Gradient Electrodeposition of Electrocatalysts*

Although the preceding selective electrodeposition method can be leveraged to enable comparative catalytic studies of the activity of various material compositions deposited sequentially across adjacent regions of a carbon bipolar UME array, such a process would be extremely time-consuming and does not take full advantage of the array's impressive resolution and imaging capacity. To introduce a radial gradient in the amount of catalytic metal deposited across an array, a method was devised in which a plume of metal salt solution was delivered to the biased array surface via a micropipette in a process similar in principle to other studies in which a redox species was "puffed" toward the surface of an electrode immersed in supporting electrolyte solution[50,53,54] (see step 1 of **Scheme 1**). First, the well on the detecting side of an array was filled with supporting electrolyte solution, after which the opposite side was brought into contact with the Hg drop and a reference electrode and Pt foil counter electrode were immersed in the electrolyte solution. Next, a 5 μm diameter micropipette filled with a metal salt solution was lowered through a hole in the counter electrode and held ~100 μm above the array surface. The Hg drop was then biased at a reducing potential and a pressure-injection module was used to dispense the metal salt solution at the surface of the array. Due to dilution of the pipette contents by the surrounding electrolyte solution after injection, a metal ion concentration gradient was formed about the pipette orifice over the course of the deposition.[55] **Figure 4.2f** shows an energy dispersive spectroscopy (EDS) map of the results of a Pt injection/deposition experiment with the corresponding scanning electron microscopy (SEM) image displayed in **Figure C1**. Note that there is a clear radial decrease in the amount of metal deposited on the electrodes about the injection site with the tailing observed

toward the upper portion of the image being due to positioning the pipette at a slight angle from normal to the array surface.

4.3.3 *Electrocatalyst Screening via Bipolar Coupling to ECL*

After modification of an array via this gradient electrodeposition technique, the activity of the Pt-modified electrodes toward the hydrogen evolution reaction (HER) was imaged via coupling to a $Ru(bpy)_3^{2+}$-based ECL system with the aim of demonstrating the applicability of this platform toward highly parallelized electrocatalyst screening (see step 2 of **Scheme 4.1**). The well on the detecting side of a metal-modified array was first filled with an acid solution, after which the reporting side was immersed in anodic ECL solution and the driving voltage across the array swept from 0 to 3 V; this applied potential induced coupling of the HER on one side of the array to anodic ECL on the other, the intensity of which was monitored and recorded as a video. Given that the current through an electrode of a bipolar array is directly related to the ECL intensity emanating from its reporting pole, the intensity vs. driving voltage trace (I_{ECL}-V) for each electrode could be used to determine the applied potential necessary to bring about the onset of HER.

Mapping of HER onset driving voltage for all of the electrodes in an array was carried out using a custom Python script which extracted I_{ECL}-V traces for all ~6000 electrodes in the field-of-view and separately determined the driving potential necessary for each electrode to reach an ECL intensity threshold slightly above the noise level of the camera (180 counts). Since the applied potential necessary to induce coupling across a closed bipolar system is equal to the difference in formal potentials of the two half reactions and given that the formal potential of the reporter reaction is constant for all electrodes, a difference in the driving potential at the onset of ECL coupling for two electrodes equates to their difference in HER onset potential. **Figure 4.2e** shows the false color plot corresponding to the Pt deposition mapped in **Figure 4.2f**. Note that electrodes

at the center of the injection site exhibit the lowest HER onset potentials, but these values quickly increase for electrodes located further away from this position. Also, the same tailing which was observed in the EDS map covers an even greater area in this plot, indicating that imaging the catalytic activity via this scheme is even more sensitive than EDS for detecting the presence of Pt.

After mapping the HER performance across the deposition site, SEM was used to examine the metal coverage of individual electrodes. Due to the geometric arrangement of the arrayed electrodes and the excellent contrast between the deposited Pt and underlying carbon, imaging of specific electrodes exhibiting an ECL signal of interest was relatively straightforward (see designated electrodes in **Figure 4.2e**). As should be expected, a positive correlation between the catalytic performance of individual electrodes and the coverage of Pt on the surface was qualitatively established (**Figures 4.2a-d**). Such a relationship is to be expected given the higher local metal ion concentration present about the pipette orifice during injection which would result in greater amounts of Pt on the nearby electrodes. These results demonstrate the efficacy of this gradient electrodeposition method coupled with bipolar coupling and ECL imaging as a high-throughput platform for generating and screening large pools of compositionally gradient electrocatalyst samples.

4.3.4 *Screening Electrocatalyst Composition with Au-Modified Bipolar UME Arrays*

To further expand the applications of this array-based catalysis imaging scheme toward the investigation of more complex interfacial and bimetallic catalytic systems, the fabrication scheme for the carbon bipolar UME arrays was updated to incorporate a metal coating on the electrodes' detecting poles. Au was selected as the modifying material due to its ease of patterning via wet etching. Briefly, 200 nm of Au was sputtered over the surface of the devices immediately following pyrolysis, after which the Au-coated electrodes were insulated in Parylene C and exposed via

plasma etching. The arrays were annealed in a tube furnace at 400°C under a N_2 flow which typically resulted in delamination of the devices from the substrate. Each released array was then epoxied to a well on its upper surface, after which the lower surface was immersed in Au etchant to remove the metal connecting the individual electrodes. This same process may be readily extended to facilitate modification of a bipolar UME array with any other metal which can be wet etched. Note that the reporting poles of these Au-coated arrays still consist of bare carbon to ensure that the kinetics of the ECL reporter reaction remain unchanged relative to the original unmodified design. The resulting arrays appeared extremely uniform under SEM characterization (see **Figure 4.3a,b**) and revealed virtually identical optical responses from all electrodes when used to couple HER in acidic solution to anodic ECL (**Figure 4.3c**).

A metal/metal hydroxide electrocatalyst was selected for investigation to demonstrate the utility of these Au-coated arrays in interfacial catalyst screening and compositional optimization studies. This electrocatalytic scheme was originally introduced to enhance the HER activity of Pt in alkaline solution by decorating the metal surface with $Ni(OH)_2$ islands to encourage adsorption of OH on the metal hydroxide clusters and H on the Pt surface, thereby promoting water dissociation which is the rate determining step of the HER in basic solution.[56] Modification with metal hydroxides has since been demonstrated to similarly improve the HER performance of other transition metal electrocatalysts (such as Au, Ag, Cu, Ru etc.) which underperform in basic solution due to slow water dissociation kinetics.[57–59] However, oversaturation of the electrode surface results in adverse effects to HER activity due to the poor conductivity of $Ni(OH)_2$[60–62] and obstruction of active sites on the transition metal surface necessary for H adsorption.[63–65] Such a prediction therefore implies the existence of an optimum degree of metal hydroxide surface

coverage for maximum electrocatalyst performance; this proposed relationship will be further explored here.

An initial experiment to confirm the predicted link between these two parameters was carried out using a 25 μm Au UME in which the electrode was immersed in a $NiCl_2$ solution for intervals ranging from 10 s to 5 min to modify the surface with increasing amounts of $Ni(OH)_2$.[57] The UME was then rinsed with DI water and transferred to 100 mM KOH where its potential was scanned from 0 to -2 V vs. Ag/AgCl and the resulting current response recorded. Note from **Figure 4.4a** that immersion times of 10 s and 1 min in the $NiCl_2$ solution result in corresponding decreases in HER onset potential relative to the unmodified Au surface; however, an immersion time of 5 min displays a drastic negative shift in current onset with the observed response reduced to almost zero over the displayed potential range. This reduction in activity is consistent with blockage of the electrode surface by the metal hydroxide despite the synergistic enhancement to alkaline HER activity which was brought on by initial modification.

To further verify this relationship in a more parallelized fashion, a gradient of $Ni(OH)_2$ was generated across the surface of an Au-coated array by first employing a micropipette to dispense a concentrated $NiCl_2$ solution at the array surface which was contacting a Hg drop biased at a reducing potential; pipette diameter, distance from the array surface, injection pressure/time, and bulk electrolyte concentration were unchanged from the Pt deposition conditions. The electrolyte solution was then replaced with 100 mM KOH and the applied potential scanned[66,67] between 0.1 and 0.5 V vs. Ag/AgCl at 5 mV/s to oxidize the deposited Ni to $Ni(OH)_2$; potential cycling was ceased after 25 cycles when the anodic current was observed to be zero. **Figure C2e** shows a representative EDS map of a $Ni(OH)_2$ gradient generated on an Au-coated array which exhibits a clear radial decrease in Ni signal about the location of the micropipette injection. Additionally,

SEM micrographs of selected electrodes from the EDS map confirm this trend in deposited $Ni(OH)_2$, with coverage ranging from almost total encapsulation of the electrode surfaces near the center of the spot to virtually nothing at the periphery (**Figure C2a-d**). Note, however, that the nature of the SEM/EDS sample prep (*i.e.*, affixation to a Si substrate with conductive epoxy followed by carbon coating) prevented further use of arrays characterized in this fashion. Subsequent experiments were therefore carried out with identically prepared devices.

After $Ni(OH)_2$ deposition, the HER activity of the array in 100 mM KOH was imaged via coupling to anodic ECL using a driving potential scan of 0 to 4 V vs. Ag/AgCl (see **Figure 4.4b**). The resulting activity false color plot (**Figure 4.4c**) for the center of the $Ni(OH)_2$ gradient exhibits a ~300 mV decrease in the magnitude of HER onset potential relative to bare Au for electrodes located in a narrow ~250 μm diameter ring with less pronounced enhancements to activity being observed outside this region. This increase in activity is consistent with the potential shift observed for the voltammogram exhibiting the highest HER activity in **Figure 4.4a** (1 min immersion time). The presence of this peak in activity indicates that optimal modification of the Au surface was achieved at this point in the radial $Ni(OH)_2$ gradient about the deposition site, with higher or lower coverage outside this region resulting in diminished catalytic performance (the zone exhibiting extremely low activity in the upper right of the plot is due to the application of epoxy which was used to seal a defect in the array). These results further confirm the predicted nature of the relationship between alkaline HER performance and the surface coverage of the modifying metal hydroxide on a transition metal surface and also demonstrate the utility of this gradient deposition technique and array-based screening platform in exploring the effects of compositional variation on electrocatalytic activity.

4.4 CONCLUSIONS

In summary, we have demonstrated the use of massive bipolar UME arrays in conjunction with ECL imaging as a high-throughput platform capable of simultaneously screening several thousand electrocatalyst compositions. Additionally, we have introduced a complementary technique for electrodeposition of a radial gradient of catalytic metal on the surface of these arrays for the purpose of rapidly generating large quantities of compositionally varied electrocatalyst samples. Lastly, we have utilized both of these methods in conjunction with a new process for uniform metal modification of the aforementioned arrays to investigate the impact of varied $Ni(OH)_2$ coverage on the HER activity of an Au surface in alkaline solution, with the catalytic performance of the modified Au being confirmed to exhibit a peak-shaped dependence on increasing $Ni(OH)_2$ coverage. Future work will focus on further expanding this platform to enable the screening of metal alloys by incorporating additional micropipettes for the purpose of simultaneously delivering multiple metal salt solutions to the array surface during the gradient electrodeposition process; X-ray photoelectron spectroscopy (XPS) measurements of catalyst compositions will also be the focus of subsequent studies.

Note: This chapter is adapted with permission from Anderson, T. J.; Defnet, P. A.; Cheung, R. A.; Zhang, B. "High-Throughput Electrocatalyst Screening on a Massive Array of Bipolar Ultramicroelectrodes." J. Electrochem. Soc. **2021**, *in review*. This is an unofficial adaptation of an article that has been submitted to an IOP publication. IOP has not endorsed the content of this adaptation or the context of its use.

4.5 REFERENCES

(1) Wang, Y.-J.; Zhao, N.; Fang, B.; Li, H.; Bi, X. T.; Wang, H. Carbon-Supported Pt-Based Alloy Electrocatalysts for the Oxygen Reduction Reaction in Polymer Electrolyte Membrane Fuel Cells: Particle Size, Shape, and Composition Manipulation and Their Impact to Activity. *Chem. Rev.* **2015**, *115*, 3433–3467.

(2) Lenne, Q.; Leroux, Y. R.; Lagrost, C. Surface Modification for Promoting Durable, Efficient, and Selective Electrocatalysts. *ChemElectroChem* **2020**, *7*, 2345–2363.

(3) Wang, C.; Markovic, N. M.; Stamenkovic, V. R. Advanced Platinum Alloy Electrocatalysts for the Oxygen Reduction Reaction. *ACS Catal.* **2012**, *2*, 891–898.

(4) Gamler, J. T. L.; Ashberry, H. M.; Skrabalak, S. E.; Koczkur, K. M. Random Alloyed versus Intermetallic Nanoparticles: A Comparison of Electrocatalytic Performance. *Adv. Mater.* **2018**, *30*, 1801563.

(5) Smotkin, E. S.; Díaz-Morales, R. R. New Electrocatalysts by Combinatorial Methods. *Annu. Rev. Mater. Res.* **2003**, *33*, 557–579.

(6) Jeon, M. K.; Lee, C. H.; Park, G. I.; Kang, K. H. Combinatorial Search for Oxygen Reduction Reaction Electrocatalysts: A Review. *J. Power Sources* **2012**, *216*, 400–408.

(7) Antolini, E. Evaluation of the Optimum Composition of Low-Temperature Fuel Cell Electrocatalysts for Methanol Oxidation by Combinatorial Screening. *ACS Comb. Sci.* **2017**, *19*, 47–54.

(8) Guerin, S.; Hayden, B. E.; Lee, C. E.; Mormiche, C.; Owen, J. R.; Russell, A. E.; Theobald, B.; Thompsett, D. Combinatorial Electrochemical Screening of Fuel Cell Electrocatalysts. *J. Comb. Chem.* **2004**, *6*, 149–158.

(9) Smotkin, E. S.; Jiang, J.; Nayar, A.; Liu, R. High-Throughput Screening of Fuel Cell Electrocatalysts. *Appl. Surf. Sci.* **2006**, *252*, 2573–2579.

(10) Reddington, E. Combinatorial Electrochemistry: A Highly Parallel, Optical Screening Method for Discovery of Better Electrocatalysts. *Science* **1998**, *280*, 1735–1737.

(11) Jayaraman, S.; Hillier, A. C. Screening the Reactivity of $Pt_x Ru_y$ and $Pt_x Ru_y Mo_z$ Catalysts toward the Hydrogen Oxidation Reaction with the Scanning Electrochemical Microscope. *J. Phys. Chem. B* **2003**, *107*, 5221–5230.

(12) Fernández, J. L.; White, J. M.; Sun, Y.; Tang, W.; Henkelman, G.; Bard, A. J. Characterization and Theory of Electrocatalysts Based on Scanning Electrochemical Microscopy Screening Methods. *Langmuir* **2006**, *22*, 10426–10431.

(13) Spong, A. D.; Vitins, G.; Guerin, S.; Hayden, B. E.; Russell, A. E.; Owen, J. R. Combinatorial Arrays and Parallel Screening for Positive Electrode Discovery. *J. Power Sources* **2003**, *119–121*, 778–783.

(14) Fernández, J. L.; Walsh, D. A.; Bard, A. J. Thermodynamic Guidelines for the Design of Bimetallic Catalysts for Oxygen Electroreduction and Rapid Screening by Scanning Electrochemical Microscopy. M−Co (M: Pd, Ag, Au). *J. Am. Chem. Soc.* **2005**, *127*, 357–365.

(15) Latyshev, V.; Vorobiov, S.; Shylenko, O.; Komanicky, V. Fabrication of Combinatorial Material Libraries by Flow Cell Electrodeposition Technique. *Mater. Lett.* **2020**, *281*, 128594.

(16) Guerin, S.; Hayden, B. E. Physical Vapor Deposition Method for the High-Throughput Synthesis of Solid-State Material Libraries. *J. Comb. Chem.* **2006**, *8*, 66–73.

(17) Prochaska, M.; Jin, J.; Rochefort, D.; Zhuang, L.; DiSalvo, F. J.; Abruña, H. D.; van Dover, R. B. High Throughput Screening of Electrocatalysts for Fuel Cell Applications. *Rev. Sci. Instrum.* **2006**, *77*, 054104.

(18) Guerin, S.; Hayden, B. E.; Lee, C. E.; Mormiche, C.; Russell, A. E. High-Throughput Synthesis and Screening of Ternary Metal Alloys for Electrocatalysis. *J. Phys. Chem. B* **2006**, *110*, 14355–14362.

(19) Latyshev, V.; Vorobiov, S.; Shylenko, O.; Komanicky, V. Screening of Electrocatalysts for Hydrogen Evolution Reaction Using Bipolar Electrodes Fabricated by Composition Gradient Magnetron Sputtering. *J. Electroanal. Chem.* **2019**, *854*, 113562.

(20) Yang, Y.; Chen, G.; Zeng, R.; Villarino, A. M.; DiSalvo, F. J.; van Dover, R. B.; Abruña, H. D. Combinatorial Studies of Palladium-Based Oxygen Reduction Electrocatalysts for Alkaline Fuel Cells. *J. Am. Chem. Soc.* **2020**, *142*, 3980–3988.

(21) Termebaf, H.; Shayan, M.; Kiani, A. Two-Step Bipolar Electrochemistry: Generation of Composition Gradient and Visual Screening of Electrocatalytic Activity. *Langmuir* **2015**, *31*, 13238–13246.

(22) Minguzzi, A.; Alpuche-Aviles, M. A.; López, J. R.; Rondinini, S.; Bard, A. J. Screening of Oxygen Evolution Electrocatalysts by Scanning Electrochemical Microscopy Using a Shielded Tip Approach. *Anal. Chem.* **2008**, *80*, 4055–4064.

(23) Minguzzi, A.; Battistel, D.; Rodríguez-López, J.; Vertova, A.; Rondinini, S.; Bard, A. J.; Daniele, S. Rapid Characterization of Oxygen-Evolving Electrocatalyst Spot Arrays by the Substrate Generation/Tip Collection Mode of Scanning Electrochemical Microscopy with Decreased O_2 Diffusion Layer Overlap. *J. Phys. Chem. C* **2015**, *119*, 2941–2947.

(24) Li, W.; Fan, F.-R. F.; Bard, A. J. The Application of Scanning Electrochemical Microscopy to the Discovery of Pd–W Electrocatalysts for the Oxygen Reduction Reaction That Demonstrate High Activity, Stability, and Methanol Tolerance. *J. Solid State Electrochem.* **2012**, *16*, 2563–2568.

(25) Walsh, D. A.; Fernández, J. L.; Bard, A. J. Rapid Screening of Bimetallic Electrocatalysts for Oxygen Reduction in Acidic Media by Scanning Electrochemical Microscopy. *J. Electrochem. Soc.* **2006**, *153*, E99.

(26) Jung, C.; Sánchez-Sánchez, C. M.; Lin, C.-L.; Rodríguez-López, J.; Bard, A. J. Electrocatalytic Activity of Pd−Co Bimetallic Mixtures for Formic Acid Oxidation Studied by Scanning Electrochemical Microscopy. *Anal. Chem.* **2009**, *81*, 7003–7008.

(27) Lee, K. R.; Jeon, M. K.; Woo, S. I. Composition Optimization of PtRuM/C (M=Fe and Mo) Catalysts for Methanol Electro-Oxidation via Combinatorial Method. *Appl. Catal. B Environ.* **2009**, *91*, 428–433.

(28) Lee, K. R.; Jung, Y.; Woo, S. I. Combinatorial Screening of Highly Active Pd Binary Catalysts for Electrochemical Oxygen Reduction. *ACS Comb. Sci.* **2012**, *14*, 10–16.

(29) Schuppert, A. K.; Topalov, A. A.; Katsounaros, I.; Klemm, S. O.; Mayrhofer, K. J. J. A Scanning Flow Cell System for Fully Automated Screening of Electrocatalyst Materials. *J. Electrochem. Soc.* **2012**, *159*, F670.

(30) Lai, Y.; Jones, R. J. R.; Wang, Y.; Zhou, L.; Gregoire, J. M. Scanning Electrochemical Flow Cell with Online Mass Spectroscopy for Accelerated Screening of Carbon Dioxide Reduction Electrocatalysts. *ACS Comb. Sci.* **2019**, *21*, 692–704.

(31) Woodhouse, M.; Parkinson, B. A. Combinatorial Discovery and Optimization of a Complex Oxide with Water Photoelectrolysis Activity. *Chem. Mater.* **2008**, *20*, 2495–2502.

(32) Sullivan, M. G.; Utomo, H.; Fagan, P. J.; Ward, M. D. Automated Electrochemical Analysis with Combinatorial Electrode Arrays. *Anal. Chem.* **1999**, *71*, 4369–4375.

(33) Strasser, P.; Fan, Q.; Devenney, M.; Weinberg, W. H.; Liu, P.; Nørskov, J. K. High Throughput Experimental and Theoretical Predictive Screening of Materials − A Comparative Study of Search Strategies for New Fuel Cell Anode Catalysts. *J. Phys. Chem. B* **2003**, *107*, 11013–11021.

(34) Dang, T.; Ramsaran, R.; Roy, S.; Froehlich, J.; Wang, J.; Kubiak, C. P. Design of a High Throughput 25-Well Parallel Electrolyzer for the Accelerated Discovery of CO2 Reduction Catalysts via a Combinatorial Approach. *Electroanalysis* **2011**, *23*, 2335–2342.

(35) Zhang, Y.; McGinn, P. J. Combinatorial Screening for Methanol Oxidation Catalysts in Alloys of Pt, Cr, Co and V. *J. Power Sources* **2012**, *206*, 29–36.

(36) Brace, K. M.; Hayden, B. E.; Russell, A. E.; Owen, J. R. A Parallel Optical Screen for the Rapid Combinatorial Electrochromic Analysis of Electrochemical Materials. *Adv. Mater.* **2006**, *18*, 3253–3257.

(37) Jaramillo, T. F.; Ivanovskaya, A.; McFarland, E. W. High-Throughput Screening System for Catalytic Hydrogen-Producing Materials. *J. Comb. Chem.* **2002**, *4*, 17–22.

(38) Xiang, C.; Suram, S. K.; Haber, J. A.; Guevarra, D. W.; Soedarmadji, E.; Jin, J.; Gregoire, J. M. High-Throughput Bubble Screening Method for Combinatorial Discovery of Electrocatalysts for Water Splitting. *ACS Comb. Sci.* **2014**, *16*, 47–52.

(39) Fosdick, S. E.; Crooks, R. M. Bipolar Electrodes for Rapid Screening of Electrocatalysts. *J. Am. Chem. Soc.* **2012**, *134*, 863–866.

(40) Fosdick, S. E.; Berglund, S. P.; Mullins, C. B.; Crooks, R. M. Parallel Screening of Electrocatalyst Candidates Using Bipolar Electrochemistry. *Anal. Chem.* **2013**, *85*, 2493–2499.

(41) Fosdick, S. E.; Berglund, S. P.; Mullins, C. B.; Crooks, R. M. Evaluating Electrocatalysts for the Hydrogen Evolution Reaction Using Bipolar Electrode Arrays: Bi- and Trimetallic Combinations of Co, Fe, Ni, Mo, and W. *ACS Catal.* **2014**, *4*, 1332–1339.

(42) Chow, K.-F.; Mavré, F.; Crooks, R. M. Wireless Electrochemical DNA Microarray Sensor. *J. Am. Chem. Soc.* **2008**, *130*, 7544–7545.

(43) Chow, K.-F.; Mavré, F.; Crooks, J. A.; Chang, B.-Y.; Crooks, R. M. A Large-Scale, Wireless Electrochemical Bipolar Electrode Microarray. *J. Am. Chem. Soc.* **2009**, *131*, 8364–8365.

(44) Mavré, F.; Chow, K.-F.; Sheridan, E.; Chang, B.-Y.; Crooks, J. A.; Crooks, R. M. A Theoretical and Experimental Framework for Understanding Electrogenerated Chemiluminescence (ECL) Emission at Bipolar Electrodes. *Anal. Chem.* **2009**, *81*, 6218–6225.

(45) Fosdick, S. E.; Knust, K. N.; Scida, K.; Crooks, R. M. Bipolar Electrochemistry. *Angew. Chem. Int. Ed.* **2013**, *52*, 10438–10456.

(46) Cox, J. T.; Guerrette, J. P.; Zhang, B. Steady-State Voltammetry of a Microelectrode in a Closed Bipolar Cell. *Anal. Chem.* **2012**, *84*, 8797–8804.

(47) Guerrette, J. P.; Oja, S. M.; Zhang, B. Coupled Electrochemical Reactions at Bipolar Microelectrodes and Nanoelectrodes. *Anal. Chem.* **2012**, *84*, 1609–1616.

(48) Lin, X.; Zheng, L.; Gao, G.; Chi, Y.; Chen, G. Electrochemiluminescence Imaging-Based High-Throughput Screening Platform for Electrocatalysts Used in Fuel Cells. *Anal. Chem.* **2012**, *84*, 7700–7707.

(49) Zhang, J.-D.; Hao, N.; Lu, L.; Yun, S.; Zhu, X.-F.; Hong, K.; Feng, L.-D. High-Efficient Preparation and Screening of Electrocatalysts Using a Closed Bipolar Electrode Array System. *J. Electroanal. Chem.* **2019**, *832*, 1–6.

(50) Anderson, T. J.; Defnet, P. A.; Zhang, B. Electrochemiluminescence (ECL)-Based Electrochemical Imaging Using a Massive Array of Bipolar Ultramicroelectrodes. *Anal. Chem.* **2020**, *92*, 6748–6755.

(51) Guerrette, J. P.; Percival, S. J.; Zhang, B. Fluorescence Coupling for Direct Imaging of Electrocatalytic Heterogeneity. *J. Am. Chem. Soc.* **2013**, *135*, 855–861.

(52) Defnet, P. A.; Zhang, B. Detection of Transient Nanoparticle Collision Events Using Electrochemiluminescence on a Closed Bipolar Microelectrode. *ChemElectroChem* **2020**, *7*, 252–259.

(53) V. Macpherson, J.; A. Beeston, M.; R. Unwin, P. Imaging Local Mass-Transfer Rates within an Impinging Jet and Studies of Fast Heterogeneous Electron-Transfer Kinetics Using the Microjet Electrode. *J. Chem. Soc. Faraday Trans.* **1995**, *91*, 899–904.

(54) Macpherson, J. V.; Simjee, N.; Unwin, P. R. Hydrodynamic Ultramicroelectrodes: Kinetic and Analytical Applications. *Electrochimica Acta* **2001**, *47*, 29–45.

(55) Bitziou, E.; Rudd, N. C.; Edwards, M. A.; Unwin, P. R. Visualization and Modeling of the Hydrodynamics of an Impinging Microjet. *Anal. Chem.* **2006**, *78*, 1435–1443.

(56) Subbaraman, R.; Tripkovic, D.; Strmcnik, D.; Chang, K.-C.; Uchimura, M.; Paulikas, A. P.; Stamenkovic, V.; Markovic, N. M. Enhancing Hydrogen Evolution Activity in Water Splitting by Tailoring Li^+-$Ni(OH)_2$-Pt Interfaces. *Science* **2011**, *334*, 1256–1260.

(57) Danilovic, N.; Subbaraman, R.; Strmcnik, D.; Chang, K.-C.; Paulikas, A. P.; Stamenkovic, V. R.; Markovic, N. M. Enhancing the Alkaline Hydrogen Evolution Reaction Activity through the Bifunctionality of $Ni(OH)_2$ /Metal Catalysts. *Angew. Chem.* **2012**, *124*, 12663–12666.

(58) Chen, Z.; Duan, X.; Wei, W.; Wang, S.; Ni, B.-J. Recent Advances in Transition Metal-Based Electrocatalysts for Alkaline Hydrogen Evolution. *J. Mater. Chem. A* **2019**, *7*, 14971–15005.

(59) Zhu, Y.; Lin, Q.; Zhong, Y.; Tahini, H. A.; Shao, Z.; Wang, H. Metal Oxide-Based Materials as an Emerging Family of Hydrogen Evolution Electrocatalysts. *Energy Environ. Sci.* **2020**, *13*, 3361–3392.

(60) Wu, H.; Zhu, T.; Lu, X.; Wei Ho, G. High-Efficient Electrocatalysts by Unconventional Acid-Etching for Overall Water Splitting. *J. Mater. Chem. A* **2017**, *5*, 24153–24158.

(61) Xie, L.; Ren, X.; Liu, Q.; Cui, G.; Ge, R.; M. Asiri, A.; Sun, X.; Zhang, Q.; Chen, L. A $Ni(OH)_2$ –PtO_2 Hybrid Nanosheet Array with Ultralow Pt Loading toward Efficient and Durable Alkaline Hydrogen Evolution. *J. Mater. Chem. A* **2018**, *6*, 1967–1970.

(62) Liu, Q.; Yan, Z.; Gao, J.; Wang, E.; Sun, G. Optimizing Platinum Location on Nickel Hydroxide Nanosheets to Accelerate the Hydrogen Evolution Reaction. *ACS Appl. Mater. Interfaces* **2020**, *12*, 24683–24692.

(63) Wang, L.; Lin, C.; Huang, D.; Chen, J.; Jiang, L.; Wang, M.; Chi, L.; Shi, L.; Jin, J. Optimizing the Volmer Step by Single-Layer Nickel Hydroxide Nanosheets in Hydrogen Evolution Reaction of Platinum. *ACS Catal.* **2015**, *5*, 3801–3806.

(64) Yu, X.; Zhao, J.; Zheng, L.-R.; Tong, Y.; Zhang, M.; Xu, G.; Li, C.; Ma, J.; Shi, G. Hydrogen Evolution Reaction in Alkaline Media: Alpha- or Beta-Nickel Hydroxide on the Surface of Platinum? *ACS Energy Lett.* **2018**, *3*, 237–244.

(65) Wang, G.; Parrondo, J.; He, C.; Li, Y.; Ramani, V. Pt/C/Ni(OH)2 Bi-Functional Electrocatalyst for Enhanced Hydrogen Evolution Reaction Activity under Alkaline Conditions. *J. Electrochem. Soc.* **2017**, *164*, F1307.

(66) E, S. P.; Liu, D.; Lazenby, R. A.; Sloan, J.; Vidotti, M.; Unwin, P. R.; Macpherson, J. V. Electrodeposition of Nickel Hydroxide Nanoparticles on Carbon Nanotube Electrodes: Correlation of Particle Crystallography with Electrocatalytic Properties. *J. Phys. Chem. C* **2016**, *120*, 16059–16068.

(67) Tucceri, R. An Electrochemical Study of the Nickel Hydroxide-Gold Modified Electrode Employing the Surface Resistance Technique. *J. Electroanal. Chem.* **2016**, *774*, 95–101.

4.6 SCHEMES AND FIGURES

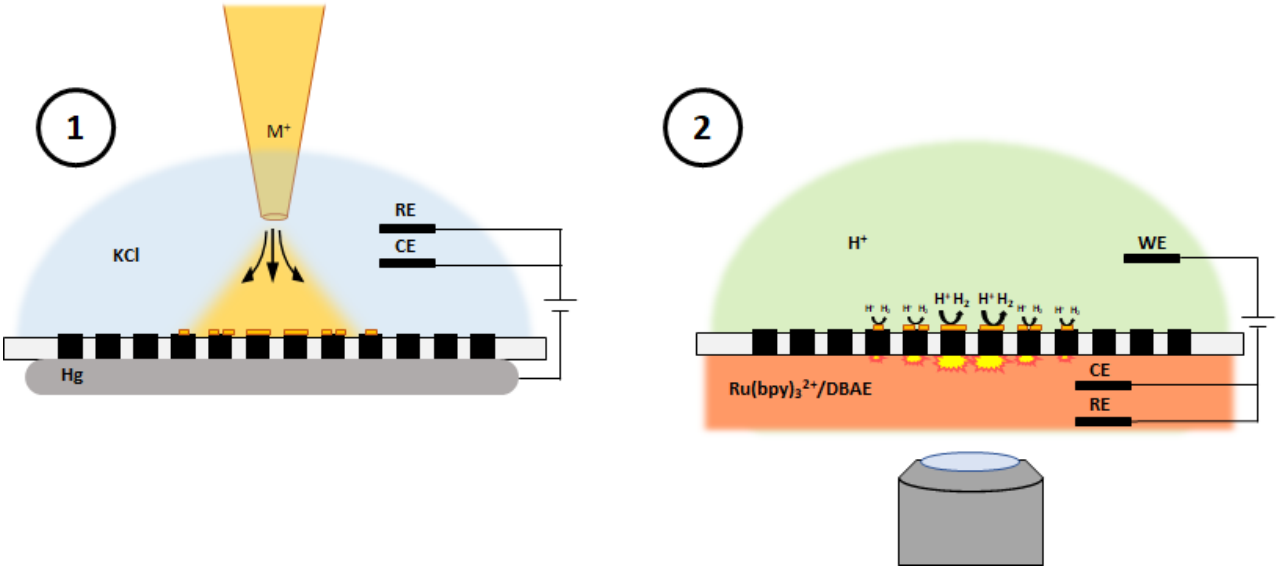

Scheme 4.1. Diagram of gradient electrodeposition process (step 1) and highly parallelized HER electrocatalyst screening via coupling to ECL using a BPE array (step 2).

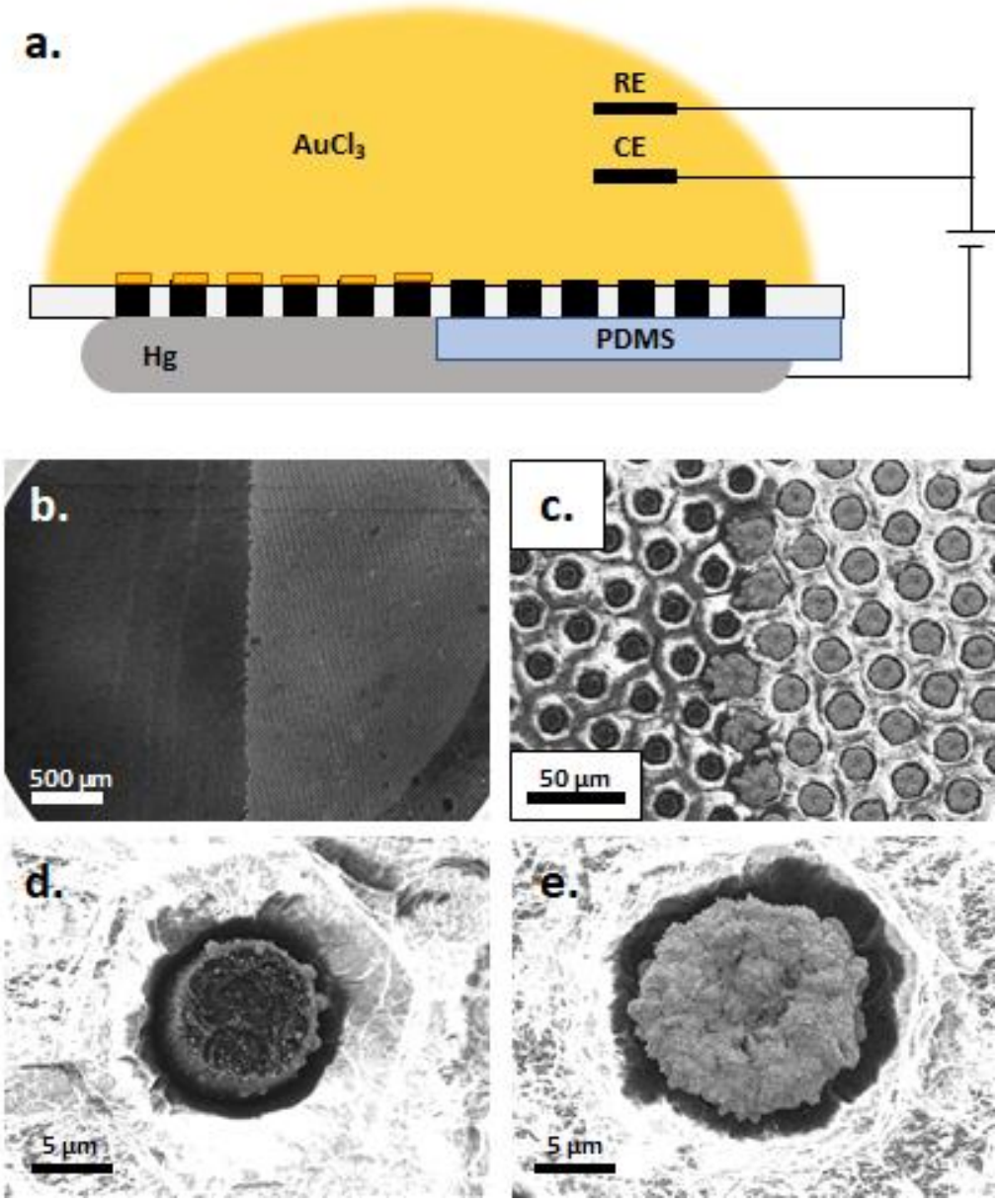

Figure 4.1. (a) Diagram of selective electrodeposition technique. (b) SEM image of an Au deposition which was carried out using 50 mM $AuCl_3$ for 2 min at 1.5 mA over half of a bipolar carbon UME array. (c) Zoomed SEM image of the boundary between the Au-modified and unmodified regions of the same array. Representative images of (d) a bare carbon electrode and (e) an Au-modified electrode.

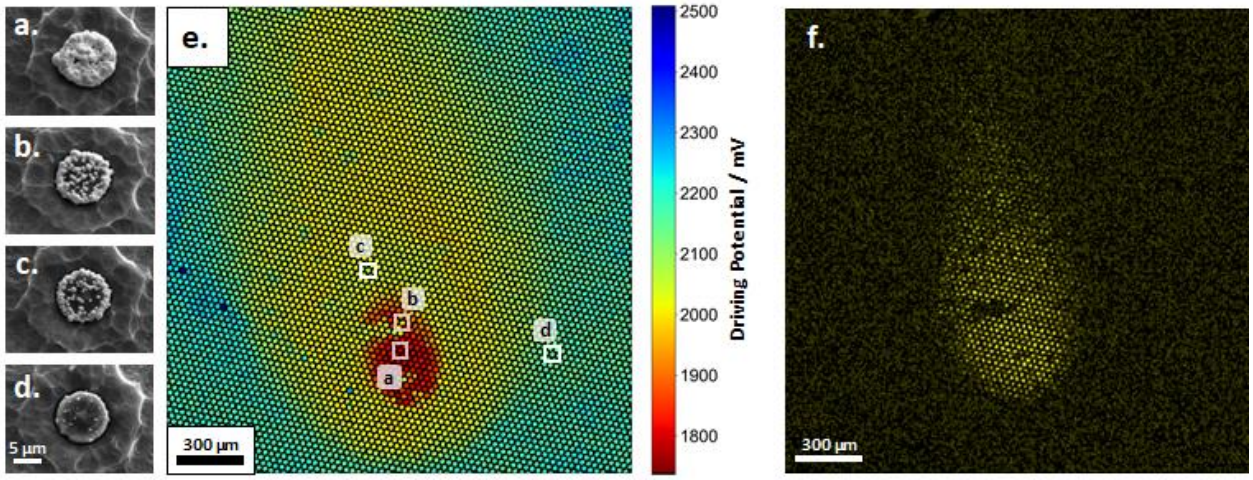

Figure 4.2. (a-d) SEM images of selected electrodes from the Pt gradient deposition site. (e) False color plot of HER onset driving potentials of the Pt gradient deposition site in 100 mM $HClO_4$ 100 mM NaCl coupled to anodic ECL with SEM-imaged electrodes labeled. (f) EDS map of Pt across gradient deposition site.

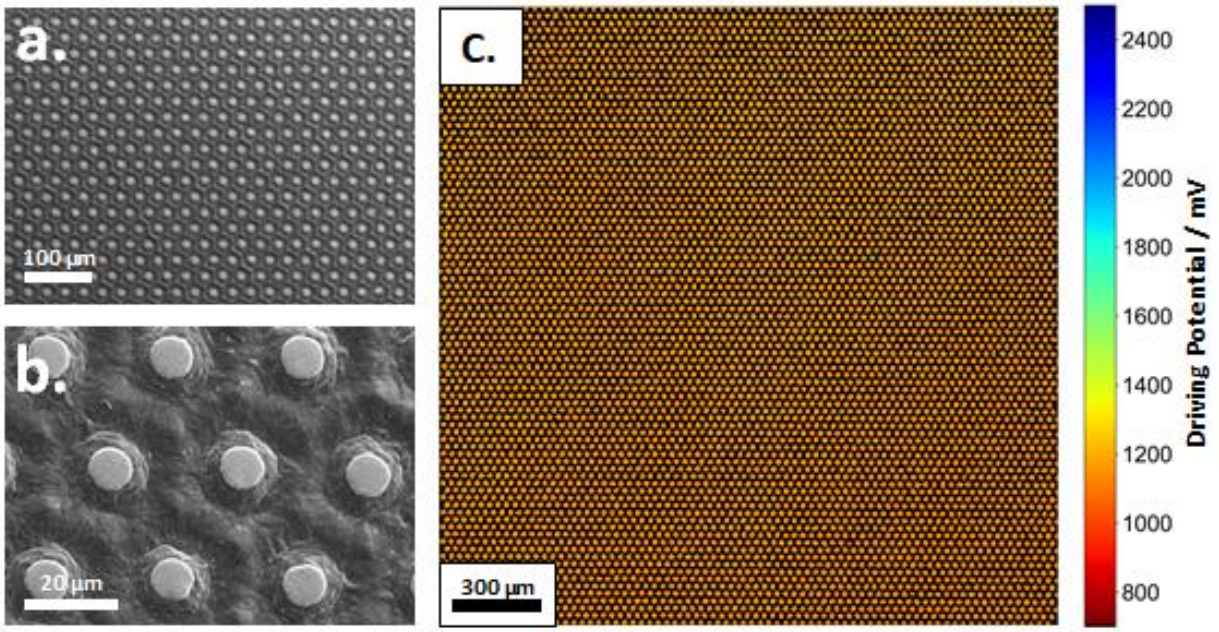

Figure 4.3. (a,b) SEM images of Au-coated bipolar UME array. (c) False color plot of HER onset driving potentials of an Au-coated bipolar UME array in 100 mM $HClO_4$ 100 mM NaCl coupled to anodic ECL.

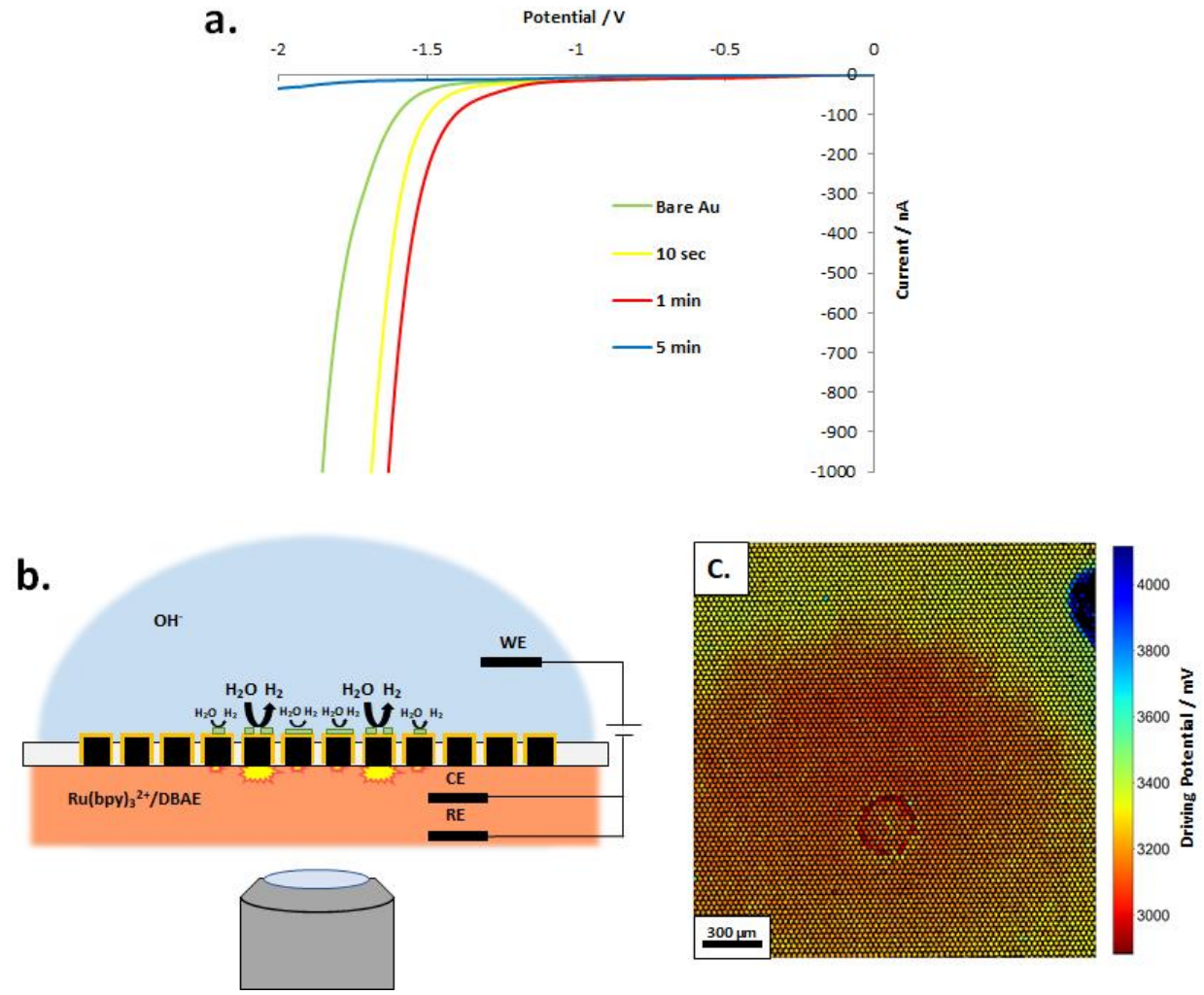

Figure 4.4. (a) Linear sweep voltammograms for a 25 µm Au UME with varying immersion times in 1 M $NiCl_2$ 100 mM NaCl pH 3.6. (b) Diagram of a screening experiment with a gradient of $Ni(OH)_2$ on an Au-coated bipolar UME array. (c) False color plot of HER onset driving potentials of a $Ni(OH)_2$-modified Au-coated bipolar UME array in 100 mM KOH 100 coupled to anodic ECL.

Chapter 5

NOVEL MICROFABRICATED GLASS FREESTANDING MEMBRANE CHIPS FOR LOW-NOISE NANOPORE SUBSTRATES

5.1 INTRODUCTION

Resistive-pulse measurements have been widely utilized in the detection and analysis of single entities ranging from nanoparticles[1] to biomolecules.[2,3] In this electrochemical sensing scheme (referred to as a Coulter counter),[4] an electric field is applied across a nanopore separating two segregated buffer solutions to induce the flow of ionic current through the pore. When a particle or macromolecule is drawn into the pore as a result of Brownian motion, pressure, electroosmosis, or electrophoresis, the movement of ions within the constriction is obstructed and a transient decrease in electrical current for the system is observed. The magnitude and duration of such resistive pulses are governed by the cross-sectional area of the particle relative to the pore and the time taken for the particle taken to traverse the pore's length (the translocation time), respectively, and can be used to determine the particle size in addition to other properties such as zeta potential and electrophoretic mobility.[1]

One of the most widely targeted applications of this technique has been the sequencing of single-stranded deoxyribonucleic acid (DNA) via detection of the characteristic resistive pulses exhibited by the individual nucleotide bases during translocation.[5] Biological nanopores comprised of transport proteins embedded in lipid bilayers have been used to achieve single base pair sequencing resolution by utilizing enzyme racheting to unzip and slow the translocation rate of DNA[6]; this scheme has since been extended to very long reads including bacterial[7] and human[8] genomes. Despite exhibiting a number of advantages over their biological counterparts (such as improved signal[9] and greater control over pore size, geometry, and thickness), solid-

state nanopores in inorganic membranes[10] have seen comparatively less advancement as sequencing platforms due to the extremely fast translocation rate of freerunning DNA (~20,000 nucleotides/ms)[9] which necessitates bandwidths of more than 20 Mhz to achieve single nucleotide resolution. At present, two studies have managed to detect single nucleotide bases with atomically thin MoS_2 nanopores, but in both cases the translocation rate was slowed by either a viscosity gradient[11] or increased charge interaction between the nucleotides or DNA oligos and the pore.[12] This reduction in translocation rate is undesirable due to the associated decrease in sequencing throughput. Increasing the speed of measurement is therefore critical to the further development of solid-state nanopores as DNA sequencing platforms.

However, the elevated noise associated with high bandwidths can render the current signals of single nucleotides impossible to resolve. Above a bandwidth of 10 kHz the major contribution to noise is interaction between the voltage noise of the current amplifier and the capacitance of the nanopore chip, where the root-mean-squared input referred current noise (I_{rms}) is given by **Equation 5.1** below,[9]

$$I_{rms}(B) = \left(\frac{2\pi}{\sqrt{3}}\right) B^{\frac{3}{2}}\left(C_{chip} + C_w + C_{amp}\right)\nu_n \qquad (5.1)$$

in which B is the bandwidth, C_{chip} is the chip capacitance, C_w is the capacitance of the wiring between the amplifier and the chip, C_{amp} is the capacitance of the amplifier, and ν_n is the input-referred voltage noise of the amplifier. Thus, noise levels may be lessened by reducing the chip capacitance as much as possible. Several studies have reported accomplishing this by applying a thick layer of insulator such as polydimethylsiloxane (PDMS),[13,14] polyimide,[15] low pressure chemical vapor deposited (LPCVD) SiN_x/SiO_2, or bonded glass slides[9] to the chip surface, but manual handling or patterning during this step greatly extends fabrication time and prevents such approaches from being scaled up to mass production. Alternatively, glass chips may be utilized

in place of traditional Si substrates to completely eliminate the capacitance associated with the semiconductor/membrane interface. The fabrication of such devices has been carried out by transferring SiN_x membranes to glass chips,[16,17] although the necessity for manual handling precludes wafer-scale fabrication according to this scheme. Other studies have described the use of the previously deposited membrane material as a stop layer for HF etching of the underlying glass[18,19] or sapphire,[20] but thereby introduce the possibility of pitting or thinning of the membrane material due to poor etch selectivity.

To address these issues, a novel wafer-scale fabrication scheme for free-standing SiN_x membranes was devised in which the membranes are formed by plasma enhanced chemical vapor deposition (PECVD) onto a sacrificial Si surface without any intervening transfer or etching steps (see **Scheme 5.1**), thereby enabling the scalable production of a low-capacitance platform for nanopore measurements which is free of semiconductor/insulator interfaces and exhibits excellent control over membrane thickness.

5.2 Experimental Section

5.2.1 *Glass Etching*

A 500 µm thick Si wafer (Silicon Valley Microelectronics) was anodically bonded to a 500 µm thick Borofloat 33 glass wafer (Schott AG) using an EVG 501 Wafer Bonding System using a voltage of -500 V at 350°C and 2.5×10^{-3} mbar for 10 min, after which 10 nm of Cr and 200 nm of Au was sputtered over the exposed glass surface with an Evatec EVO Sputter System. After adhesion promotion in a HMDS oven , a 4 µm film of AZ 10XT photoresist (Microchemicals) was then spun over the metalized surface and softbaked for 3 min at 110°C. Exposure was performed on a semi-automatic mask aligner (ABM) with a custom Mylar photomask (CAD/Art Services) using an exposure dose of 400 mJ/cm^2 at 400 nm. The exposed resist film was

developed in 1:4 AZ400K:DIW for 4 min then rinsed in DI water and spun dry using an Avenger Ultra-Pure spin-rinse-dryer (Class One Technology). The bonded wafer pair was then descummed using a Vision 320 RIE Mk II reactive ion etcher before being sequentially immersed in Cr 1020 etchant (Transene) and Au Etch TFA (Transene) until the exposed metal observed to be removed from the patterned regions of the surface and then rinsed in DI water. Through-etching of the exposed glass was carried out via immersion in 49% HF for 95 minutes at room temperature without agitation. The substrate was held vertically in a Teflon wafer carrier throughout the process to maintain etch uniformity. After etch completion, the wafer pair was thoroughly rinsed with DI water and spun dry.

5.2.2 *Membrane Formation*

A layer of SiN_x between 200 nm and 1 µm was deposited over the through-etched glass surface at 125°C and 0.56 nm/s using a SPTS PECVD system, after which the Si backing of the wafer pair was thinned to ~70 µm using a Strasbaugh 7AA-SP wafer grinder. Dicing lanes were then patterned into an AZ 10XT film spun onto the SiN_x surface using the aforementioned parameters before the wafer was diced into chips using a Disco DAD321 dicing saw. The Si backing of the individual chips was further thinned to ~1 µm via dry etching with a SPTS Rapier Si deep reactive ion etcher (DRIE) and finally removed via immersion in 35% KOH solution for 1-4 min.

5.2.3 *Focused Ion Beam Milling*

The free-standing SiN_x membrane chips were coated with ~100 nm of carbon using a SPI Modular Sputter and Carbon Coater before being milled using the ion beam of an Oxford Instruments X-Max Dual Beam FIB-SEM at 80000x magnification and a beam current of 10 pA (sample imaging was carried out using this same system). The milling endpoint was detected by

the abrupt change in intensity of the backscattered electron signal which occurred upon full penetration of the membrane. Removal of the carbon film was carried out via O_2 plasma etching in a Diener Femto Low-Pressure Plasma system for 30 min at 40 W and 15 mbar.

5.3 Results and Discussion

To enable fabrication of the freestanding membrane chips, a series of apertures were first formed through a Borofloat 33 glass wafer to provide a framework for the suspended membranes. HF etching was selected for the aperture formation method due to its high etch rate for borosilicate glass[21] relative to dry etching techniques and hemispherical etch profile which would result in a reduced substrate thickness about the membrane and consequently lower stray capacitance.[18] Initially, masking of the glass surface was carried out with PECVD amorphous silicon (a-Si), but despite the excellent resistance of this material to HF attack, its high internal stress and poor adhesion to the glass wafer resulted in partial delamination about the etched regions of the wafer (see **Figure D1**). This adhesion issue was resolved by the substitution of a 200 nm Au film on a 10 nm Cr adhesion layer for the a-Si. The 4 µm AZ 10XT photoresist film which was used to pattern holes in the metal mask layers was also left in place to minimize pinholing of the glass due to HF permeation of defects in the hydrophilic Au surface.[22,23] Concentrated 49% HF was also utilized to maximize the glass etch rate and minimize the HF exposure time of the mask layer. Backside protection of the glass substrate during etching was accomplished via anodic bonding to a Si wafer with matching coefficient of thermal expansion (CTE) to the Borofloat 33. Note that exposure of the smooth Si surface at the bottom of the through-etched holes serving as an indicator of the endpoint of the etch (see **Figure 5.1a**). This wet etching scheme yielded minimal pinholing of the glass surface (see **Figure 5.1b**) and enabled many chips to be simultaneously etched across a single wafer (see **Figure 5.1c**).

Formation of the membranes was accomplished by deposition of a layer of 0.2-1 μm of PECVD SiN_x over the etched glass surface after removal of the photoresist/Au/Cr mask; the stress of the film was minimized by maintaining a low temperature (125°C) and deposition rate during the process (0.56 nm/s). Note that the exposed smooth Si at the bottom of each through-hole served as a sacrificial substrate for conformal SiN_x growth during deposition (see **Scheme 5.1**) and also protected the integrity of the resulting membranes from the water jet and mechanical vibrations of the subsequent dicing process. This strategy of membrane deposition after the glass etching process provides excellent control over the membrane thickness as a result of the slow deposition rate and allows complete through-etching of the glass wafer to be carried out in a single step. Other glass etching schemes which utilize the membrane material as a stop layer rely on additional wet etching steps,[18] pretreatment via laser exposure,[19] or deposition of a second membrane layer,[20] thereby further complicating the fabrication process.

Removal of the Si backing was initially carried out via dissolution in hot 35% KOH solution immediately after dicing the bonded wafer pair. However, poor Si/glass etch selectivity and the length of time required for complete dissolution (>3 hr) resulted in overetching and extensive pitting of the chip surfaces (see **Figure D2**). Consequently, a wafer grinder was used to mechanically remove ~85% of the backing (see **Figure 5.2a**), after which the remaining thickness was further reduced via DRIE until a state of optical transparency was reached, as evidenced by the visibility of the HF-etched holes through the back of the chip shown in **Figure 5.2c**. The residual Si was then rapidly dissolved in 35% KOH solution, thereby greatly reducing the exposure time of the glass to the etchant and yielding much smoother chip surfaces (see **Figure 5.3b**).

Figure 5.3a shows an example of two finished devices, each containing 16 freestanding SiN_x membranes to enable parallel recording from multiple nanopore data channels, with an example membrane displayed in **Figure 5.3b**. Note than the area of the membrane may be controlled to a certain degree by altering the size of the holes patterned in the HF etching mask (the membrane in **Figure 5.3b** corresponds to a 300 μm mask hole). The freestanding nature of the membranes was verified by using a scanning electron microscope (SEM) equipped with a focused ion beam (FIB) to mill a 5 μm × 5 μm square hole through the center of a membrane and image its cross-section (see **Figure 5.3c**), the thickness of which was found to be in good agreement with the value targeted during deposition (200 nm). FIB milling was also used to drill a 170 nm nanopore in a 200 nm thick membrane to demonstrate the viability of these devices as nanopore substrates (see **Figure 5.3d**). However, while FIB-milled pores of such dimensions are well-suited to nanoparticle translocation measurements,[24] other methods for pore formation such as dielectric breakdown[25] or transmission electron microscopy (TEM) drilling[26] are capable of creating pores on the single-nanometer scale and are currently being explored in our group as a means of creating smaller pores within these devices. Additionally, due to the fact that the potential drop across the nanopore during a resistive pulse experiment occurs linearly along its length,[1] thinning of the deposited membranes via FIB[27–29] or reactive ion etching (RIE)[30] is also being investigated to further reduce the size of the sensing zone and enhance the electric field at the pore.

5.4 CONCLUSIONS

Herein we have presented a novel fabrication scheme for thin, freestanding SiN_x membranes supported on glass chips in which an anodically bonded Si wafer is used for the dual purpose of backside protection during HF through-etching of the glass support and as a sacrificial substrate

for direct deposition of the membrane material via PECVD, thereby eliminating the necessity of any transfer steps. While the focus of this unpublished work is centered on microfabrication processes rather than experimental applications, studies are currently underway to utilize these devices for open bipolar coupling of reactions across translocating metal nanoparticles[31] with the aim of creating a platform for Janus particle synthesis. Additionally, further improvements to the fabrication scheme are being explored to enable mass production of devices utilizing 2D membrane materials (*e.g.*, graphene[32–34]) without any intervening exfoliation/transfer steps.

5.5 REFERENCES

(1) Luo, L.; German, S. R.; Lan, W.-J.; Holden, D. A.; Mega, T. L.; White, H. S. Resistive-Pulse Analysis of Nanoparticles. *Annu. Rev. Anal. Chem.* **2014**, *7*, 513–535.

(2) Harrer, S.; Kim, S. C.; Schieber, C.; Kannam, S.; Gunn, N.; Moore, S.; Scott, D.; Bathgate, R.; Skafidas, S.; Wagner, J. M. Label-Free Screening of Single Biomolecules through Resistive Pulse Sensing Technology for Precision Medicine Applications. *Nanotechnology* **2015**, *26*, 182502.

(3) Hu, Z.-L.; Huo, M.-Z.; Ying, Y.-L.; Long, Y.-T. Biological Nanopore Approach for Single-Molecule Protein Sequencing. *Angew. Chem.* **2021**, *133*, 14862–14873.

(4) Coulter, W. H. Means for Counting Particles Suspended in a Fluid. US2656508A, October 20, 1953.

(5) Haque, F.; Li, J.; Wu, H.-C.; Liang, X.-J.; Guo, P. Solid-State and Biological Nanopore for Real-Time Sensing of Single Chemical and Sequencing of DNA. *Nano Today* **2013**, *8*, 56–74.

(6) Manrao, E. A.; Derrington, I. M.; Laszlo, A. H.; Langford, K. W.; Hopper, M. K.; Gillgren, N.; Pavlenok, M.; Niederweis, M.; Gundlach, J. H. Reading DNA at Single-Nucleotide Resolution with a Mutant MspA Nanopore and Phi29 DNA Polymerase. *Nat. Biotechnol.* **2012**, *30*, 349–353.

(7) Loman, N. J.; Quick, J.; Simpson, J. T. A Complete Bacterial Genome Assembled de Novo Using Only Nanopore Sequencing Data. *Nat. Methods* **2015**, *12*, 733–735.

(8) Jain, M.; Koren, S.; Miga, K. H.; Quick, J.; Rand, A. C.; Sasani, T. A.; Tyson, J. R.; Beggs, A. D.; Dilthey, A. T.; Fiddes, I. T.; Malla, S.; Marriott, H.; Nieto, T.; O'Grady, J.; Olsen, H. E.; Pedersen, B. S.; Rhie, A.; Richardson, H.; Quinlan, A. R.; Snutch, T. P.; Tee, L.; Paten,

B.; Phillippy, A. M.; Simpson, J. T.; Loman, N. J.; Loose, M. Nanopore Sequencing and Assembly of a Human Genome with Ultra-Long Reads. *Nat. Biotechnol.* **2018**, *36*, 338–345.

(9) Balan, A.; Machielse, B.; Niedzwiecki, D.; Lin, J.; Ong, P.; Engelke, R.; Shepard, K. L.; Drndić, M. Improving Signal-to-Noise Performance for DNA Translocation in Solid-State Nanopores at MHz Bandwidths. *Nano Lett.* **2014**, *14*, 7215–7220.

(10) Xue, L.; Yamazaki, H.; Ren, R.; Wanunu, M.; Ivanov, A. P.; Edel, J. B. Solid-State Nanopore Sensors. *Nat. Rev. Mater.* **2020**, *5*, 931–951.

(11) Feng, J.; Liu, K.; Bulushev, R. D.; Khlybov, S.; Dumcenco, D.; Kis, A.; Radenovic, A. Identification of Single Nucleotides in MoS2 Nanopores. *Nat. Nanotechnol.* **2015**, *10*, 1070–1076.

(12) Sen, P.; Gupta, M. Single Nucleotide Detection Using Bilayer MoS_2 Nanopores with High Efficiency. *RSC Adv.* **2021**, *11*, 6114–6123.

(13) Tabard-Cossa, V.; Trivedi, D.; Wiggin, M.; Jetha, N. N.; Marziali, A. Noise Analysis and Reduction in Solid-State Nanopores. *Nanotechnology* **2007**, *18*, 305505.

(14) Rosenstein, J. K.; Wanunu, M.; Merchant, C. A.; Drndic, M.; Shepard, K. L. Integrated Nanopore Sensing Platform with Sub-Microsecond Temporal Resolution. *Nat. Methods* **2012**, *9*, 487–492.

(15) Dimitrov, V.; Mirsaidov, U.; Wang, D.; Sorsch, T.; Mansfield, W.; Miner, J.; Klemens, F.; Cirelli, R.; Yemenicioglu, S.; Timp, G. Nanopores in Solid-State Membranes Engineered for Single Molecule Detection. *Nanotechnology* **2010**, *21*, 065502.

(16) Pitchford, W. H.; Kim, H.-J.; Ivanov, A. P.; Kim, H.-M.; Yu, J.-S.; Leatherbarrow, R. J.; Albrecht, T.; Kim, K.-B.; Edel, J. B. Synchronized Optical and Electronic Detection of Biomolecules Using a Low Noise Nanopore Platform. *ACS Nano* **2015**, *9*, 1740–1748.

(17) Lee, M.-H.; Kumar, A.; Park, K.-B.; Cho, S.-Y.; Kim, H.-M.; Lim, M.-C.; Kim, Y.-R.; Kim, K.-B. A Low-Noise Solid-State Nanopore Platform Based on a Highly Insulating Substrate. *Sci. Rep.* **2015**, *4*, 7448.

(18) Balan, A.; Chien, C.-C.; Engelke, R.; Drndić, M. Suspended Solid-State Membranes on Glass Chips with Sub 1-PF Capacitance for Biomolecule Sensing Applications. *Sci. Rep.* **2016**, *5*, 17775.

(19) de Vreede, L. J.; Ying, C.; Houghtaling, J.; Figueiredo Da Silva, J.; Hall, A. R.; Lovera, A.; Mayer, M. Wafer-Scale Fabrication of Fused Silica Chips for Low-Noise Recording of Resistive Pulses through Nanopores. *Nanotechnology* **2019**, *30*, 265301.

(20) Xia, P.; Zuo, J.; Paudel, P.; Choi, S.; Chen, X.; Rahman Laskar, M. A.; Bai, J.; Song, W.; Im, J.; Wang, C. Sapphire-Supported Nanopores for Low-Noise DNA Sensing. *Biosens. Bioelectron.* **2021**, *174*, 112829.

(21) Iliescu, C.; Chen, B.; Miao, J. On the Wet Etching of Pyrex Glass. *Sens. Actuators Phys.* **2008**, *143*, 154–161.

(22) Tay, F. E. H.; Iliescu, C.; Jing, J.; Miao, J. Defect-Free Wet Etching through Pyrex Glass Using Cr/Au Mask. *Microsyst. Technol.* **2006**, *12*, 935–939.

(23) Jin, J.-Y.; Yoo, S.; Bae, J.-S.; Kim, Y.-K. Deep Wet Etching of Borosilicate Glass and Fused Silica with Dehydrated AZ4330 and a Cr/Au Mask. *J. Micromechanics Microengineering* **2014**, *24*, 015003.

(24) Gunderson, C. G.; Barlow, S. T.; Zhang, B. FIB-Milled Quartz Nanopores in a Sealed Nanopipette. *J. Electroanal. Chem.* **2019**, *833*, 181–188.

(25) Kwok, H.; Briggs, K.; Tabard-Cossa, V. Nanopore Fabrication by Controlled Dielectric Breakdown. *PLoS ONE* **2014**, *9*, e92880.

(26) Wu, M.-Y.; Krapf, D.; Zandbergen, M.; Zandbergen, H.; Batson, P. E. Formation of Nanopores in a SiN⁄SiO2 Membrane with an Electron Beam. *Appl. Phys. Lett.* **2005**, *87*, 113106.

(27) Li, J.; Stein, D.; McMullan, C.; Branton, D.; Aziz, M. J.; Golovchenko, J. A. Ion-Beam Sculpting at Nanometre Length Scales. *Nature* **2001**, *412*, 166–169.

(28) Sawafta, F.; Carlsen, A.; Hall, A. Membrane Thickness Dependence of Nanopore Formation with a Focused Helium Ion Beam. *Sensors* **2014**, *14*, 8150–8161.

(29) Rodríguez-Manzo, J. A.; Puster, M.; Nicolaï, A.; Meunier, V.; Drndić, M. DNA Translocation in Nanometer Thick Silicon Nanopores. *ACS Nano* **2015**, *9*, 6555–6564.

(30) Wanunu, M.; Dadosh, T.; Ray, V.; Jin, J.; McReynolds, L.; Drndić, M. Rapid Electronic Detection of Probe-Specific MicroRNAs Using Thin Nanopore Sensors. *Nat. Nanotechnol.* **2010**, *5*, 807–814.

(31) Han, C.; Hao, R.; Fan, Y.; Edwards, M. A.; Gao, H.; Zhang, B. Observing Transient Bipolar Electrochemical Coupling on Single Nanoparticles Translocating through a Nanopore. *Langmuir* **2019**, *35*, 7180–7190.

(32) Merchant, C. A.; Healy, K.; Wanunu, M.; Ray, V.; Peterman, N.; Bartel, J.; Fischbein, M. D.; Venta, K.; Luo, Z.; Johnson, A. T. C.; Drndić, M. DNA Translocation through Graphene Nanopores. *Nano Lett.* **2010**, *10*, 2915–2921.

(33) Schneider, G. F.; Kowalczyk, S. W.; Calado, V. E.; Pandraud, G.; Zandbergen, H. W.; Vandersypen, L. M. K.; Dekker, C. DNA Translocation through Graphene Nanopores. *Nano Lett.* **2010**, *10*, 3163–3167.

(34) Zhang, X.; van Deursen, P. M. G.; Fu, W.; Schneider, G. F. Facile and Ultraclean Graphene-on-Glass Nanopores by Controlled Electrochemical Etching. *ACS Sens.* **2020**, *5*, 2317–2325.

5.6 SCHEMES AND FIGURES

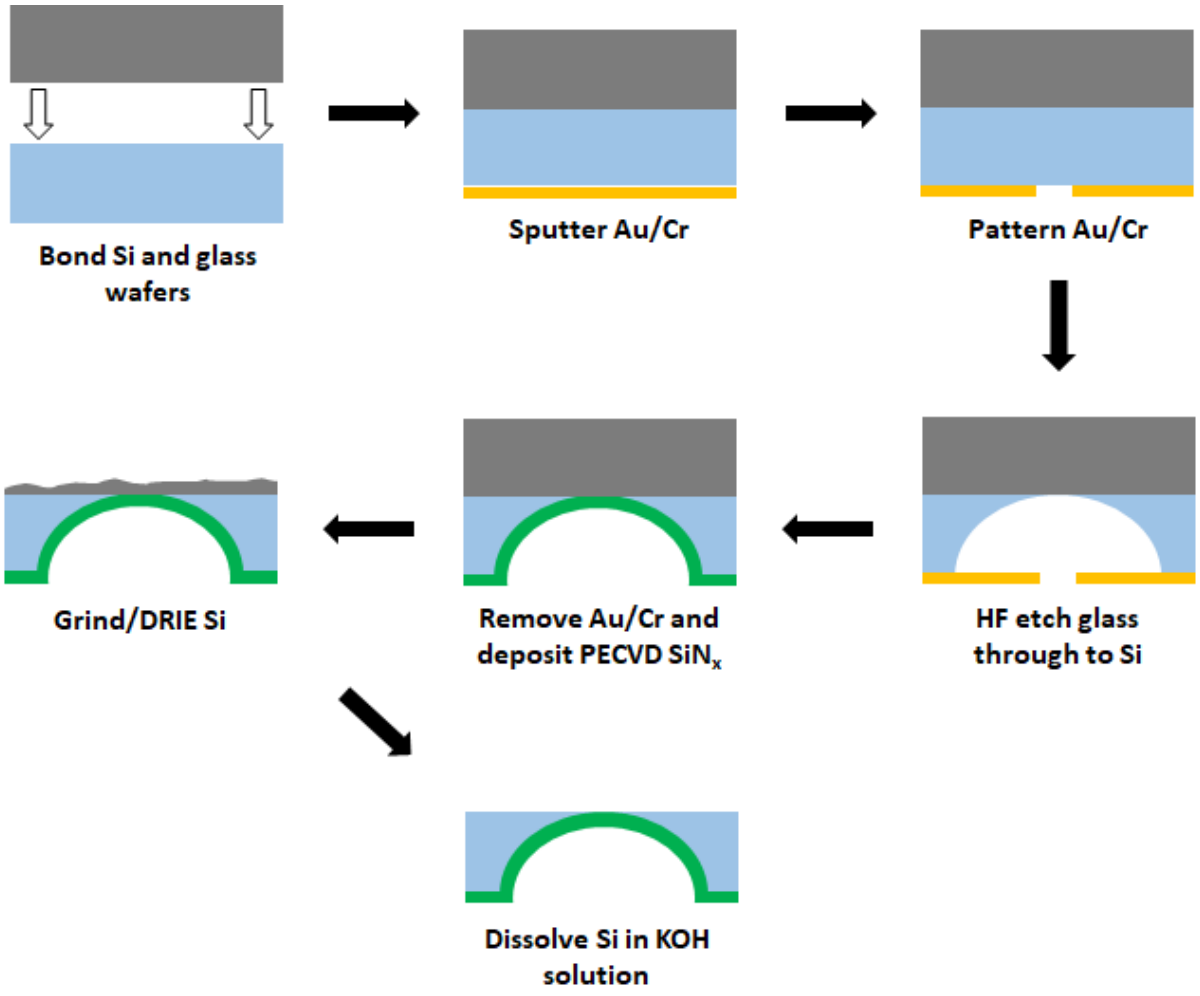

Scheme 5.1. Flowchart of glass freestanding membrane chip fabrication scheme.

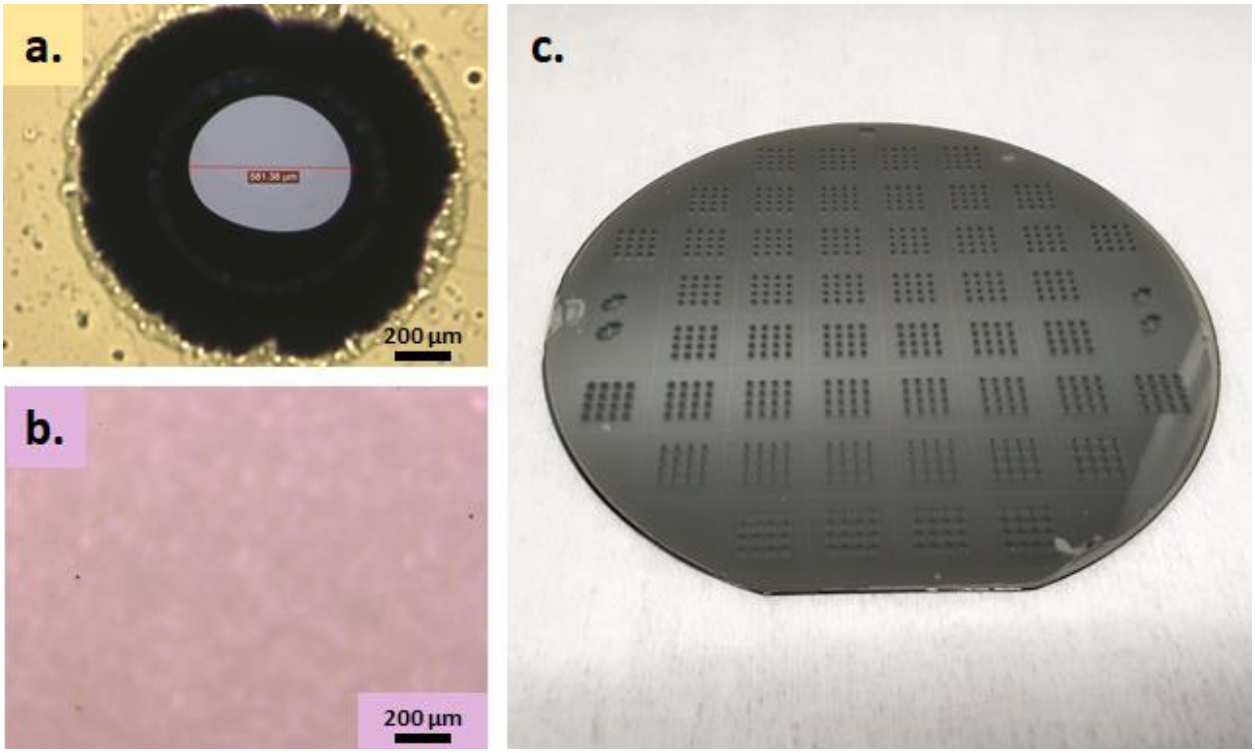

Figure 5.1. (a) Optical microscope image of through-etched glass pore after 95 min in 49% HF prior to removal of Au/Cr mask. (b) Optical microscope image of glass surface after removal of Au/Cr mask. (c) Photograph of entire HF-etched wafer (36 dies) after removal of Au mask and subsequent SiN_x deposition.

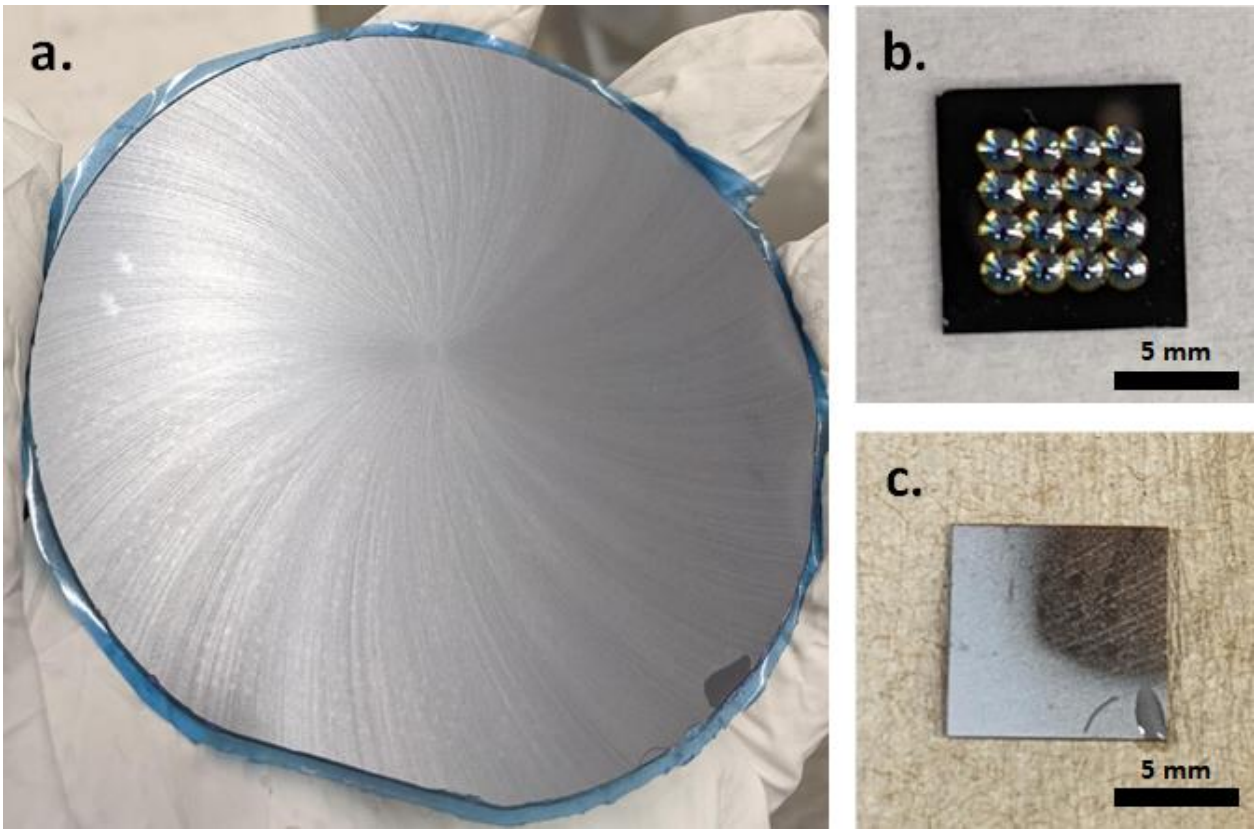

Figure 5.2. (a) Photograph of Si surface after thinning to ~75 µm via wafer grinder. (b) Photograph of etched glass surface of a single chip. (c) Photograph of Si chip backing after DRIE thinning.

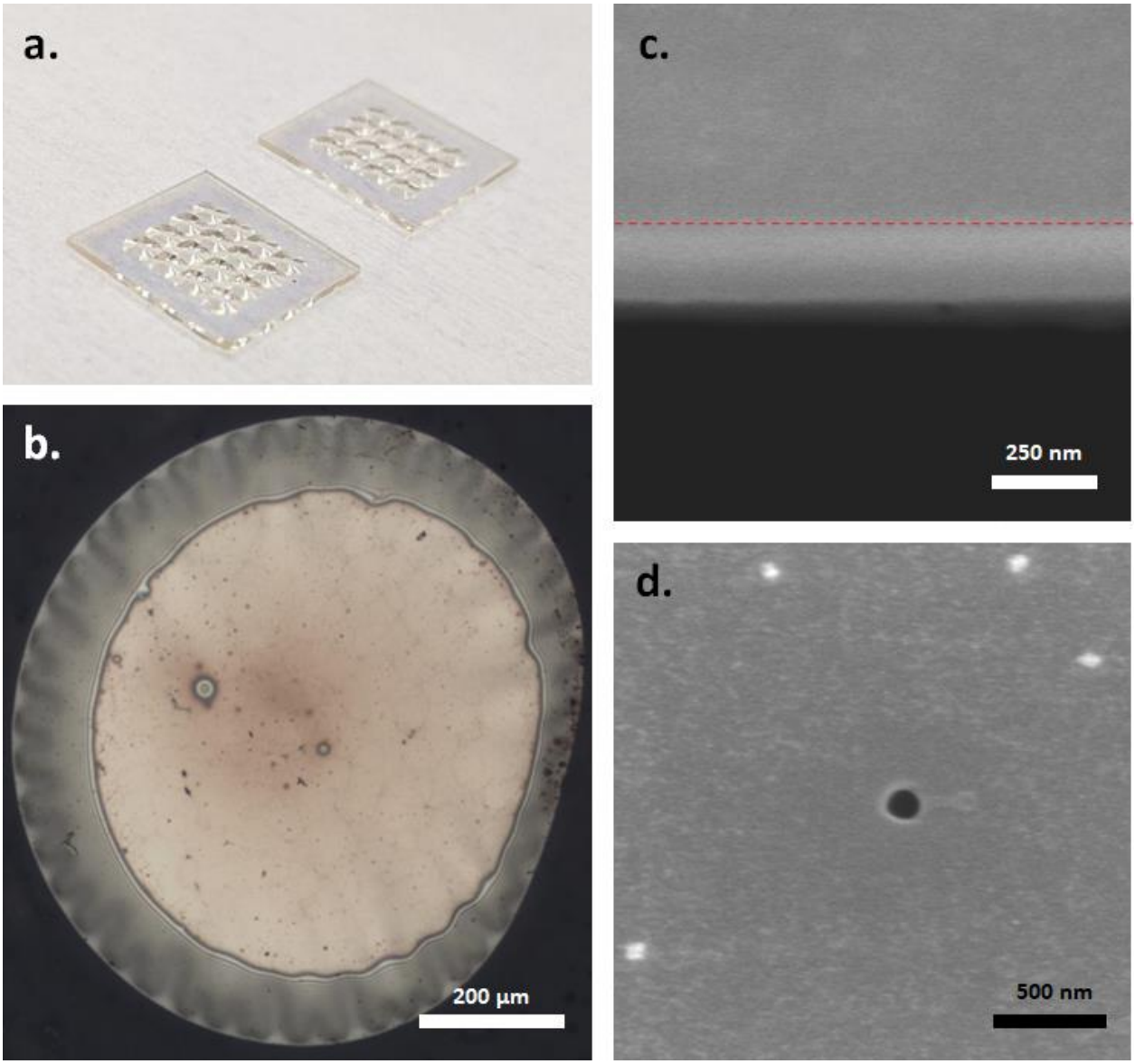

Figure 5.3. (a) Photograph of two completed glass freestanding membrane chips. (b) Transmission microscopy image of a freestanding SiN_x membrane surface. (c) SEM micrograph of a membrane cross-section imaged at a 45° angle from the surface. (d) SEM micrograph of a nanopore milled via FIB in a 200 nm thick freestanding SiN_x membrane.

BIBLIOGRAPHY

Amemiya, S.; Bard, A. J.; Fan, F.-R. F.; Mirkin, M. V.; Unwin, P. R. Scanning Electrochemical Microscopy. *Ann. Rev. Anal. Chem.* **2008**, *1*, 95–131.

Anderson, T. J.; Defnet, P. A.; Zhang, B. Electrochemiluminescence (ECL)-Based Electrochemical Imaging Using a Massive Array of Bipolar Ultramicroelectrodes. *Anal. Chem.* **2020**, *92*, 6748–6755.

Antolini, E. Evaluation of the Optimum Composition of Low-Temperature Fuel Cell Electrocatalysts for Methanol Oxidation by Combinatorial Screening. *ACS Comb. Sci.* **2017**, *19*, 47–54.

Arora, A.; Eijkel, J. C. T.; Morf, W. E.; Manz, A. A Wireless Electrochemiluminescence Detector Applied to Direct and Indirect Detection for Electrophoresis on a Microfabricated Glass Device. *Anal. Chem.* **2001**, *73*, 3282–3288.

Balan, A.; Chien, C.-C.; Engelke, R.; Drndić, M. Suspended Solid-State Membranes on Glass Chips with Sub 1-PF Capacitance for Biomolecule Sensing Applications. *Sci. Rep.* **2016**, *5*, 17775.

Balan, A.; Machielse, B.; Niedzwiecki, D.; Lin, J.; Ong, P.; Engelke, R.; Shepard, K. L.; Drndić, M. Improving Signal-to-Noise Performance for DNA Translocation in Solid-State Nanopores at MHz Bandwidths. *Nano Lett.* **2014**, *14*, 7215–7220.

Bentley, C. L.; Kang, M.; Unwin, P. R. Scanning Electrochemical Cell Microscopy: New Perspectives on Electrode Processes in Action. *Curr. Opin. Electrochem.* **2017**, *6*, 23–30.

Bitziou, E.; Rudd, N. C.; Edwards, M. A.; Unwin, P. R. Visualization and Modeling of the Hydrodynamics of an Impinging Microjet. *Anal. Chem.* **2006**, *78*, 1435–1443.

Brace, K. M.; Hayden, B. E.; Russell, A. E.; Owen, J. R. A Parallel Optical Screen for the Rapid Combinatorial Electrochromic Analysis of Electrochemical Materials. *Adv. Mater.* **2006**, *18*, 3253–3257.

Chen, C.-C.; Zhou, Y.; Baker, L. A. Scanning Ion Conductance Microscopy. *Ann. Rev. Anal. Chem.* **2012**, *5*, 207–228.

Chen, Y.; Zhao, D.; Fu, J.; Gou, X.; Jiang, D.; Dong, H.; Zhu, J.-J. *In Situ* Imaging Facet-Induced Spatial Heterogeneity of Electrocatalytic Reaction Activity at the Subparticle Level via Electrochemiluminescence Microscopy. *Anal. Chem.* **2019**, acs.analchem.9b01044.

Chen, Z.; Duan, X.; Wei, W.; Wang, S.; Ni, B.-J. Recent Advances in Transition Metal-Based Electrocatalysts for Alkaline Hydrogen Evolution. *J. Mater. Chem. A* **2019**, *7*, 14971–15005.

Chou, Y.-C.; Masih Das, P.; Monos, D. S.; Drndić, M. Lifetime and Stability of Silicon Nitride Nanopores and Nanopore Arrays for Ionic Measurements. *ACS Nano* **2020**, *14*, 6715–6728.

Chow, K.-F.; Chang, B.-Y.; Zaccheo, B. A.; Mavré, F.; Crooks, R. M. A Sensing Platform Based on Electrodissolution of a Ag Bipolar Electrode. *J. Am. Chem. Soc.* **2010**, *132*, 9228–9229.

Chow, K.-F.; Mavré, F.; Crooks, J. A.; Chang, B.-Y.; Crooks, R. M. A Large-Scale, Wireless Electrochemical Bipolar Electrode Microarray. *J. Am. Chem. Soc.* **2009**, *131*, 8364–8365.

Chow, K.-F.; Mavré, F.; Crooks, R. M. Wireless Electrochemical DNA Microarray Sensor. *J. Am. Chem. Soc.* **2008**, *130*, 7544–7545.

Conzuelo, F.; Schulte, A.; Schuhmann, W. Biological Imaging with Scanning Electrochemical Microscopy. *Proc. R. Soc. A* **2018**, *474*, 20180409.

Coulter, W. H. Means for Counting Particles Suspended in a Fluid. US2656508A, October 20, 1953.

Cox, J. T.; Guerrette, J. P.; Zhang, B. Steady-State Voltammetry of a Microelectrode in a Closed Bipolar Cell. *Anal. Chem.* **2012**, *84*, 8797-8804.

Cui, C.; Jin, R.; Jiang, D.; Zhang, J.; Zhu, J.-J. Electrogenerated Chemiluminescence in Submicrometer Wells for Very High-Density Biosensing. *Anal. Chem.* **2020**, *92*, 578–582.

Dang, T.; Ramsaran, R.; Roy, S.; Froehlich, J.; Wang, J.; Kubiak, C. P. Design of a High Throughput 25-Well Parallel Electrolyzer for the Accelerated Discovery of CO2 Reduction Catalysts via a Combinatorial Approach. *Electroanalysis* **2011**, *23*, 2335–2342.

Danilovic, N.; Subbaraman, R.; Strmcnik, D.; Chang, K.-C.; Paulikas, A. P.; Stamenkovic, V. R.; Markovic, N. M. Enhancing the Alkaline Hydrogen Evolution Reaction Activity through the Bifunctionality of Ni(OH) $_2$ /Metal Catalysts. *Angew. Chem.* **2012**, *124*, 12663–12666.

de Vreede, L. J.; Ying, C.; Houghtaling, J.; Figueiredo Da Silva, J.; Hall, A. R.; Lovera, A.; Mayer, M. Wafer-Scale Fabrication of Fused Silica Chips for Low-Noise Recording of Resistive Pulses through Nanopores. *Nanotechnology* **2019**, *30*, 265301.

Defnet, P. A.; Anderson, T. J.; Zhang, B. Stochastic Collision Electrochemistry of Single Silver Nanoparticles. *Curr. Opin. Electrochem.* **2020**, *22*, 129–135.

Defnet, P. A.; Han, C.; Zhang, B. Temporally-Resolved Ultrafast Hydrogen Adsorption and Evolution on Single Platinum Nanoparticles. *Anal. Chem.* **2019**, *91*, 4023–4030.

Defnet, P. A.; Zhang, B. Detection of Transient Nanoparticle Collision Events Using Electrochemiluminescence on a Closed Bipolar Microelectrode. *ChemElectroChem* **2020**, *7*, 252–259.

Dimitrov, V.; Mirsaidov, U.; Wang, D.; Sorsch, T.; Mansfield, W.; Miner, J.; Klemens, F.; Cirelli, R.; Yemenicioglu, S.; Timp, G. Nanopores in Solid-State Membranes Engineered for Single Molecule Detection. *Nanotechnology* **2010**, *21*, 065502.

Dragas, J.; Viswam, V.; Shadmani, A.; Chen, Y.; Bounik, R.; Stettler, A.; Radivojevic, M.; Geissler, S.; Obien, M. E. J.; Müller, J.; Hierlemann, A. In Vitro Multi-Functional Microelectrode Array Featuring 59 760 Electrodes, 2048 Electrophysiology Channels, Stimulation,

Impedance Measurement, and Neurotransmitter Detection Channels. *IEEE J. Solid-State Circuits* **2017**, *52*, 1576–1590.

Du, K.; Wathuthanthri, I.; Mao, W.; Xu, W.; Choi, C.-H. Large-Area Pattern Transfer of Metallic Nanostructures on Glass Substrates via Interference Lithography. *Nanotechnology* **2011**, *22*, 285306.

E, S. P.; Liu, D.; Lazenby, R. A.; Sloan, J.; Vidotti, M.; Unwin, P. R.; Macpherson, J. V. Electrodeposition of Nickel Hydroxide Nanoparticles on Carbon Nanotube Electrodes: Correlation of Particle Crystallography with Electrocatalytic Properties. *J. Phys. Chem. C* **2016**, *120*, 16059–16068.

Ebejer, N.; Schnippering, M.; Colburn, A. W.; Edwards, M. A.; Unwin, P. R. Localized High Resolution Electrochemistry and Multifunctional Imaging: Scanning Electrochemical Cell Microscopy. *Anal. Chem.* **2010**, *82*, 9141–9145.

Fan, Y.; Anderson, T. J.; Zhang, B. Single-Molecule Electrochemistry: From Redox Cycling to Single Redox Events. *Curr. Opin. in Electrochem.* **2018**, *7*, 81–86.

Feng, J.; Liu, K.; Bulushev, R. D.; Khlybov, S.; Dumcenco, D.; Kis, A.; Radenovic, A. Identification of Single Nucleotides in MoS2 Nanopores. *Nat. Nanotechnol.* **2015**, *10*, 1070–1076.

Fernández, J. L.; Walsh, D. A.; Bard, A. J. Thermodynamic Guidelines for the Design of Bimetallic Catalysts for Oxygen Electroreduction and Rapid Screening by Scanning Electrochemical Microscopy. M−Co (M: Pd, Ag, Au). *J. Am. Chem. Soc.* **2005**, *127*, 357–365.

Fernández, J. L.; White, J. M.; Sun, Y.; Tang, W.; Henkelman, G.; Bard, A. J. Characterization and Theory of Electrocatalysts Based on Scanning Electrochemical Microscopy Screening Methods. *Langmuir* **2006**, *22*, 10426–10431.

Fosdick, S. E.; Berglund, S. P.; Mullins, C. B.; Crooks, R. M. Evaluating Electrocatalysts for the Hydrogen Evolution Reaction Using Bipolar Electrode Arrays: Bi- and Trimetallic Combinations of Co, Fe, Ni, Mo, and W. *ACS Catal.* **2014**, *4*, 1332–1339.

Fosdick, S. E.; Berglund, S. P.; Mullins, C. B.; Crooks, R. M. Parallel Screening of Electrocatalyst Candidates Using Bipolar Electrochemistry. *Anal. Chem.* **2013**, *85*, 2493–2499.

Fosdick, S. E.; Crooks, R. M. Bipolar Electrodes for Rapid Screening of Electrocatalysts. *J. Am. Chem. Soc.* **2012**, *134*, 863–866.

Fosdick, S. E.; Knust, K. N.; Scida, K.; Crooks, R. M. Bipolar Electrochemistry. *Angew. Chem. Int. Ed.* **2013**, *52*, 10438–10456.

Fuladpanjeh-Hojaghan, B.; Elsutohy, M. M.; Kabanov, V.; Heyne, B.; Trifkovic, M.; Roberts, E. P. L. In-Operando Mapping of PH Distribution in Electrochemical Processes. *Angew. Chem.* **2019**, *131*, 16971–16975.

Gamler, J. T. L.; Ashberry, H. M.; Skrabalak, S. E.; Koczkur, K. M. Random Alloyed versus Intermetallic Nanoparticles: A Comparison of Electrocatalytic Performance. *Adv. Mater.* **2018**, *30*, 1801563.

Gisbert Quilis, N.; Lequeux, M.; Venugopalan, P.; Khan, I.; Knoll, W.; Boujday, S.; Lamy de la Chapelle, M.; Dostalek, J. Tunable Laser Interference Lithography Preparation of Plasmonic Nanoparticle Arrays Tailored for SERS. *Nanoscale* **2018**, *10*, 10268–10276.

Grant, A. W.; Hu, Q.-H.; Kasemo, B. Transmission Electron Microscopy Windows for Nanofabricated Structures. *Nanotechnology* **2004**, *15*, 1175–1181.

Guerin, S.; Hayden, B. E. Physical Vapor Deposition Method for the High-Throughput Synthesis of Solid-State Material Libraries. *J. Comb. Chem.* **2006**, *8*, 66–73.

Guerin, S.; Hayden, B. E.; Lee, C. E.; Mormiche, C.; Owen, J. R.; Russell, A. E.; Theobald, B.; Thompsett, D. Combinatorial Electrochemical Screening of Fuel Cell Electrocatalysts. *J. Comb. Chem.* **2004**, *6*, 149–158.

Guerin, S.; Hayden, B. E.; Lee, C. E.; Mormiche, C.; Russell, A. E. High-Throughput Synthesis and Screening of Ternary Metal Alloys for Electrocatalysis. *J. Phys. Chem. B* **2006**, *110*, 14355–14362.

Guerrette, J. P.; Oja, S. M.; Zhang, B. Coupled Electrochemical Reactions at Bipolar Microelectrodes and Nanoelectrodes. *Anal. Chem.* **2012**, *84*, 1609–1616.

Guerrette, J. P.; Percival, S. J.; Zhang, B. Fluorescence Coupling for Direct Imaging of Electrocatalytic Heterogeneity. *J. Am. Chem. Soc.* **2013**, *135*, 855–861.

Guille-Collignon, M.; Lemaître, F. Recent Developments Concerning the Investigation of Exocytosis with Amperometry. *Curr. Opin. Electrochem.* **2021**, *29*, 100751.

Gunderson, C. G.; Barlow, S. T.; Zhang, B. FIB-Milled Quartz Nanopores in a Sealed Nanopipette. *J. Electroanal. Chem.* **2019**, *833*, 181–188.

Han, C.; Hao, R.; Fan, Y.; Edwards, M. A.; Gao, H.; Zhang, B. Observing Transient Bipolar Electrochemical Coupling on Single Nanoparticles Translocating through a Nanopore. *Langmuir* **2019**, *35*, 7180–7190.

Hao, R.; Peng, Z.; Zhang, B. Single-Molecule Fluorescence Microscopy for Probing the Electrochemical Interface. *ACS Omega* **2020**, *5*, 89–97.

Haque, F.; Li, J.; Wu, H.-C.; Liang, X.-J.; Guo, P. Solid-State and Biological Nanopore for Real-Time Sensing of Single Chemical and Sequencing of DNA. *Nano Today* **2013**, *8*, 56–74.

Harrer, S.; Kim, S. C.; Schieber, C.; Kannam, S.; Gunn, N.; Moore, S.; Scott, D.; Bathgate, R.; Skafidas, S.; Wagner, J. M. Label-Free Screening of Single Biomolecules through Resistive

Pulse Sensing Technology for Precision Medicine Applications. *Nanotechnology* **2015**, *26*, 182502.

Hu, Z.-L.; Huo, M.-Z.; Ying, Y.-L.; Long, Y.-T. Biological Nanopore Approach for Single-Molecule Protein Sequencing. *Angew. Chem.* **2021**, *133*, 14862–14873.

Iliescu, C.; Chen, B.; Miao, J. On the Wet Etching of Pyrex Glass. *Sens. Actuators Phys.* **2008**, *143*, 154–161.

Ino, K.; Yaegaki, R.; Hiramoto, K.; Nashimoto, Y.; Shiku, H. Closed Bipolar Electrode Array for On-Chip Analysis of Cellular Respiration by Cell Aggregates. *ACS Sens.* **2020**, *5*, 740–745.

Iwama, T.; Inoue, K. Y.; Abe, H.; Matsue, T. Chemical Imaging Using a Closed Bipolar Electrode Array. *Chem. Lett.* **2018**, *47*, 843–845.

Jain, M.; Koren, S.; Miga, K. H.; Quick, J.; Rand, A. C.; Sasani, T. A.; Tyson, J. R.; Beggs, A. D.; Dilthey, A. T.; Fiddes, I. T.; Malla, S.; Marriott, H.; Nieto, T.; O'Grady, J.; Olsen, H. E.; Pedersen, B. S.; Rhie, A.; Richardson, H.; Quinlan, A. R.; Snutch, T. P.; Tee, L.; Paten, B.; Phillippy, A. M.; Simpson, J. T.; Loman, N. J.; Loose, M. Nanopore Sequencing and Assembly of a Human Genome with Ultra-Long Reads. *Nat. Biotechnol.* **2018**, *36*, 338–345.

Jaramillo, T. F.; Ivanovskaya, A.; McFarland, E. W. High-Throughput Screening System for Catalytic Hydrogen-Producing Materials. *J. Comb. Chem.* **2002**, *4*, 17–22.

Jayaraman, S.; Hillier, A. C. Screening the Reactivity of $Pt_x Ru_y$ and $Pt_x Ru_y Mo_z$ Catalysts toward the Hydrogen Oxidation Reaction with the Scanning Electrochemical Microscope. *J. Phys. Chem. B* **2003**, *107*, 5221–5230.

Jeon, M. K.; Lee, C. H.; Park, G. I.; Kang, K. H. Combinatorial Search for Oxygen Reduction Reaction Electrocatalysts: A Review. *J. Power Sources* **2012**, *216*, 400–408.

Jin, J.-Y.; Yoo, S.; Bae, J.-S.; Kim, Y.-K. Deep Wet Etching of Borosilicate Glass and Fused Silica with Dehydrated AZ4330 and a Cr/Au Mask. *J. Micromechanics Microengineering* **2014**, *24*, 015003.

Jung, C.; Sánchez-Sánchez, C. M.; Lin, C.-L.; Rodríguez-López, J.; Bard, A. J. Electrocatalytic Activity of Pd−Co Bimetallic Mixtures for Formic Acid Oxidation Studied by Scanning Electrochemical Microscopy. *Anal. Chem.* **2009**, *81*, 7003–7008.

Jung, Y. H.; Qiu, Y.; Lee, S.; Shih, T.-Y.; Xu, Y.; Xu, R.; Lee, J.; Schendel, A. A.; Lin, W.; Williams, J. C.; Behdad, N.; Ma, Z. A Compact Parylene-Coated WLAN Flexible Antenna for Implantable Electronics. *IEEE Antennas and Wireless Prop. Lett.* **2016**, *15*, 1382–1385.

Kim, D.-S.; Kang, E.-S.; Baek, S.; Choo, S.-S.; Chung, Y.-H.; Lee, D.; Min, J.; Kim, T.-H. Electrochemical Detection of Dopamine Using Periodic Cylindrical Gold Nanoelectrode Arrays. *Sci. Rep.* **2018**, *8*, 14049.

Kim, T.-H.; Yea, C.-H.; Chueng, S.-T. D.; Yin, P. T.-T.; Conley, B.; Dardir, K.; Pak, Y.; Jung, G. Y.; Choi, J.-W.; Lee, K.-B. Large-Scale Nanoelectrode Arrays to Monitor the Dopaminergic Differentiation of Human Neural Stem Cells. *Adv. Mater.* **2015**, *27*, 6356–6362.

Kwok, H.; Briggs, K.; Tabard-Cossa, V. Nanopore Fabrication by Controlled Dielectric Breakdown. *PLoS ONE* **2014**, *9*, e92880.

Lai, Y.; Jones, R. J. R.; Wang, Y.; Zhou, L.; Gregoire, J. M. Scanning Electrochemical Flow Cell with Online Mass Spectroscopy for Accelerated Screening of Carbon Dioxide Reduction Electrocatalysts. *ACS Comb. Sci.* **2019**, *21*, 692–704.

Lan, W.-J.; Holden, D. A.; Zhang, B.; White, H. S. Nanoparticle Transport in Conical-Shaped Nanopores. *Anal. Chem.* **2011**, *83*, 3840–3847.

Latyshev, V.; Vorobiov, S.; Shylenko, O.; Komanicky, V. Fabrication of Combinatorial Material Libraries by Flow Cell Electrodeposition Technique. *Mater. Lett.* **2020**, *281*, 128594.

Latyshev, V.; Vorobiov, S.; Shylenko, O.; Komanicky, V. Screening of Electrocatalysts for Hydrogen Evolution Reaction Using Bipolar Electrodes Fabricated by Composition Gradient Magnetron Sputtering. *J. Electroanal. Chem.* **2019**, *854*, 113562.

Lee, J.-H.; Choi, H. K.; Yang, L.; Chueng, S.-T. D.; Choi, J.-W.; Lee, K.-B. Nondestructive Real-Time Monitoring of Enhanced Stem Cell Differentiation Using a Graphene-Au Hybrid Nanoelectrode Array. *Adv. Mater.* **2018**, *30*, 1802762.

Lee, K. R.; Jeon, M. K.; Woo, S. I. Composition Optimization of PtRuM/C (M=Fe and Mo) Catalysts for Methanol Electro-Oxidation via Combinatorial Method. *Appl. Catal. B Environ.* **2009**, *91*, 428–433.

Lee, K. R.; Jung, Y.; Woo, S. I. Combinatorial Screening of Highly Active Pd Binary Catalysts for Electrochemical Oxygen Reduction. *ACS Comb. Sci.* **2012**, *14*, 10–16.

Lee, M.-H.; Kumar, A.; Park, K.-B.; Cho, S.-Y.; Kim, H.-M.; Lim, M.-C.; Kim, Y.-R.; Kim, K.-B. A Low-Noise Solid-State Nanopore Platform Based on a Highly Insulating Substrate. *Sci. Rep.* **2015**, *4*, 7448.

Lenne, Q.; Leroux, Y. R.; Lagrost, C. Surface Modification for Promoting Durable, Efficient, and Selective Electrocatalysts. *ChemElectroChem* **2020**, *7*, 2345–2363.

Li, J.; Stein, D.; McMullan, C.; Branton, D.; Aziz, M. J.; Golovchenko, J. A. Ion-Beam Sculpting at Nanometre Length Scales. *Nature* **2001**, *412*, 166–169.

Li, W.; Fan, F.-R. F.; Bard, A. J. The Application of Scanning Electrochemical Microscopy to the Discovery of Pd–W Electrocatalysts for the Oxygen Reduction Reaction That Demonstrate

High Activity, Stability, and Methanol Tolerance. *J. Solid State Electrochem.* **2012**, *16*, 2563–2568.

Li, W.; Rodger, D. C.; Meng, E.; Weiland, J. D.; Humayun, M. S.; Tai, Y.-C. Wafer-Level Parylene Packaging with Integrated RF Electronics for Wireless Retinal Prostheses. *J. Microelectromech. Sys.* **2010**, *19*, 735–742.

Liang, Y.; Pfisterer, J. H. K.; McLaughlin, D.; Csoklich, C.; Seidl, L.; Bandarenka, A. S.; Schneider, O. Electrochemical Scanning Probe Microscopies in Electrocatalysis. *Small Methods* **2019**, *3*, 1800387.

Lin, T.-E.; Rapino, S.; Girault, H. H.; Lesch, A. Electrochemical Imaging of Cells and Tissues. *Chem. Sci.* **2018**, *9*, 4546–4554.

Lin, X.; Zheng, L.; Gao, G.; Chi, Y.; Chen, G. Electrochemiluminescence Imaging-Based High-Throughput Screening Platform for Electrocatalysts Used in Fuel Cells. *Anal. Chem.* **2012**, *84*, 7700–7707.

Lin, X.; Zheng, L.; Gao, G.; Chi, Y.; Chen, G. Electrochemiluminescence Imaging-Based High-Throughput Screening Platform for Electrocatalysts Used in Fuel Cells. *Anal. Chem.* **2012**, *84*, 7700–7707.

Liu, Q.; Yan, Z.; Gao, J.; Wang, E.; Sun, G. Optimizing Platinum Location on Nickel Hydroxide Nanosheets to Accelerate the Hydrogen Evolution Reaction. *ACS Appl. Mater. Interfaces* **2020**, *12*, 24683–24692.

Liu, X.; Tong, Y.; Fang, P.-P. Recent Development in Amperometric Measurements of Vesicular Exocytosis. *TrAC Trends Anal. Chem.* **2019**, *113*, 13–24.

Loman, N. J.; Quick, J.; Simpson, J. T. A Complete Bacterial Genome Assembled de Novo Using Only Nanopore Sequencing Data. *Nat. Methods* **2015**, *12*, 733–735.

Lu, C.; Lipson, R. H. Interference Lithography: A Powerful Tool for Fabricating Periodic Structures: Interference Lithography. *Laser Photonics Rev.* **2010**, *4*, 568–580.

Luo, L.; German, S. R.; Lan, W.-J.; Holden, D. A.; Mega, T. L.; White, H. S. Resistive-Pulse Analysis of Nanoparticles. *Annu. Rev. Anal. Chem.* **2014**, *7*, 513–535.

Macpherson, J. V.; A. Beeston, M.; R. Unwin, P. Imaging Local Mass-Transfer Rates within an Impinging Jet and Studies of Fast Heterogeneous Electron-Transfer Kinetics Using the Microjet Electrode. *J. Chem. Soc. Faraday Trans.* **1995**, *91*, 899–904.

Macpherson, J. V.; Simjee, N.; Unwin, P. R. Hydrodynamic Ultramicroelectrodes: Kinetic and Analytical Applications. *Electrochimica Acta* **2001**, *47*, 29–45.

Manrao, E. A.; Derrington, I. M.; Laszlo, A. H.; Langford, K. W.; Hopper, M. K.; Gillgren, N.; Pavlenok, M.; Niederweis, M.; Gundlach, J. H. Reading DNA at Single-Nucleotide Resolution with a Mutant MspA Nanopore and Phi29 DNA Polymerase. *Nat. Biotechnol.* **2012**, *30*, 349–353.

Mao, X.; Liu, C.; Hesari, M.; Zou, N.; Chen, P. Super-Resolution Imaging of Non-Fluorescent Reactions via Competition. *Nat. Chem.* **2019**, *11*, 687–694.

Mavré, F.; Anand, R. K.; Laws, D. R.; Chow, K.-F.; Chang, B.-Y.; Crooks, J. A.; Crooks, R. M. Bipolar Electrodes: A Useful Tool for Concentration, Separation, and Detection of Analytes in Microelectrochemical Systems. *Anal. Chem.* **2010**, *82*, 8766–8774.

Mavré, F.; Chow, K.-F.; Sheridan, E.; Chang, B.-Y.; Crooks, J. A.; Crooks, R. M. A Theoretical and Experimental Framework for Understanding Electrogenerated Chemiluminescence (ECL) Emission at Bipolar Electrodes. *Anal. Chem.* **2009**, *81*, 6218–6225.

Merchant, C. A.; Healy, K.; Wanunu, M.; Ray, V.; Peterman, N.; Bartel, J.; Fischbein, M. D.; Venta, K.; Luo, Z.; Johnson, A. T. C.; Drndić, M. DNA Translocation through Graphene Nanopores. *Nano Lett.* **2010**, *10*, 2915–2921.

Minguzzi, A.; Alpuche-Aviles, M. A.; López, J. R.; Rondinini, S.; Bard, A. J. Screening of Oxygen Evolution Electrocatalysts by Scanning Electrochemical Microscopy Using a Shielded Tip Approach. *Anal. Chem.* **2008**, *80*, 4055–4064.

Minguzzi, A.; Battistel, D.; Rodríguez-López, J.; Vertova, A.; Rondinini, S.; Bard, A. J.; Daniele, S. Rapid Characterization of Oxygen-Evolving Electrocatalyst Spot Arrays by the Substrate Generation/Tip Collection Mode of Scanning Electrochemical Microscopy with Decreased O_2 Diffusion Layer Overlap. *J. Phys. Chem. C* **2015**, *119*, 2941–2947.

Morkved, T. L.; Lopes, W. A.; Hahm, J.; Sibener, S. J.; Jaeger, H. M. Silicon Nitride Membrane Substrates for the Investigation of Local Structure in Polymer Thin Films. *Polymer* **1998**, *39*, 3871–3875.

Ng, W. W.; Hong, C.-S.; Yariv, A. Holographic Interference Lithography for Integrated Optics. *IEEE Trans. Electron Devices* **1978**, *25*, 1193–1200.

Oh, Y.; Lim, J. W.; Kim, J. G.; Wang, H.; Kang, B.-H.; Park, Y. W.; Kim, H.; Jang, Y. J.; Kim, J.; Kim, D. H.; Ju, B.-K. Plasmonic Periodic Nanodot Arrays *via* Laser Interference Lithography for Organic Photovoltaic Cells with >10% Efficiency. *ACS Nano* **2016**, *10*, 10143–10151.

Oja, S. M.; Guerrette, J. P.; David, M. R.; Zhang, B. Fluorescence-Enabled Electrochemical Microscopy with Dihydroresorufin as a Fluorogenic Indicator. *Anal. Chem.* **2014**, *86*, 6040–6048.

Oja, S. M.; Zhang, B. Imaging Transient Formation of Diffusion Layers with Fluorescence-Enabled Electrochemical Microscopy. *Anal. Chem.* **2014**, *86*, 12299–12307.

Peng, Y.-Y.; Qian, R.-C.; Hafez, M. E.; Long, Y.-T. Stochastic Collision Nanoelectrochemistry: A Review of Recent Developments. *ChemElectroChem* **2017**, *4*, 977–985.

Pitchford, W. H.; Kim, H.-J.; Ivanov, A. P.; Kim, H.-M.; Yu, J.-S.; Leatherbarrow, R. J.; Albrecht, T.; Kim, K.-B.; Edel, J. B. Synchronized Optical and Electronic Detection of Biomolecules Using a Low Noise Nanopore Platform. *ACS Nano* **2015**, *9*, 1740–1748.

Polcari, D.; Dauphin-Ducharme, P.; Mauzeroll, J. Scanning Electrochemical Microscopy: A Comprehensive Review of Experimental Parameters from 1989 to 2015. *Chem. Rev.* **2016**, *116*, 13234–13278.

Prochaska, M.; Jin, J.; Rochefort, D.; Zhuang, L.; DiSalvo, F. J.; Abruña, H. D.; van Dover, R. B. High Throughput Screening of Electrocatalysts for Fuel Cell Applications. *Rev. Sci. Instrum.* **2006**, *77*, 054104.

Pruchyathamkorn, J.; Yang, M.; Amin, H. M. A.; Batchelor-McAuley, C.; Compton, R. G. Imaging Electrode Heterogeneity Using Chemically Confined Fluorescence Electrochemical Microscopy. *J. Phys. Chem. Lett.* **2017**, *8*, 6124–6127.

Qi, H.; Zhang, C. Electrogenerated Chemiluminescence Biosensing. *Anal. Chem.* **2020**, *92*, 524–534.

Quilis, N. G.; Hageneder, S.; Fossati, S.; Auer, S. K.; Venugopalan, P.; Bozdogan, A.; Petri, C.; Moreno-Cencerrado, A.; Toca-Herrera, J. L.; Jonas, U.; Dostalek, J. UV-Laser Interference Lithography for Local Functionalization of Plasmonic Nanostructures with Responsive Hydrogel. *J. Phys. Chem. C* **2020**, *124*, 3297–3305.

Reddington, E. Combinatorial Electrochemistry: A Highly Parallel, Optical Screening Method for Discovery of Better Electrocatalysts. *Science* **1998**, *280*, 1735–1737.

Ring, E. A.; Peckys, D. B.; Dukes, M. J.; Baudoin, J. P.; Jonge, N. D. Silicon Nitride Windows for Electron Microscopy of Whole Cells. *J. Microsc.* **2011**, *243*, 273–283.

Rodríguez-Manzo, J. A.; Puster, M.; Nicolaï, A.; Meunier, V.; Drndić, M. DNA Translocation in Nanometer Thick Silicon Nanopores. *ACS Nano* **2015**, *9*, 6555–6564.

Rosenstein, J. K.; Wanunu, M.; Merchant, C. A.; Drndic, M.; Shepard, K. L. Integrated Nanopore Sensing Platform with Sub-Microsecond Temporal Resolution. *Nat. Methods* **2012**, *9*, 487–492.

Safizadeh, F.; Ghali, E.; Houlachi, G. Electrocatalysis Developments for Hydrogen Evolution Reaction in Alkaline Solutions – A Review. *Int. J. Hydrog. Energy* **2015**, *40*, 256–274.

Sambur, J. B.; Chen, P. Distinguishing Direct and Indirect Photoelectrocatalytic Oxidation Mechanisms Using Quantitative Single-Molecule Reaction Imaging and Photocurrent Measurements. *J. Phys. Chem. C* **2016**, *120*, 20668–20676.

Sambur, J. B.; Chen, T.-Y.; Choudhary, E.; Chen, G.; Nissen, E. J.; Thomas, E. M.; Zou, N.; Chen, P. Sub-Particle Reaction and Photocurrent Mapping to Optimize Catalyst-Modified Photoanodes. *Nature* **2016**, *530*, 77–80.

Sawafta, F.; Carlsen, A.; Hall, A. Membrane Thickness Dependence of Nanopore Formation with a Focused Helium Ion Beam. *Sensors* **2014**, *14*, 8150–8161.

Schilling, E. A.; Kamholz, A. E.; Yager, P. Cell Lysis and Protein Extraction in a Microfluidic Device with Detection by a Fluorogenic Enzyme Assay. *Anal. Chem.* **2002**, *74*, 1798–1804.

Schneider, G. F.; Kowalczyk, S. W.; Calado, V. E.; Pandraud, G.; Zandbergen, H. W.; Vandersypen, L. M. K.; Dekker, C. DNA Translocation through Graphene Nanopores. *Nano Lett.* **2010**, *10*, 3163–3167.

Schuppert, A. K.; Topalov, A. A.; Katsounaros, I.; Klemm, S. O.; Mayrhofer, K. J. J. A Scanning Flow Cell System for Fully Automated Screening of Electrocatalyst Materials. *J. Electrochem. Soc.* **2012**, *159*, F670.

Sen, P.; Gupta, M. Single Nucleotide Detection Using Bilayer MoS_2 Nanopores with High Efficiency. *RSC Adv.* **2021**, *11*, 6114–6123.

Shekar, S.; Niedzwiecki, D. J.; Chien, C.-C.; Ong, P.; Fleischer, D. A.; Lin, J.; Rosenstein, J. K.; Drndić, M.; Shepard, K. L. Measurement of DNA Translocation Dynamics in a Solid-State Nanopore at 100 Ns Temporal Resolution. *Nano Lett.* **2016**, *16*, 4483–4489.

Smotkin, E. S.; Díaz-Morales, R. R. New Electrocatalysts by Combinatorial Methods. *Annu. Rev. Mater. Res.* **2003**, *33*, 557–579.

Smotkin, E. S.; Jiang, J.; Nayar, A.; Liu, R. High-Throughput Screening of Fuel Cell Electrocatalysts. *Appl. Surf. Sci.* **2006**, *252*, 2573–2579.

Spong, A. D.; Vitins, G.; Guerin, S.; Hayden, B. E.; Russell, A. E.; Owen, J. R. Combinatorial Arrays and Parallel Screening for Positive Electrode Discovery. *J. Power Sources* **2003**, *119–121*, 778–783.

Strasser, P.; Fan, Q.; Devenney, M.; Weinberg, W. H.; Liu, P.; Nørskov, J. K. High Throughput Experimental and Theoretical Predictive Screening of Materials − A Comparative Study of Search Strategies for New Fuel Cell Anode Catalysts. *J. Phys. Chem. B* **2003**, *107*, 11013–11021.

Subbaraman, R.; Tripkovic, D.; Strmcnik, D.; Chang, K.-C.; Uchimura, M.; Paulikas, A. P.; Stamenkovic, V.; Markovic, N. M. Enhancing Hydrogen Evolution Activity in Water Splitting by Tailoring Li^+-$Ni(OH)_2$-Pt Interfaces. *Science* **2011**, *334*, 1256–1260.

Sullivan, M. G.; Utomo, H.; Fagan, P. J.; Ward, M. D. Automated Electrochemical Analysis with Combinatorial Electrode Arrays. *Anal. Chem.* **1999**, *71*, 4369–4375.

Tabard-Cossa, V.; Trivedi, D.; Wiggin, M.; Jetha, N. N.; Marziali, A. Noise Analysis and Reduction in Solid-State Nanopores. *Nanotechnology* **2007**, *18*, 305505.

Takahashi, Y.; Kobayashi, Y.; Wang, Z.; Ito, Y.; Ota, M.; Ida, H.; Kumatani, A.; Miyazawa, K.; Fujita, T.; Shiku, H.; Korchev, Y. E.; Miyata, Y.; Fukuma, T.; Chen, M.; Matsue, T. High-Resolution Electrochemical Mapping of the Hydrogen Evolution Reaction on Transition-Metal Dichalcogenide Nanosheets. *Angew. Chem. Int. Ed.* **2020,** *59*, 3601–3608.

Takahashi, Y.; Kumatani, A.; Shiku, H.; Matsue, T. Scanning Probe Microscopy for Nanoscale Electrochemical Imaging. *Anal. Chem.* **2017**, *89*, 342–357.

Tay, F. E. H.; Iliescu, C.; Jing, J.; Miao, J. Defect-Free Wet Etching through Pyrex Glass Using Cr/Au Mask. *Microsyst. Technol.* **2006**, *12*, 935–939.

Tedjo, W.; Chen, T. An Integrated Biosensor System With a High-Density Microelectrode Array for Real-Time Electrochemical Imaging. *IEEE Trans. Biomed. Circuits Syst.* **2020**, *14*, 20–35.

Tedjo, W.; Chen, T. An Integrated Biosensor System with a High-Density Microelectrode Array for Real-Time Electrochemical Imaging. *IEEE Trans. Biomed. Circuits Syst.* **2019**, 1–1.

Tedjo, W.; Nejad, J. E.; Feeny, R.; Yang, L.; Henry, C. S.; Tobet, S.; Chen, T. Electrochemical Biosensor System Using a CMOS Microelectrode Array Provides High Spatially and Temporally Resolved Images. *Biosens. Bioelectron.* **2018**, *114*, 78–88.

Termebaf, H.; Shayan, M.; Kiani, A. Two-Step Bipolar Electrochemistry: Generation of Composition Gradient and Visual Screening of Electrocatalytic Activity. *Langmuir* **2015**, *31*, 13238–13246.

Toivola, Y.; Thurn, J.; Cook, R. F.; Cibuzar, G.; Roberts, K. Influence of Deposition Conditions on Mechanical Properties of Low-Pressure Chemical Vapor Deposited Low-Stress Silicon Nitride Films. *J. Appl. Phys.* **2003**, *94*, 6915–6922.

Trantidou, T.; Tariq, M.; Terracciano, C.; Toumazou, C.; Prodromakis, T. The Effects of Annealing on Mechanical, Chemical, and Physical Properties and Structural Stability of Parylene C. *Sensors* **2014**, *14*, 11629–11639.

Tucceri, R. An Electrochemical Study of the Nickel Hydroxide-Gold Modified Electrode Employing the Surface Resistance Technique. *J. Electroanal. Chem.* **2016**, *774*, 95–101.

Uram, J. D.; Ke, K.; Mayer, M. Noise and Bandwidth of Current Recordings from Submicrometer Pores and Nanopores. *ACS Nano* **2008**, *2*, 857–872.

Viswam, V.; Bounik, R.; Shadmani, A.; Dragas, J.; Urwyler, C.; Boos, J. A.; Obien, M. E. J.; Muller, J.; Chen, Y.; Hierlemann, A. Impedance Spectroscopy and Electrophysiological Imaging of Cells With a High-Density CMOS Microelectrode Array System. *IEEE Trans. Biomed. Circuits Syst.* **2018**, *12*, 1356–1368.

Walsh, D. A.; Fernández, J. L.; Bard, A. J. Rapid Screening of Bimetallic Electrocatalysts for Oxygen Reduction in Acidic Media by Scanning Electrochemical Microscopy. *J. Electrochem. Soc.* **2006**, *153*, E99.

Wang, C.; Jia, G.; Taherabadi, L. H.; Madou, M. J. A Novel Method for the Fabrication of High-Aspect Ratio C-MEMS Structures. *J. Microelectromech. Sys.* **2005**, *14*, 348–358.

Wang, C.; Markovic, N. M.; Stamenkovic, V. R. Advanced Platinum Alloy Electrocatalysts for the Oxygen Reduction Reaction. *ACS Catal.* **2012**, *2*, 891–898.

Wang, G.; Parrondo, J.; He, C.; Li, Y.; Ramani, V. Pt/C/Ni(OH)2 Bi-Functional Electrocatalyst for Enhanced Hydrogen Evolution Reaction Activity under Alkaline Conditions. *J. Electrochem. Soc.* **2017**, *164*, F1307.

Wang, L.; Lin, C.; Huang, D.; Chen, J.; Jiang, L.; Wang, M.; Chi, L.; Shi, L.; Jin, J. Optimizing the Volmer Step by Single-Layer Nickel Hydroxide Nanosheets in Hydrogen Evolution Reaction of Platinum. *ACS Catal.* **2015**, *5*, 3801–3806.

Wang, Y.-J.; Zhao, N.; Fang, B.; Li, H.; Bi, X. T.; Wang, H. Carbon-Supported Pt-Based Alloy Electrocatalysts for the Oxygen Reduction Reaction in Polymer Electrolyte Membrane Fuel Cells: Particle Size, Shape, and Composition Manipulation and Their Impact to Activity. *Chem. Rev.* **2015**, *115*, 3433–3467.

Wanunu, M.; Dadosh, T.; Ray, V.; Jin, J.; McReynolds, L.; Drndić, M. Rapid Electronic Detection of Probe-Specific MicroRNAs Using Thin Nanopore Sensors. *Nat. Nanotechnol.* **2010**, *5*, 807–814.

Woodhouse, M.; Parkinson, B. A. Combinatorial Discovery and Optimization of a Complex Oxide with Water Photoelectrolysis Activity. *Chem. Mater.* **2008**, *20*, 2495–2502.

Wu, H.; Zhu, T.; Lu, X.; Wei Ho, G. High-Efficient Electrocatalysts by Unconventional Acid-Etching for Overall Water Splitting. *J. Mater. Chem. A* **2017**, *5*, 24153–24158.

Wu, M.-S.; Liu, Z.; Shi, H.-W.; Chen, H.-Y.; Xu, J.-J. Visual Electrochemiluminescence Detection of Cancer Biomarkers on a Closed Bipolar Electrode Array Chip. *Anal. Chem.* **2015**, *87*, 530–537.

Wu, M.-Y.; Krapf, D.; Zandbergen, M.; Zandbergen, H.; Batson, P. E. Formation of Nanopores in a SiN⁄SiO2 Membrane with an Electron Beam. *Appl. Phys. Lett.* **2005**, *87*, 113106.

Wydallis, J. B.; Feeny, R. M.; Wilson, W.; Kern, T.; Chen, T.; Tobet, S.; Reynolds, M. M.; Henry, C. S. Spatiotemporal Norepinephrine Mapping Using a High-Density CMOS Microelectrode Array. *Lab. Chip* **2015**, *15*, 4075–4082.

Xia, P.; Zuo, J.; Paudel, P.; Choi, S.; Chen, X.; Rahman Laskar, M. A.; Bai, J.; Song, W.; Im, J.; Wang, C. Sapphire-Supported Nanopores for Low-Noise DNA Sensing. *Biosens. Bioelectron.* **2021**, *174*, 112829.

Xiang, C.; Suram, S. K.; Haber, J. A.; Guevarra, D. W.; Soedarmadji, E.; Jin, J.; Gregoire, J. M. High-Throughput Bubble Screening Method for Combinatorial Discovery of Electrocatalysts for Water Splitting. *ACS Comb. Sci.* **2014**, *16*, 47–52.

Xie, L.; Ren, X.; Liu, Q.; Cui, G.; Ge, R.; M. Asiri, A.; Sun, X.; Zhang, Q.; Chen, L. A $Ni(OH)_2$ – PtO_2 Hybrid Nanosheet Array with Ultralow Pt Loading toward Efficient and Durable Alkaline Hydrogen Evolution. *J. Mater. Chem. A* **2018**, *6*, 1967–1970.

Xu, W.; Zou, G.; Hou, H.; Ji, X. Single Particle Electrochemistry of Collision. *Small* **2019**, *15*, 1804908.

Xue, L.; Yamazaki, H.; Ren, R.; Wanunu, M.; Ivanov, A. P.; Edel, J. B. Solid-State Nanopore Sensors. *Nat. Rev. Mater.* **2020**, *5*, 931–951.

Yanagi, I.; Akahori, R.; Hatano, T.; Takeda, K. Fabricating Nanopores with Diameters of Sub-1 Nm to 3 Nm Using Multilevel Pulse-Voltage Injection. *Sci. Rep.* **2015**, *4*, 5000.

Yang, M.; Batchelor-McAuley, C.; Kätelhön, E.; Compton, R. G. Reaction Layer Imaging Using Fluorescence Electrochemical Microscopy. *Anal. Chem.* **2017**, *89*, 6870–6877.

Yang, W.; Chen, S. Recent Progress in Electrode Fabrication for Electrocatalytic Hydrogen Evolution Reaction: A Mini Review. *Chem. Eng. J.* **2020**, *393*, 124726.

Yang, Y.; Chen, G.; Zeng, R.; Villarino, A. M.; DiSalvo, F. J.; van Dover, R. B.; Abruña, H. D. Combinatorial Studies of Palladium-Based Oxygen Reduction Electrocatalysts for Alkaline Fuel Cells. *J. Am. Chem. Soc.* **2020**, *142*, 3980–3988.

Yu, X.; Zhao, J.; Zheng, L.-R.; Tong, Y.; Zhang, M.; Xu, G.; Li, C.; Ma, J.; Shi, G. Hydrogen Evolution Reaction in Alkaline Media: Alpha- or Beta-Nickel Hydroxide on the Surface of Platinum? *ACS Energy Lett.* **2018**, *3*, 237–244.

Zhai, Q.; Zhang, X.; Han, Y.; Zhai, J.; Li, J.; Wang, E. A Nanoscale Multichannel Closed Bipolar Electrode Array for Electrochemiluminescence Sensing Platform. *Anal. Chem.* **2016**, *88*, 945–951.

Zhan, W.; Alvarez, J.; Crooks, R. M. Electrochemical Sensing in Microfluidic Systems Using Electrogenerated Chemiluminescence as a Photonic Reporter of Redox Reactions. *J. Am. Chem. Soc.* **2002**, *124*, 13265–13270.

Zhang, B.; Heien, M. L. A. V.; Santillo, M. F.; Mellander, L.; Ewing, A. G. Temporal Resolution in Electrochemical Imaging on Single PC12 Cells Using Amperometry and Voltammetry at Microelectrode Arrays. *Anal. Chem.* **2011**, *83*, 571–577.

Zhang, J.; Zhou, J.; Tian, C.; Yang, S.; Jiang, D.; Zhang, X.-X.; Chen, H.-Y. Localized Electrochemiluminescence from Nanoneedle Electrodes for Very-High-Density Electrochemical Sensing. *Anal. Chem.* **2017**, *89*, 11399–11404.

Zhang, J.-D.; Hao, N.; Lu, L.; Yun, S.; Zhu, X.-F.; Hong, K.; Feng, L.-D. High-Efficient Preparation and Screening of Electrocatalysts Using a Closed Bipolar Electrode Array System. *J. Electroanal. Chem.* **2019**, *832*, 1–6.

Zhang, X.; van Deursen, P. M. G.; Fu, W.; Schneider, G. F. Facile and Ultraclean Graphene-on-Glass Nanopores by Controlled Electrochemical Etching. *ACS Sens.* **2020**, *5*, 2317–2325.

Zhang, Y.; McGinn, P. J. Combinatorial Screening for Methanol Oxidation Catalysts in Alloys of Pt, Cr, Co and V. *J. Power Sources* **2012**, *206*, 29–36.

Zhu, C.; Huang, K.; Siepser, N. P.; Baker, L. A. Scanning Ion Conductance Microscopy. *Chem. Rev.* **2020**, acs.chemrev.0c00962.

Zhu, M.-J.; Pan, J.-B.; Wu, Z.-Q.; Gao, X.-Y.; Zhao, W.; Xia, X.-H.; Xu, J.-J.; Chen, H.-Y. Electrogenerated Chemiluminescence Imaging of Electrocatalysis at a Single Au-Pt Janus Nanoparticle. *Angew. Chem. Int. Ed.* **2018**, *57*, 4010–4014.

Zhu, Y.; Lin, Q.; Zhong, Y.; Tahini, H. A.; Shao, Z.; Wang, H. Metal Oxide-Based Materials as an Emerging Family of Hydrogen Evolution Electrocatalysts. *Energy Environ. Sci.* **2020**, *13*, 3361–3392.

Zou, N.; Chen, G.; Mao, X.; Shen, H.; Choudhary, E.; Zhou, X.; Chen, P. Imaging Catalytic Hotspots on Single Plasmonic Nanostructures via Correlated Super-Resolution and Electron Microscopy. *ACS Nano* **2018**, *12*, 5570–5579.

Zwickl, B. M.; Shanks, W. E.; Jayich, A. M.; Yang, C.; Bleszynski Jayich, A. C.; Thompson, J. D.; Harris, J. G. E. High Quality Mechanical and Optical Properties of Commercial Silicon Nitride Membranes. *Appl. Phys. Lett.* **2008**, *92*, 103125.

APPENDIX A

Supplementary material for Chapter 2: Submicron Bipolar Electrode Arrays via Laser Interference Lithography.

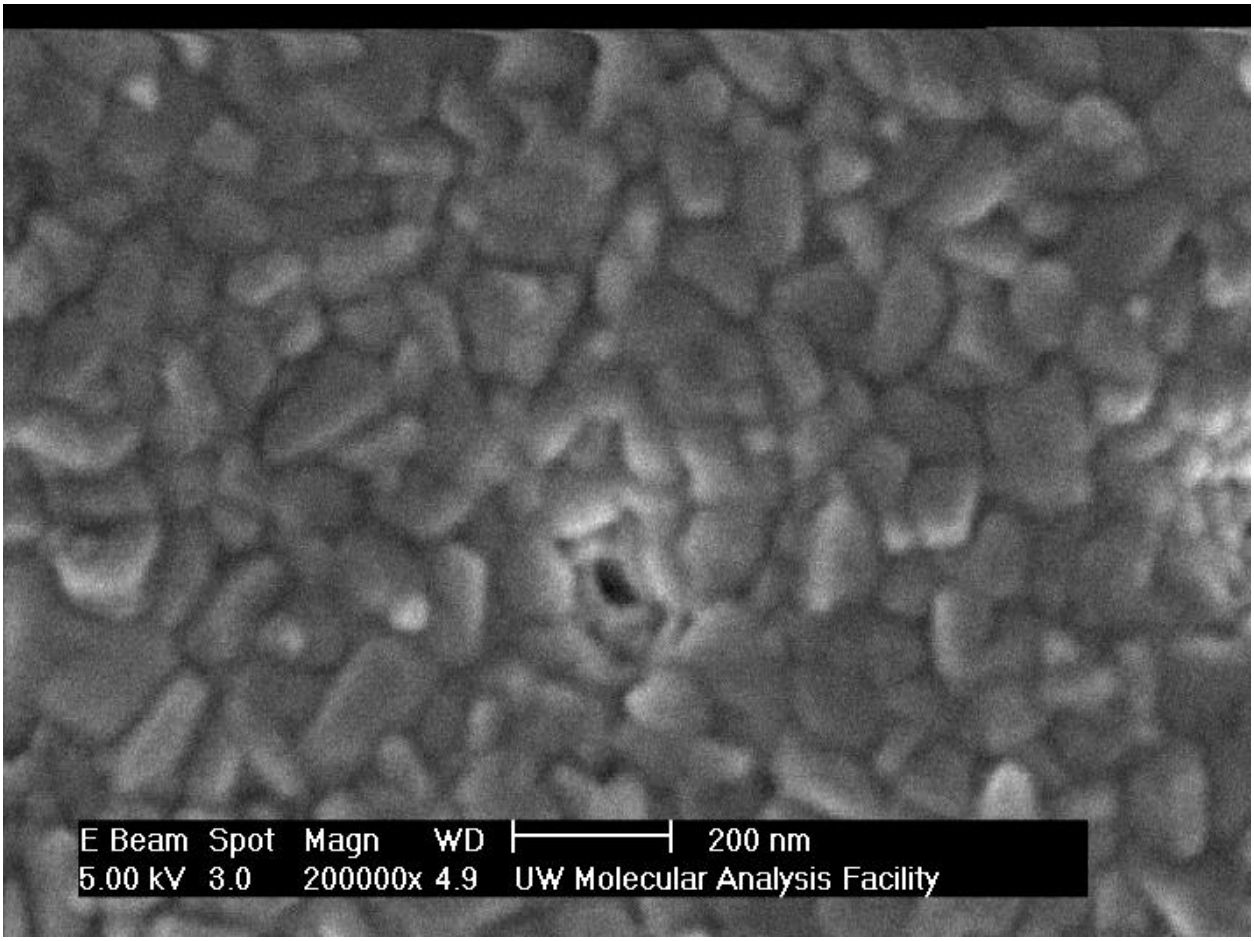

Figure A1. SEM micrograph of a ~500 nm SiN_x pore after evaporation of Au (50 nm) and Ti (650 nm) over the surface at 5 Å/s.

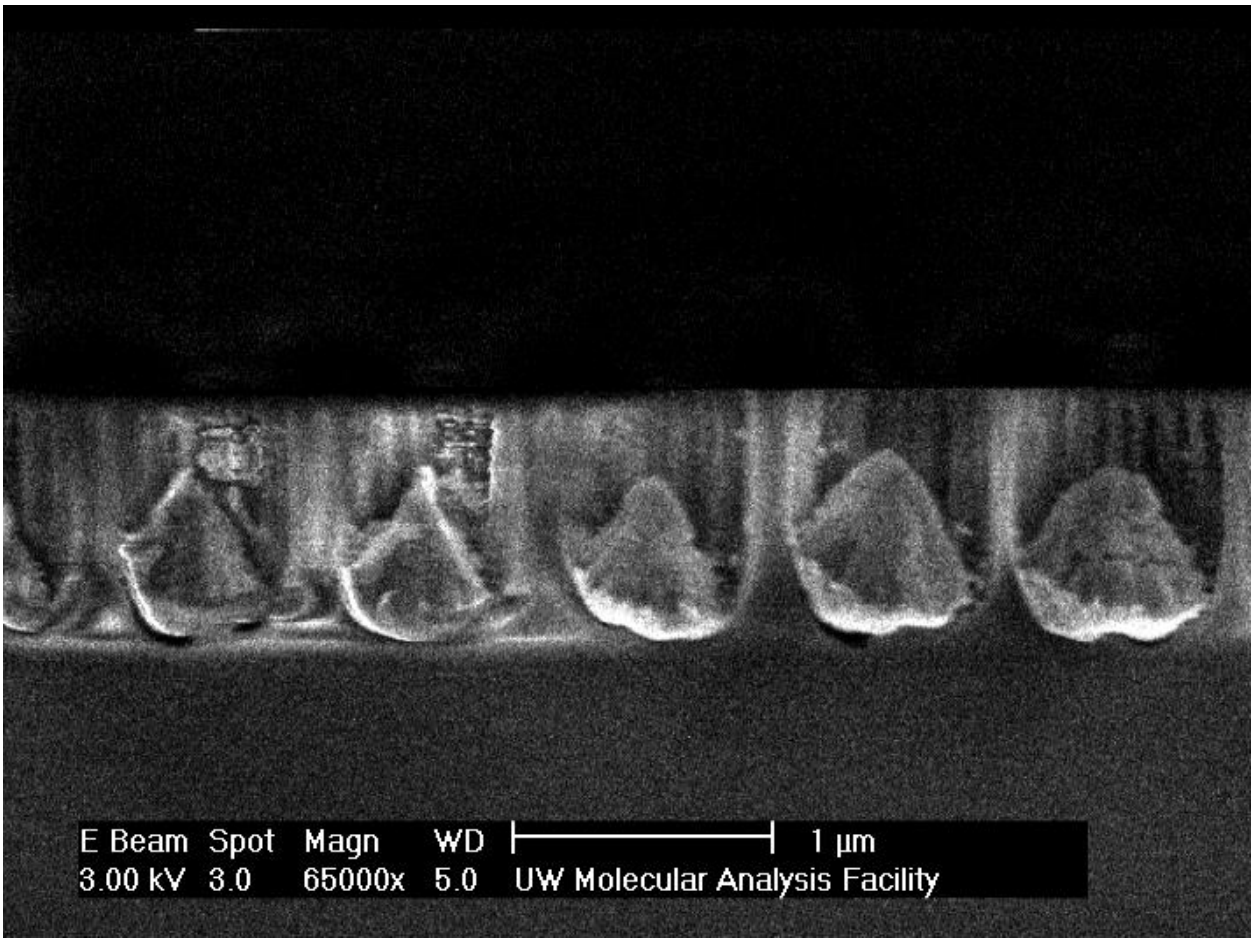

Figure A2. Cross-sectional SEM micrograph of array from **Figure A1** after lift-off of overlying metal film (chip was cleaved prior to imaging). Note that Si-supported region was imaged since freestanding membrane did not survive cleaving.

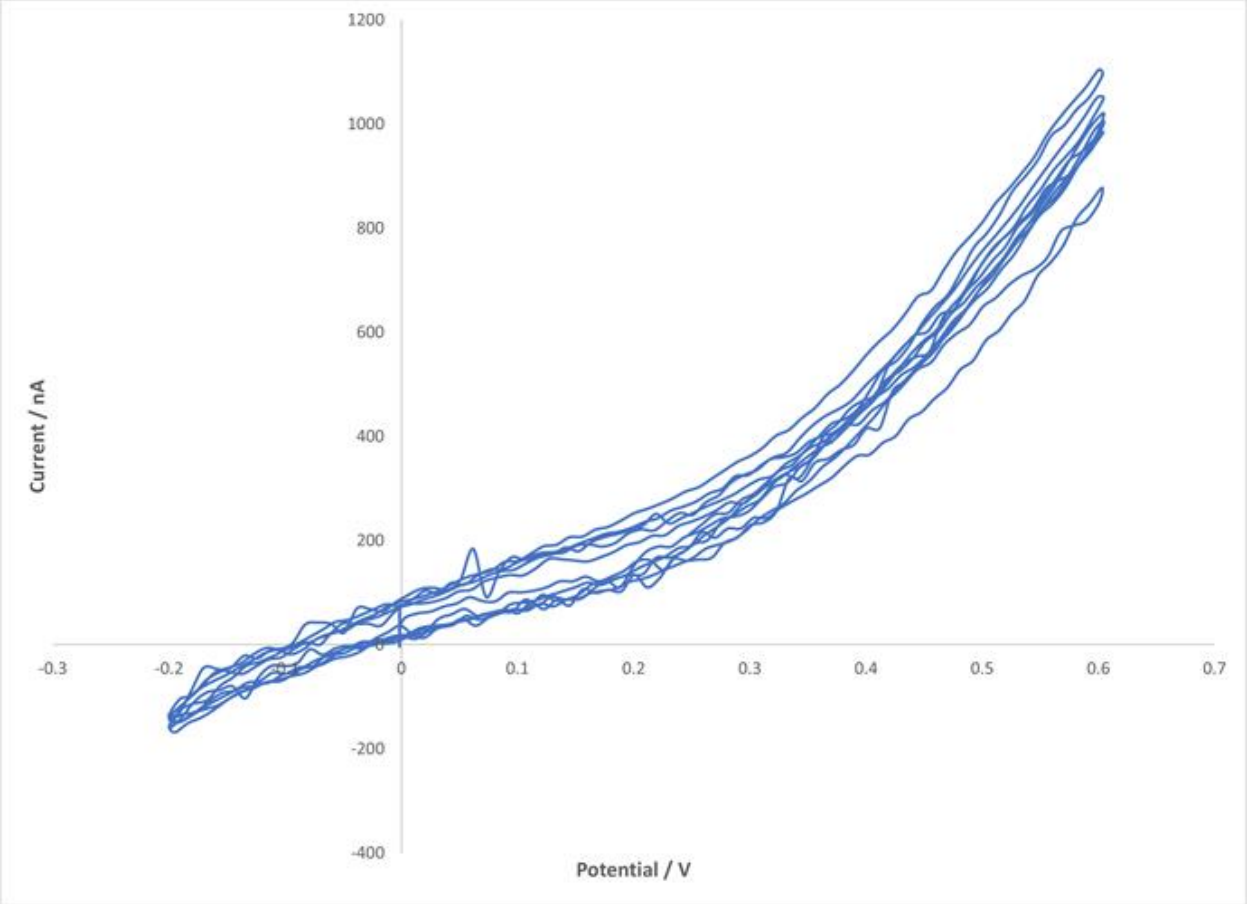

Figure A3. CV of 1 mM ferrocenemethanol 100 mM KCl coupled to 1 mM $Fe(CN)_6^{3-}$ 100 mM across a BPE array using a driving potential waveform of -0.2 to 0.6 V vs. Ag/AgCl at 100 mV/s (6 cycles).

APPENDIX B

Supplementary material for Chapter 3:Electrochemiluminescence (ECL)-Based Electrochemical Imaging Using a Massive Array of Bipolar Ultramicroelectrodes.

Chemicals and Materials. The following chemicals were used as received from their manufacturers: nitric acid (HNO_3, Sigma-Aldrich, 70%), perchloric acid ($HClO_4$, Sigma-Aldrich, 70%), hydrochloric acid (HCl, Sigma-Aldrich, 37%), sodium perchlorate monohydrate ($NaClO_4 \cdot H_2O$, Fluka, >99%), potassium chloride (KCl, Fluka, >99%), potassium hydroxide (KOH, Sigma-Aldrich, 99.99%), platinum(IV) chloride ($PtCl_4$, Sigma-Aldrich, >99.9%), nickel(II) chloride ($NiCl_2$, Sigma-Aldrich, 98%), sodium chloride (NaCl, Sigma-Aldrich, >99%), gold(III) chloride ($AuCl_3$, Salt Lake Metals, 1.534% solution), Gold Etch TFA (Transene), tris(2,2'-bipyridyl)dichlororuthenium(II) hexahydrate ($Ru(bpy)_3Cl_2 \cdot 6H_2O$, Sigma-Aldrich, 99.5%), 2-(dibutylamino)ethanol (DBAE, Sigma-Aldrich, 99%), potassium phosphate monobasic (KH_2PO_4, J.T. Baker, 99.9%), potassium phosphate dibasic (K_2HPO_4, J.T. Baker, 99.9%). All solutions were prepared with 18.2 MΩ·cm deionized water from a Barnstead NANOpure water purification system (Thermo Scientific).

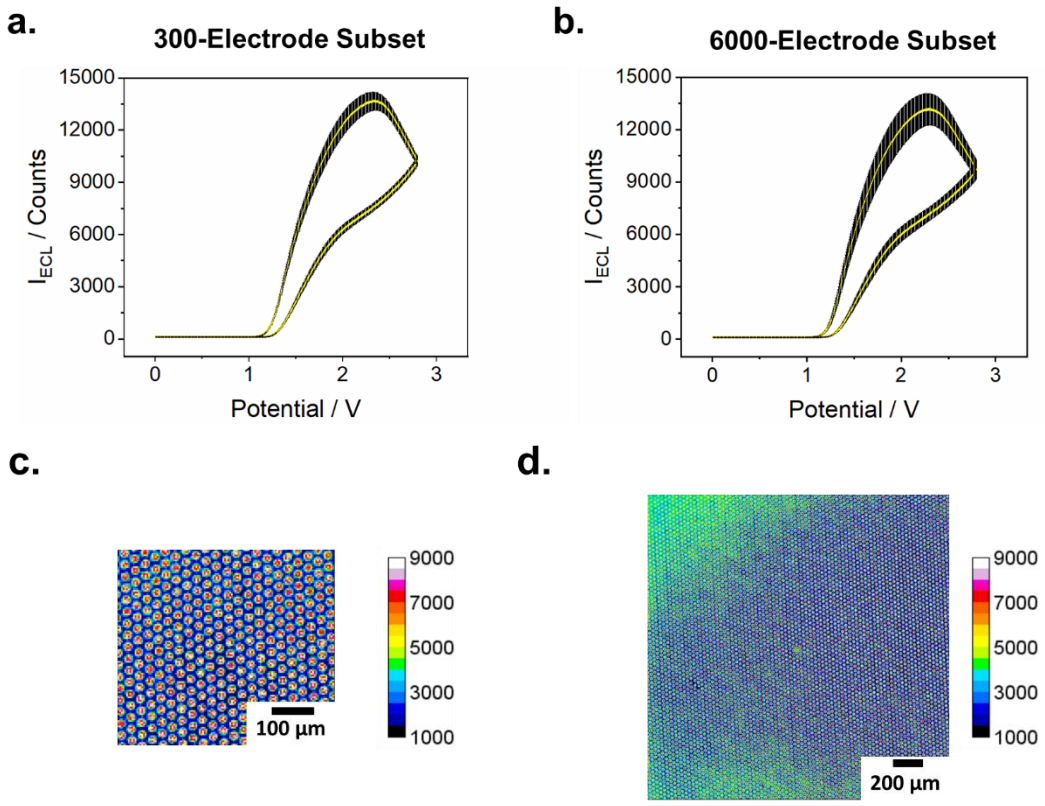

Figure B1. Plot of average I_{ECL} (yellow points) ± standard deviation (black error bars) of each individual electrode's intensity a (a) 300-electrode and (b) 6000-electrode array subset. Panel (a) uses the same ~300 electrode subset as was used in **Figure 3.3c**, while panel (b) uses all ~6000 electrodes within the field of view. Plots of ECL intensity across the array at 2.8 V for (c) the 300-electrode subset and (d) the 6000-electrode subset.

APPENDIX C

Supplementary material for Chapter 4:High-Throughput Electrocatalyst Screening on a Massive Array of Bipolar Ultramicroelectrodes.

Chemicals and Materials. The following chemicals were used as received from their manufacturers: nitric acid (HNO_3, Sigma-Aldrich, 70%), perchloric acid ($HClO_4$, Sigma-Aldrich, 70%), hydrochloric acid (HCl, Sigma-Aldrich, 37%), sodium perchlorate monohydrate ($NaClO_4 \cdot H_2O$, Fluka, >99%), potassium chloride (KCl, Fluka, >99%), potassium hydroxide (KOH, Sigma-Aldrich, 99.99%), platinum(IV) chloride ($PtCl_4$, Sigma-Aldrich, >99.9%), nickel(II) chloride ($NiCl_2$, Sigma-Aldrich, 98%), sodium chloride (NaCl, Sigma-Aldrich, >99%), gold(III) chloride ($AuCl_3$, Salt Lake Metals, 1.534% solution), Gold Etch TFA (Transene), tris(2,2'-bipyridyl)dichlororuthenium(II) hexahydrate ($Ru(bpy)_3Cl_2 \cdot 6H_2O$, Sigma-Aldrich, 99.5%), 2-(dibutylamino)ethanol (DBAE, Sigma-Aldrich, 99%), potassium phosphate monobasic (KH_2PO_4, J.T. Baker, 99.9%), potassium phosphate dibasic (K_2HPO_4, J.T. Baker, 99.9%). All solutions were prepared with 18.2 MΩ·cm deionized water from a Barnstead NANOpure water purification system (Thermo Scientific).

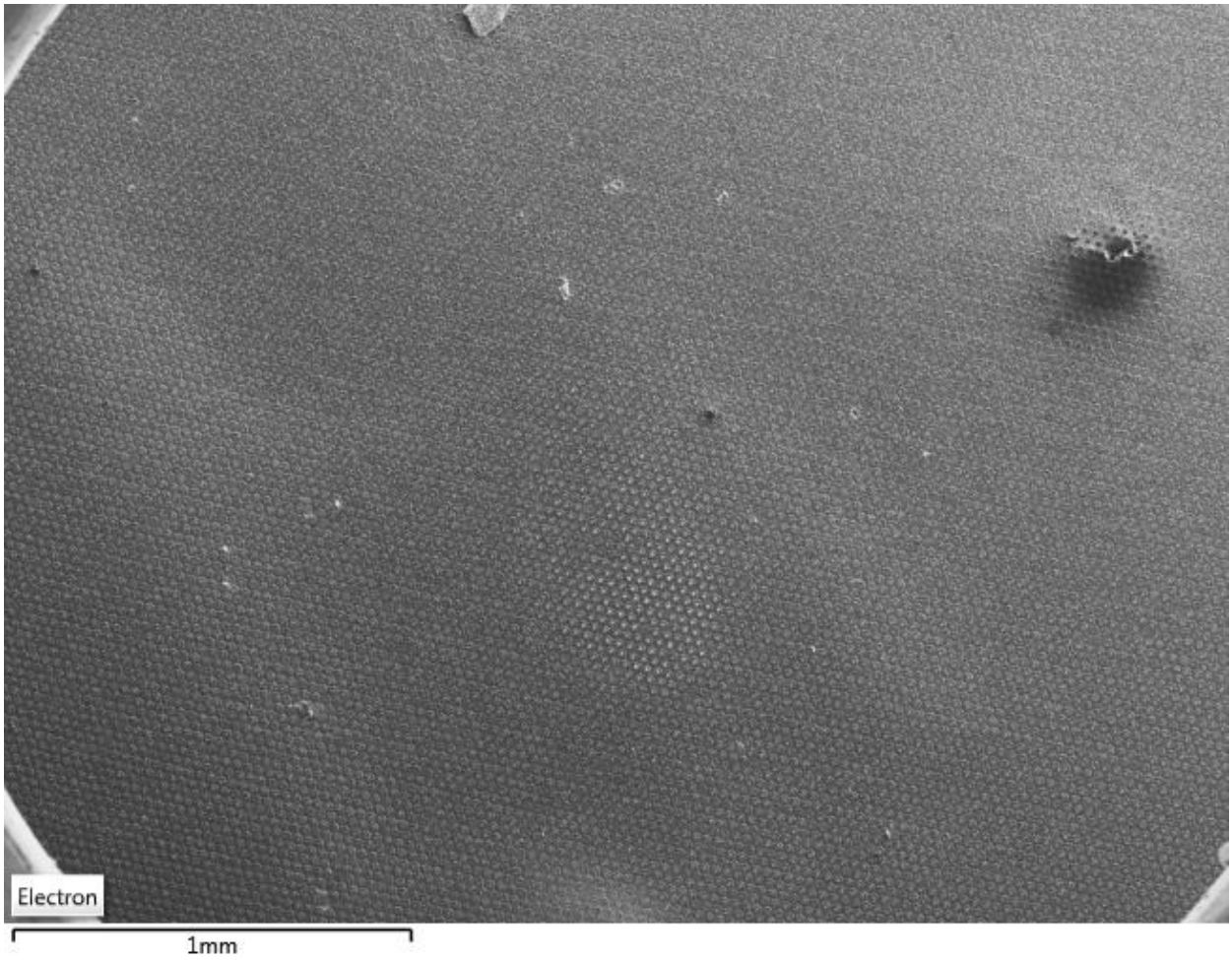

Figure C1. SEM image of gradient Pt deposition shown in **Figure 4.2**.

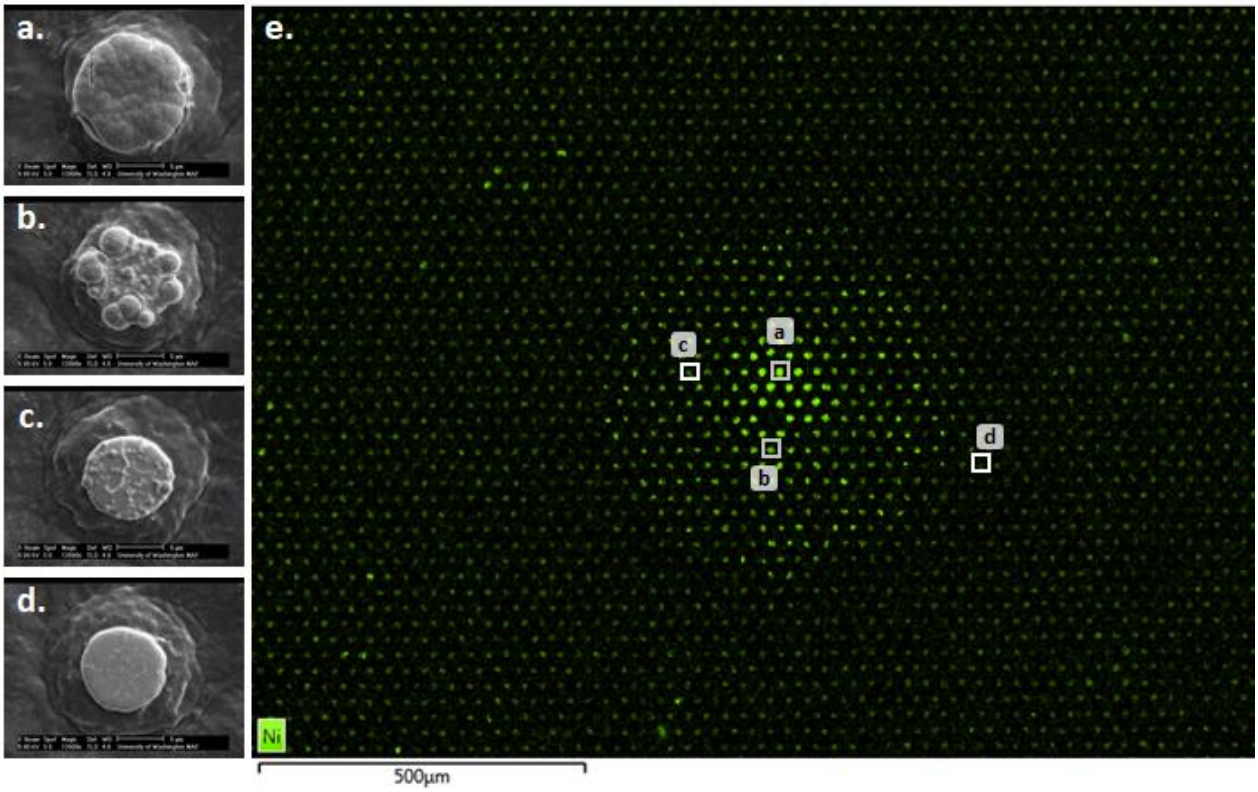

Figure C2. (a-d) SEM images of selected electrodes from a $Ni(OH)_2$ gradient deposition site. (e) EDS map of Ni across gradient deposition site with SEM-imaged electrodes labeled.

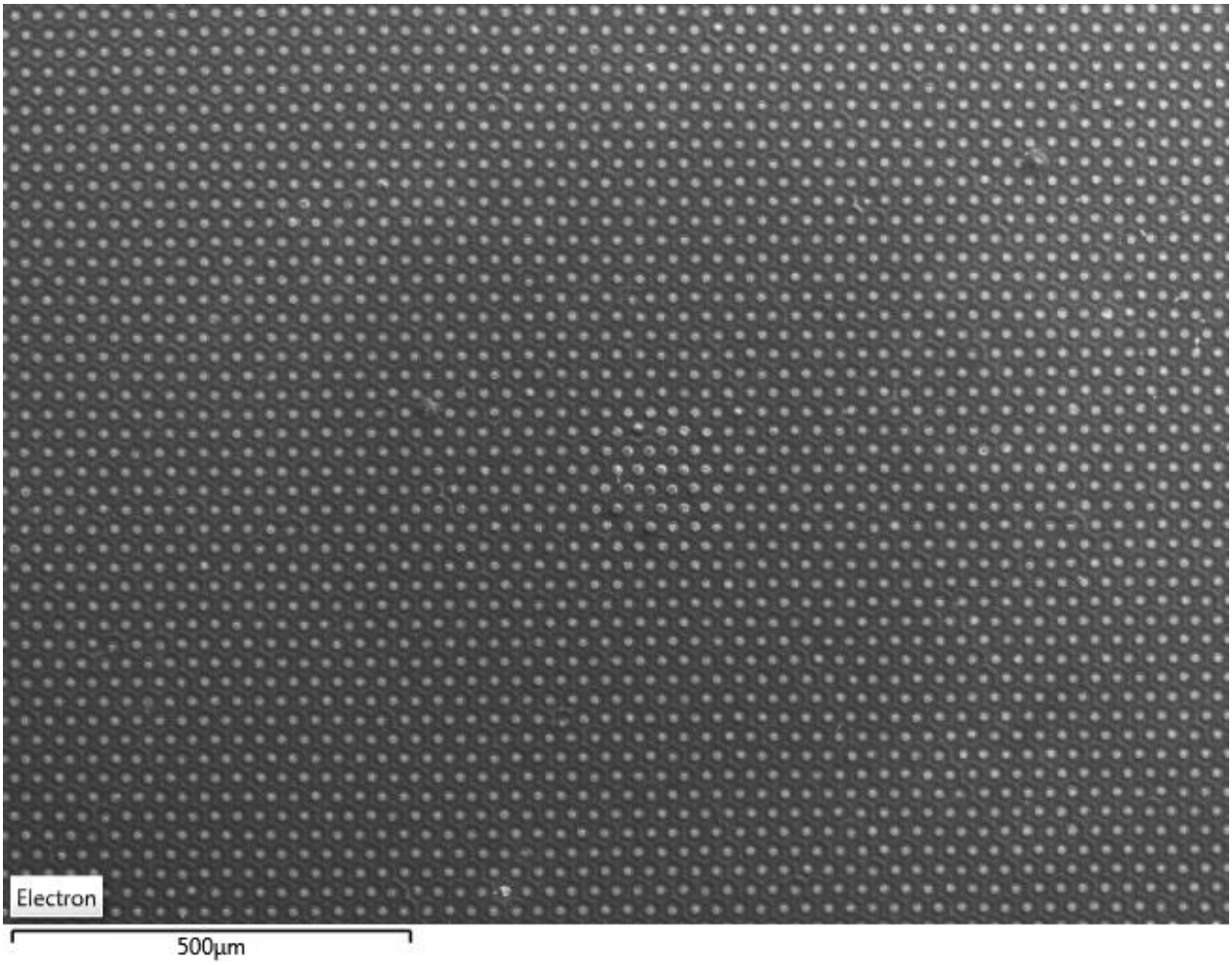

Figure C3. SEM image of the $Ni(OH)_2$ gradient deposition shown in **Figure C2**.

APPENDIX D

Supplementary material for Chapter 5: Novel Microfabricated Glass Freestanding Membrane Chips for Low-Noise Nanopore Substrates.

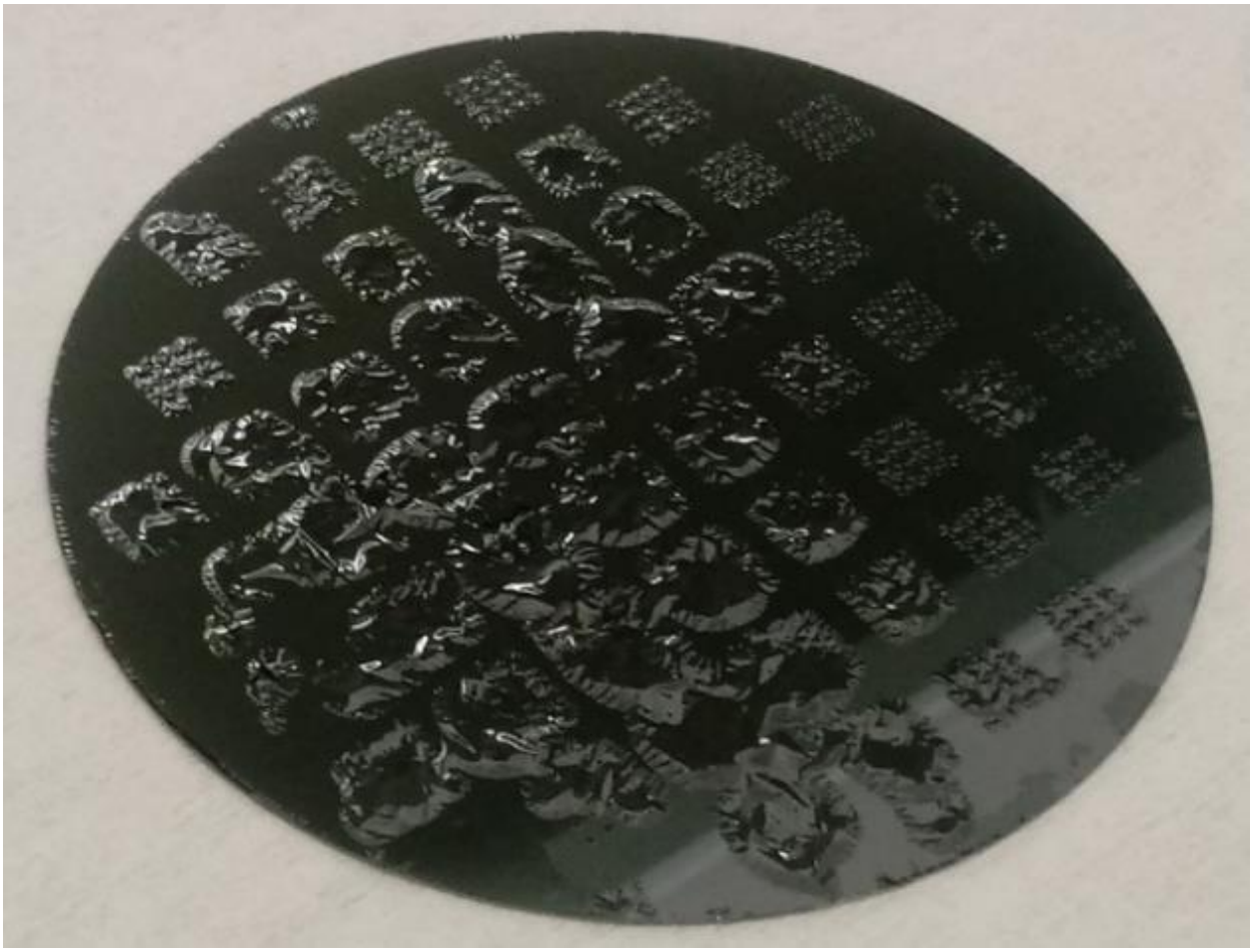

Figure D1. Photograph of partially delaminated 2 μm thick a-Si mask after HF etching.

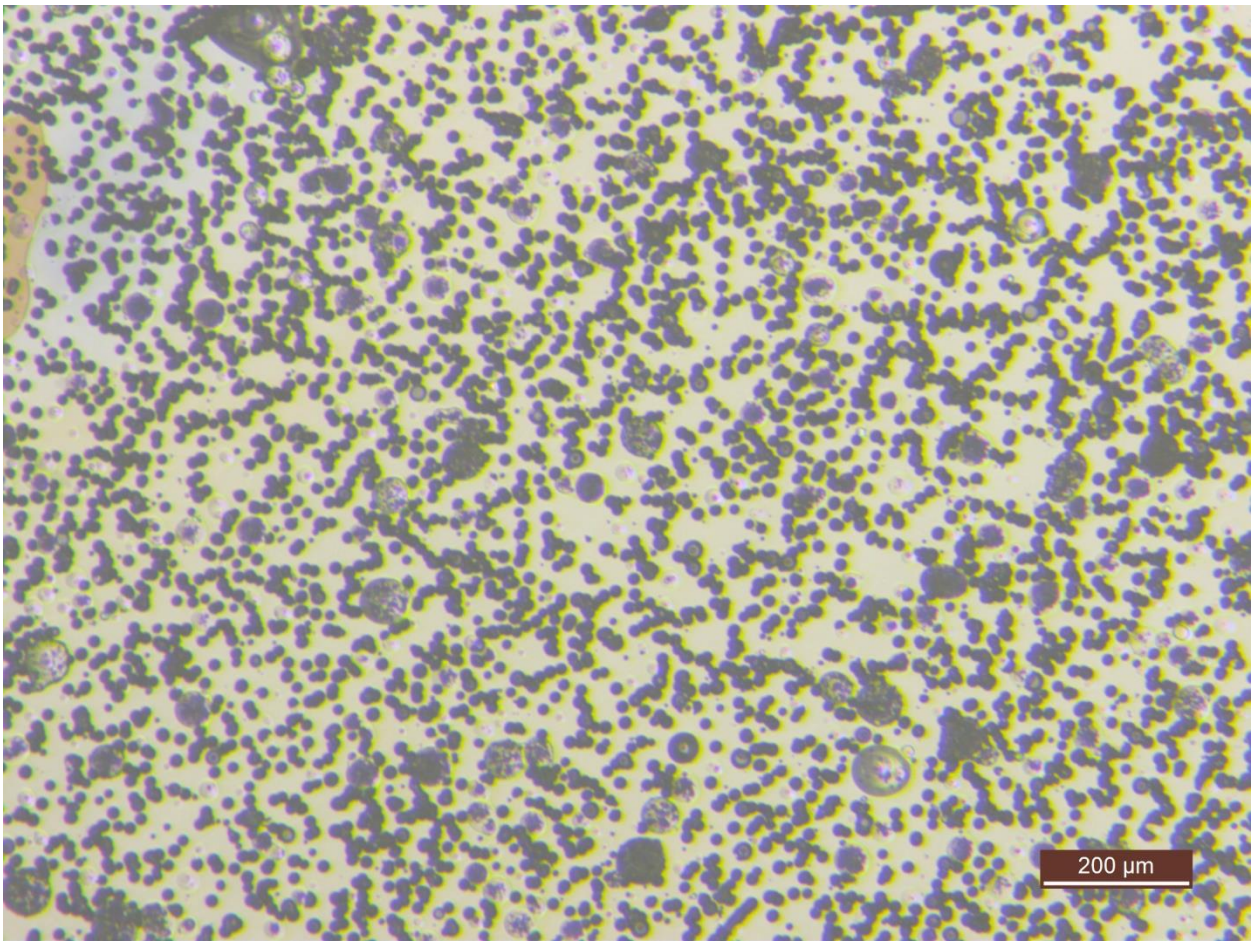

Figure D2. Optical microscope image of pitted glass surface after removal of Si backing via dissolution in 35% KOH solution at 100°C.

VITA

Todd Anderson grew up in Port Orchard, Washington, a small town on the Kitsap Peninsula directly across the Puget Sound from Seattle. He was homeschooled all the way through high school before enrolling in Olympic College, a community college in nearby Bremerton. After obtaining his Associate's Degree in 2012, he transferred to the University of Washington where he graduated with a B.S. in Chemistry in 2014. He returned to the University of Washington in 2015 as a graduate student where he worked in Professor Bo Zhang's lab to study electroanalytical chemistry while earning a Ph.D. in Chemistry.